THE STRUCTURE OF SATURN'S RINGS AND THE SURFACES OF THE GALILEAN SATELLITES AS INFERRED FROM RADAR OBSERVATIONS

by

STEVEN JEFFREY OSTRO

B.S. and A.B., Rutgers, The State University
(1969)

M.Eng'g., Cornell University
(1974)

SUBMITTED IN PARTIAL FULFILLMENT
OF THE REQUIREMENTS FOR THE
DEGREE OF

DOCTOR OF PHILOSOPHY

AT THE

MASSACHUSETTS INSTITUTE OF TECHNOLOGY

AUGUST 1978

Signature of Author..
Department of Earth and Planetary Sciences
August 1978

Certified by..
Thesis Supervisor

Accepted by...
Chairman, Department Committee

THE STRUCTURE OF SATURN'S RINGS AND THE SURFACES OF THE GALILEAN SATELLITES AS INFERRED FROM RADAR OBSERVATIONS

by

STEVEN JEFFREY OSTRO

Submitted to the Department of Earth and Planetary Sciences
on August 31, 1978, in partial fulfillment of the
requirements for the Degree of Doctor of Philosophy.

ABSTRACT

Radar observations undertaken from 1976 to 1978, using the 12.6-cm radar system of the Arecibo Observatory, are used to place constraints on the structure of Saturn's rings and the surfaces of the outer three (icy) Galilean satellites.

Measurements of the ratio, μ_C, of the echo power received in the same circular sense as transmitted to that received in the orthogonal sense, yield 1.58±0.16, 1.50±0.19, and 1.18±0.12 for Europa, Ganymede, and Callisto, respectively. (All astronomical targets previously studied by radar have $\mu_C \ll 1$.) A model which can explain this unusual polarization behavior postulates a thick surface layer of ice saturated with nearly hemispherical craters. In developing this model, I note that a single coherent reflection at normal incidence reverses the rotational sense of circularly polarized incident radiation ($\mu_C = 0$), while multiple dielectric reflections tend to produce an unpolarized echo ($\mu_C \rightarrow 1$). However, two coupled reflections can produce the observed backscattering behavior, provided the angles of incidence lie between the Brewster angle and its complement. The effect is maximum when the angles equal 45°, yielding a ratio $\mu_C = 1.9$ for water ice. Randomly oriented reflecting facets, either of ice on the surface or of rocks in the interior, cannot yield the observed behavior because too few of the total possible backscattering configurations meet the above requirement. Hemispherical craters, on the other hand, favor 45°-double-reflection backscatter. I have used modified geometrical optics and the Stokes-vector formalism to model the scattering from nearly hemispherical craters whose interiors consist of plane facets many wavelengths in size. If the surface material has a refractive index 15% larger than that of pure water ice, this model can explain the observed radar results with regard to circular and linear polarization properties, geometric albedo, and angular scattering law.

Mean geometric albedos, α, of 0.64±0.16, 0.35±0.09, and 0.14±0.04 have been determined for Europa, Ganymede, and Callisto, respectively. The orbital-phase dependence of the radar albedos appears similar to that observed at visible wavelengths for all three satellites.

The radial distribution of radar scatterers in Saturn's rings has been estimated from delay-Doppler observations made in January 1976. The optically defined A and B rings are apparently responsible for most of the radar echo. The outer half of the B ring (next to the Cassini Division) is an especially reflective region. There is no significant evidence for radar backscattering from particles interior to the B ring, exterior to the A ring, or from the planet itself. Unexpectedly large amounts of power at Doppler shifts near the center of the echo spectrum, previously reported for a ring opening angle $|B| = 24.4°$, are not apparent in spectra obtained in 1976-1978 for $|B| \leq 21.4°$.

The 12.6-cm geometric albedo and polarization ratio of Saturn's rings have been determined as: $\alpha = 0.24 \pm 0.06$ and $\mu_C = 0.57 \pm 0.12$ at $|B| = 18.2°$ in April 1977; and $\alpha = 0.27 \pm 0.07$ and $\mu_C = 0.40 \pm 0.05$ at $|B| = 11.7°$ in February 1978. These values for α and μ are significantly lower than corresponding values measured at 3.5-cm wavelength and $|B| = 24.4°$ (Goldstein et al., 1977). It follows that the radar backscattering properties of Saturn's rings are dependent on wavelength or opening angle, or both.

The circular polarization ratios reported for Saturn's rings are much less than unity, suggesting the importance of single-particle backscattering in the 12.6-cm radar echo. These results can be interpreted in terms of either a monolayer of large (radius >> wavelength) irregular particles or a many-particle-thick layer of particles with very low single-scattering polarization ratios.

Thesis Supervisor: Gordon H. Pettengill

Title: Professor of Planetary Physics

ACKNOWLEDGEMENTS

I am indebted to many people for their assistance, encouragement, and inspiration during the preparation of this thesis.

I would like to express my extreme gratitude to Gordon H. Pettengill, my research advisor, for his patient guidance and interest in my work since 1974, and for the careful attention he has given to this thesis. Gordon's superior stature, both as an articulate scientist and as a warm, generous, and compassionate human being, has provided me with an outstanding professional and personal example during my years at MIT.

I would like to thank Donald B. Campbell for his superb instruction in the art of making radar observations at Arecibo. His extraordinary patience, sensible advice, and constant encouragement during my visits to the observatory have been of immeasurable importance to me. I am especially grateful to Don for the hospitality he has extended to me and my family.

I would like to thank Irwin I. Shapiro for his many positive criticisms of my work, and for innumerable critical lessons on the methods of good scientific research. I am especially grateful to Irwin for his understanding of the problems associated with changing one's academic field. His words of encouragement and expressions of confidence in my abilities will never be forgotten.

I would like to thank John S. Lewis, the chairman of my Thesis Committee, and David H. Staelin for their careful reading of the manuscript, many useful suggestions, and interesting discussions of the implications of the icy-crater theory.

I would like to express my gratitude to Chuck Counselman for reading my thesis and serving on my Examination Committee on very short notice.

I would like to thank Robert D. Reasenberg for valuable discussions of parameter estimation techniques.

I would like to express my extreme gratitude to my parents, Ira and Mary Ostro, for their unwavering support throughout my graduate education, for impressing upon me the importance of excellence in scholarship, and for nurturing my childhood fascination with science. In many respects, this thesis is a tribute to my parents' faith in me.

I would like to thank my parents-in-law, Thomas and Marie Musca, for their constant encouragement and unlimited positive energy, but most of all for their eldest daughter.

I am grateful to Harold D. Craft, Jr., for his cooperation in scheduling the radar observations discussed in this thesis and for ensuring that my family's visits to the observatory were comfortable. I would also like to express my appreciation to Tom Dickinson, Reinaldo Velez, and Mike Davis for their assistance in various phases of my work at Arecibo.

I would like to thank Sheila Parker for typing the appendices, and Julie Roberts for loaning me her desk and typewriter.

I would like to thank Jon Mills for his consistently excellent classes in Uechi-Ryu Karate, and the following individuals for sharing their idealism and their enthusiasm for hard work: Bruce Blair, (my Uncle) Michael S. Kline, Francis Greene, Lawrence Payne, Harold T. Smythe, Jack Spector, Joseph Veverka, and Yervant Terzian.

I have saved my warmest and deepest thanks for my precious wife, Jeanne. Her companionship, emotional support, and unlimited devotion have been a constant source of strength during my graduate school years. I dedicate this thesis to Jeanne, with all my love.

Financial support for this research was provided under NASA Grant NGR 22-009-672.

TABLE OF CONTENTS

LIST OF TABLES

LIST OF ILLUSTRATIONS

I. INTRODUCTION

I. A. Motivations for the research and its scientific context

This is a dissertation on ground-based radar investigation of the physical structure of Saturn's rings and the surfaces of the Galilean satellites. The balance between observational and theoretical emphases of the research is fairly even, although the major theoretical effort concerns the surfaces of Europa, Ganymede, and Callisto. The research has been carried out during the years 1975-1978, a period which not only marks the beginning of major exploration of the outer solar system with spacecraft, but also is a particularly interesting time in the history of ground-based radar astronomy.

The early astronomical applications of radar technology led to discovery of Mercury and Venus rotation periods, improved the knowledge of planetary orbits and the astronomical unit, and contributed to determination of such properties of the inner planets as masses, radii, topography and gravitational figure. (I shall use the term "inner planets" to include the Moon.) Used extensively to examine planetary surfaces, radar astronomical techniques will be paramount in exploration of the surface of Venus.

The scientific context of this thesis is preliminary reconnaissance of outer solar system bodies. Much of the scientific challenge inherent in radar investigation of Saturn's rings and the Galilean satellite surfaces lies in the combination of three facts. First, our a priori knowledge of large-scale surface structure is practically nil. Second, the composition, physical environment, and cosmogony of these targets suggest that their structure may have very little in common with that of the inner planets. Third, many of the radar properties of bodies in the outer solar system are fundamentally different from those of the inner planets. In fact, traditional scattering theories which interpret these properties in terms of surface structure are often inapplicable.

In other words, we have only a poor idea of what the Galilean satellites and Saturn's rings actually would look like at close range. We have strong reason to believe that they are vastly different from anything we've seen before; thus, previous experience in relating radar observations to "ground truth" are not very helpful.

The major goal of this thesis is to infer structural properties of the Galilean satellite surfaces and Saturn's rings from radar observations. The rings and the outer three Galilean satellites are the only easily detectable radar targets in the outer solar system using radar systems currently available. Their unusually large radar brightness is apparently related to the presence of surface water ice. Thus, this dissertation undertakes, as its major topic, a radar study of the large, water-ice bodies in the solar system. Indeed, major constraints on the structure of both the rings and the surfaces of the satellites follow from two basic radar properties: the surface albedo and echo polarization. To a large degree, the techniques of observation and subsequent data analysis were similar for the Galilean satellites and Saturn's rings.

However, the inference of structural properties from radar observations obviously presents different problems for these two disparate types of targets. While one is interested in constraints on surface morphology and topography for the satellites, the important structural properties of Saturn's rings are particle size, shape, and spatial distribution. For this reason, the Galilean satellites and Saturn's rings are discussed in separate chapters.

The final sections of this introductory chapter review basic concepts and techniques of radar astronomy, originally developed in the context of the radar behavior of the inner planets. Chapter II is devoted to the Galilean satellites. Although comparable in size to the smallest inner planets, the moons of Jupiter exhibit profoundly different radar properties. In particular, the circular polarization of echoes from Europa, Ganymede, and Callisto is unusual in the extreme. Much of Chapter II is concerned with discussion of this effect and its possible explanation in terms of scattering from a cratered, icy surface.

Saturn's rings form the subject of Chapter III. Although the composition of ring particles may resemble that of Europa's surface, no <u>single</u> radar result can be described as "anomalous". Rather, the dilemma here is reconciliation of the results of many radar observations made at different wavelengths, in different polarization senses, and at different ring-plane tilt angles. Chapter III begins with three sections describing all Saturn's rings radar observations undertaken to date, with minimal discussion of results. The final five sections of Chapter III contain discussions of particular radar properties of the rings and my inferences of ring structure.

In order to preserve the continuity of the text, I have relegated the more mathematical material to appendices.

I. B. Techniques of radar astronomy and application to inner solar system bodies

There exist several excellent descriptions of fundamental techniques of radar astronomy (e.g., Evans and Hagfors, 1968; Pettengill, 1970). The more important radar-astronomical concepts and definitions are developed in Appendix A.

The observational work for this thesis was done at the National Astronomy and Ionosphere Center in Arecibo, Puerto Rico, employing the S-band radar system described in Appendix B. The observations generally involved transmission of a highly monochromatic 2380 MHz (12.6-cm wavelength) CW wave for a duration on the order of the round-trip light-travel time to the target, followed by reception of the Doppler-shifted echo. Since each coherently reflecting element of the target contributes echo at a particular Doppler shift, and the received wave is a summation of such contributions, each of which is largely incoherent with the others, the echo is spread out in frequency. This is indicated in Fig. 1 for CW observation of a rotating spherical target.

Most of the observations involved circularly polarized transmission with reception switched periodically between the two orthogonal rotational senses of circular polarization. Thus, a typical night's data consisted of power spectra corresponding to two orthogonal polarizations. From these, radar scattering laws, cross sections, geometric albedo and polarization ratios for the targets were derived.

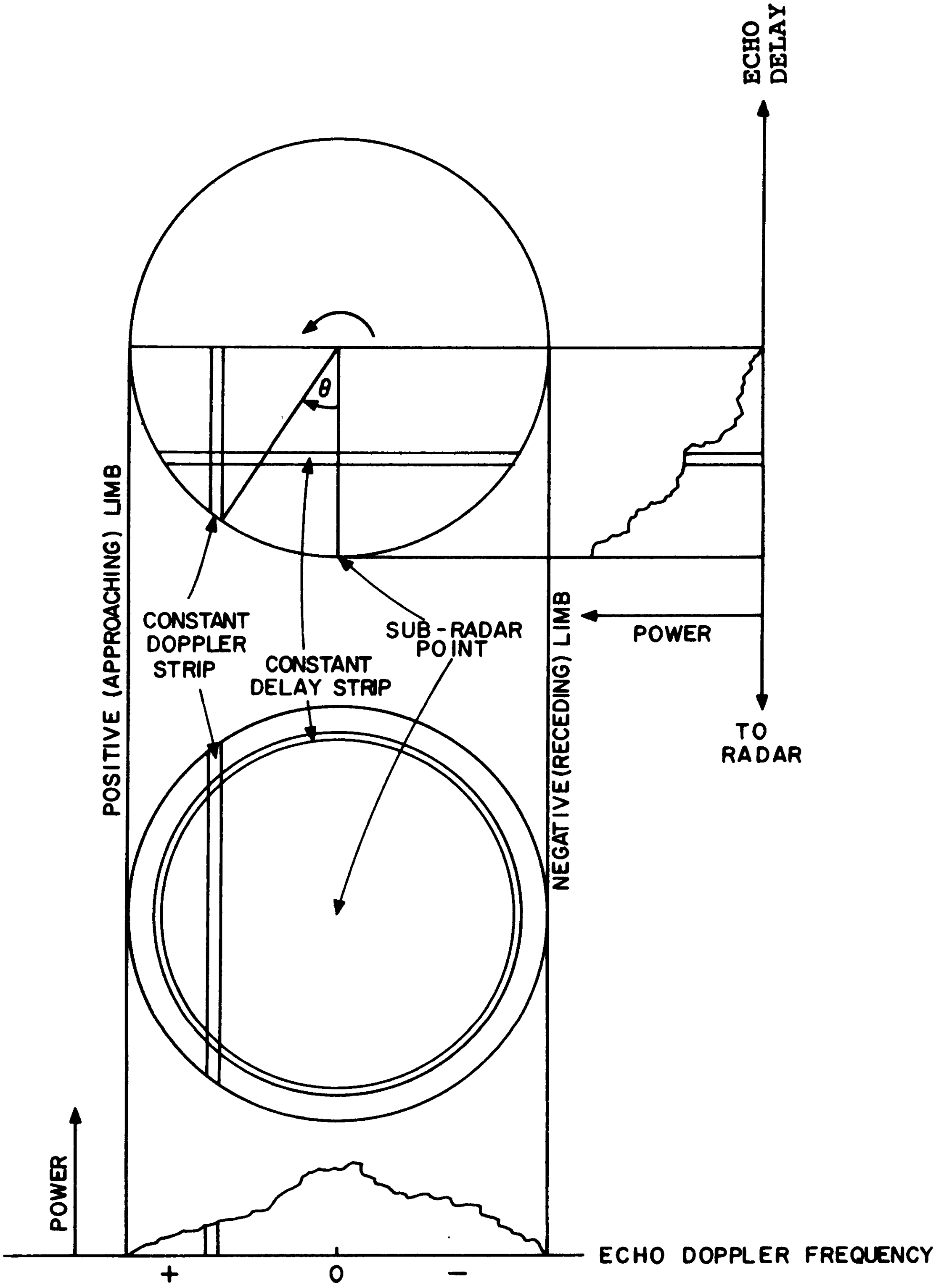

Fig. 1. Delay and Doppler resolution of a spherical target.

Radar cross section is defined in Appendix A while the formalism for dealing with polarization properties is developed in Appendix G. The ratios between orthogonally polarized echo components observed using circular and linear polarizations are defined here as:

$$\mu_C = \sigma_{SC}/\sigma_{OC} \text{ , circularly polarized transmission}$$

$$\mu_L = \sigma_{OL}/\sigma_{SL} \text{ , linearly polarized transmission}$$

where "C" and "L" are abbreviations for "circular" and "linear"; "O" and "S" designate polarization senses "orthogonal to" and "same as" that transmitted, and σ denotes radar cross section.

Any measurement of linear polarization properties may involve identification of the position angle between the polarization plane of the transmitted wave and, say, the target's apparent projected rotation axis. However, throughout this thesis I will assume that μ_L is independent of this position angle. This is equivalent to assuming that the whole-target scattering matrix is diagonal (Appendices G, H, and I). This is a reasonable assumption, although no experiments have been performed to determine the extent of its validity. For my purposes here, the above definition of μ_L is certainly adequate.

The total ("T") radar cross section is the sum of cross sections in two orthogonal polarizations:

$$\sigma_T = \begin{cases} \sigma_{TC} = \sigma_{OC} + \sigma_{SC} \\ \text{or} \\ \sigma_{TL} = \sigma_{OL} + \sigma_{SL} \end{cases}$$

where $\sigma_{TC} = \sigma_{TL}$ follows from my assumption that the target scattering matrix is diagonal. As shown in Appendix A, the radar geometric albedo α is defined by

$$\alpha = \sigma_T \; / \; (4\underline{A}_p)$$

where $\underline{A}_p$ is the target projected area.

For the Galilean satellites, $\underline{A}_p = \pi \underline{R}^2$, where $\underline{R}$ is the radius derived from optical measurements by Morrison and Cruikshank (1974): 1820, 1550, 2635, and 2500 km for Io, Europa, Ganymede, and Callisto, respectively. In the case of Saturn's rings, $\underline{A}_p$ will correspond to the visible projected area of the A and B rings (Appendix K).

I will use the term "normalized cross section" to denote $\sigma/\underline{A}_p$ and the term "absolute cross section" to denote σ. The above polarization ratios have been defined so that (μ_L, μ_C) would be (0,0) for any coherent, single-surface backscattering event, such as reflection from an infinite plane mirror whose normal is parallel to the line of sight, or from a perfectly smooth sphere; (1/3, 1) for reflection from a distribution of randomly oriented dipoles (Long, 1965); or (1,1) in the limit of complete depolarization of the transmitted wave.

During the last two decades, much effort has been devoted to theoretical explanation of radar scattering from the inner planets. Although the gross radar scattering properties of outer solar system bodies have very little in common with those of the inner planets, a brief review of the latter is an appropriate starting point for discussion.

It has proven convenient to divide the radar echo from the inner planets into components on the basis of their polarization and/or angular scattering properties (Appendix A), as illustrated in Fig. 2. On one hand, the echo can be divided into a "polarized" or coherently reflected portion and a "depolarized" or incoherently scattered portion. By "polarized" I imply the "SL" polarization for a linearly polarized transmission or "OC" for a circularly polarized transmission. The polarization ratios for the inner planets typically lie between 0.01 and 0.1, with μ_C generally larger than μ_L.

On the other hand, one can also separate echo components on the basis of the source mechanism involved. The "quasispecular" portion is completely polarized, drops off rapidly as the angle of incidence to the local surface increases and arises from single-surface reflection from a gently undulating surface. The "diffuse" portion is largely depolarized, drops off as $\cos^n\theta$ from the subradar point (where $\underline{n} \sim 3/2$ and θ is angle of incidence), and is caused by multiple scattering or scattering from surface components comparable in size with the radar wavelength.

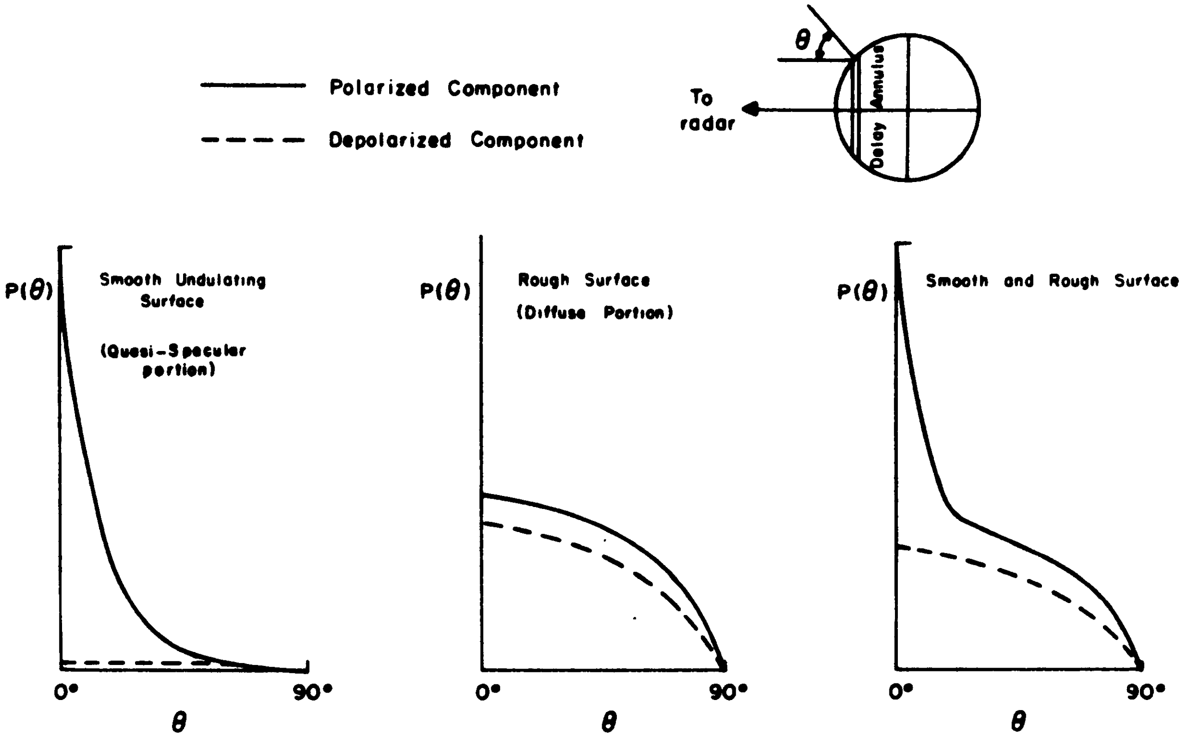

Fig. 2. Typical delay distribution of echo power for an inner planet, broken down into polarized and depolarized components, and quasispecular and diffuse portions. (Fig. 3.1 of Thompson, 1965)

I. C. The "quasispecular" echo

This topic will be treated very briefly, as none of the targets which I have studied exhibit a quasispecular return on the basis of either their angular scattering law or their polarization ratio. For mathematical treatments of quasispecular-scattering models and extensive bibliographies on the subject, see Beckmann (1968), Hagfors (1968), and Simpson (1973).

The three most common methods used to describe scattering from "quasi-smooth" surfaces are the physical-optics scalar models, the physical-optics vector models, and geometrical optics models. Each approach involves some statistical description of the surface, defining either the distribution of surface heights and their lateral autocorrelation or the slope probability distribution. In the case of the geometrical optics approach, the distribution is that of facet orientations or sizes. The geometrical optics treatment assumes that each illuminated point of the target reflects the incident wave in the same manner as would an infinite plane tangent to the surface at the given point. That is, geometrical optics approximates the scattered field in the limit where the reflecting facet has dimensions large compared to the wavelength. On the other hand, physical optics approximates only the boundary conditions on the wave equation, which is solved using either the Helmholtz integral for a scalar solution or the Stratton-Chu integral for a vector solution. Each of these several approaches has been moderately successful in describing the exponential shape and low polarization ratios of the quasispecular portion of echoes from the inner planets.

I. D. The "diffuse" echo

The "diffuse portion" of the radar return from the inner planets is relatively depolarized ($0.1 \lesssim \mu_L < \mu_C \lesssim 0.6$) and exhibits a scattering law (Appendix A) proportional to $\cos^n\theta$ where, at least for the Moon and Venus, $1 \lesssim \underline{n} \lesssim 2$. Since the average angular scattering law is easily extracted from the delay distribution of echo power (Appendices A and D), and the Moon and Venus are the easiest astronomical targets to resolve in delay, it is not surprising that the diffuse scattering law and polarization behavior of these bodies have been studied extensively over a wide range of radar wavelengths, λ.

As wavelength decreases, the fraction of total backscattered power contained in the diffuse portion of the lunar echo increases. This is because the lunar regolith appears increasingly fine-structured (rougher) as the illuminating wavelength decreases. Thus it tends to show a backscattered <u>intensity</u> proportional both to the power incident on unit geometric area as well as to projected area (i.e., constant brightness per unit illumination), corresponding to a specific radar scattering cross section $\sigma_o(\theta) \sim \cos^2\theta$, as noted in Appendix A. This so-called "Lambert law of diffuse reflection" is obeyed rather well at visible wavelengths by certain fine-grained papers. It is also a crude "first approximation" to exact solutions of the equation of transfer (Chandrasekhar, 1950, p. 146) for reflection from a semiinfinite atmosphere.

The exponent in the diffuse-portion scattering law from a real, physical surface might be closer to 1 than to 2 because of, for instance, the precise geometry of shadowing (Hapke, 1963). For the Moon, Hagfors and Evans (1968) reported that at wavelengths λ equal to 0.8 and 3.6 cm, $\underline{n} \approx 1$, but at wavelengths $\lambda \geqslant 23$ cm, $\underline{n} \approx 1.5$. At optical wavelengths, the entire Moon is uniformly bright, corresponding to $\underline{n} \approx 1$. In general, $\underline{n}$ will depend on the scattering law (bistatic phase function) for single scattering, the single scattering albedo, the relative importance of multiple scattering, the type of shadowing geometry, and the thickness, both physical and optical, of the scattering layer(s).

The diffuse portion of lunar and Venus radar echoes is largely depolarized. That is, the ratios μ_C and μ_L are much larger than for the echo as a whole, although significantly less than unity. The angular dependence of μ_C and μ_L for large angles of incidence ($\theta \geqslant 70^o$), where the diffuse portion dominates, is very small for the Moon at $\lambda = 23$ cm and 70 cm, and for Venus at $\lambda = 70$ cm according to Hagfors and Campbell (1974). They note that the circular polarization ratio levels off at 0.25 for Venus at $\lambda = 70$ cm. For the Moon, μ_C levels off at 0.4 for $\lambda = 70$ cm and at 0.55 for $\lambda = 23$ cm.

The depolarization of the diffuse portion has been attributed to single-scattering depolarization (e.g., Beckmann, 1968, p. 191), multiple scattering (Pollack and Whitehill, 1972; Fung, 1967), reflection from layered media (Hagfors and Evans, 1968), and reflection from large-scale surface structure (Hagfors and Campbell, 1974). Of course, more than one scattering process may be responsible for the polarization behavior of a real surface. The important point here is that there exists a plethora of reasonable explanations for the polarization properties of the inner planets. As discussed in the next chapter, such is not the case for three of the Galilean satellites.

II. THE GALILEAN SATELLITES

II. A. Radar picture of the satellite surfaces prior to thesis work

Goldstein and Morris (1975) reported the first radar detection of Ganymede in late August 1974, using the Jet Propulsion Laboratory's 12.6-cm radar system to determine σ_{OC}. Their six-night average (normalized) value for σ_{OC}, 0.12 ± 0.025, is at least as large as any for the inner planets. Their average spectrum (Fig. 3a) is very noisy but is clearly much broader than polarized-mode spectra for the inner planets (Fig. 4).

By fitting a model (Appendix D) based on a $\cos^n\theta$ scattering law to the spectrum, Goldstein and Morris obtain a best estimate for $\underline{n}_R$ of 10. As denoted by the "R" subscript, they constrained Ganymede's radius to the optically determined value: 2635 km, during the estimation. They define a "half-power angle of incidence" θ_{HP} by the equation: $\cos^n\theta_{HP} = 1/2$. The power backscattered from an average surface element whose normal points toward the radar ($\theta = 0°$) would drop by 50% when tilted so $\theta = \theta_{HP}$. For $\underline{n} = \underline{n}_R = 10$, the half-power angle has a value $\theta_{HP} = 21°$.

Goldstein and Morris point out that the half-power angles for the inner planets have values between 1° and 8°, such as would result from $\cos^n\theta$ scattering laws with the exponent between ~70 and ~4000. They claim that the

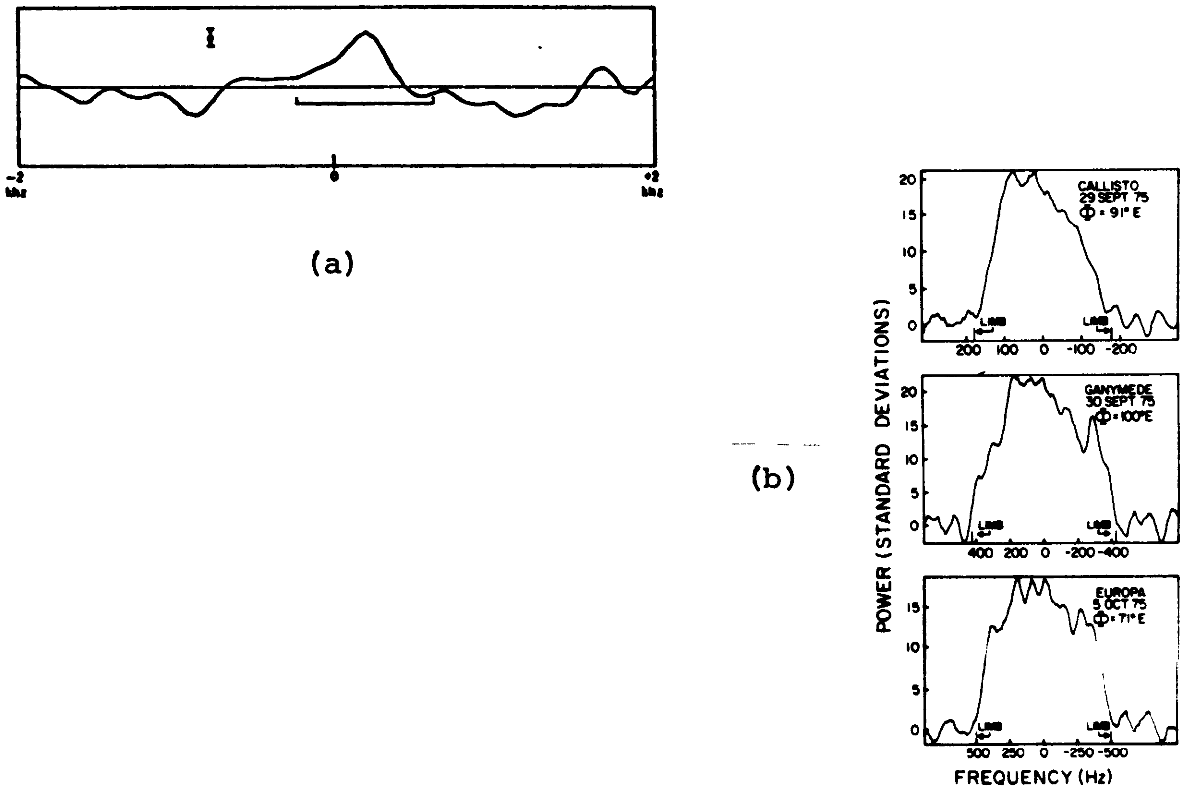

(a)

(b)

Fig. 3. (a) is the six-night average Ganymede "OC" spectrum obtained by Goldstein and Morris (1975). (b) shows selected "SL" spectra taken by Campbell et al. (1977). The latter have been filtered to a resolution of 10% $\underline{f}_{LL}$ (see text).

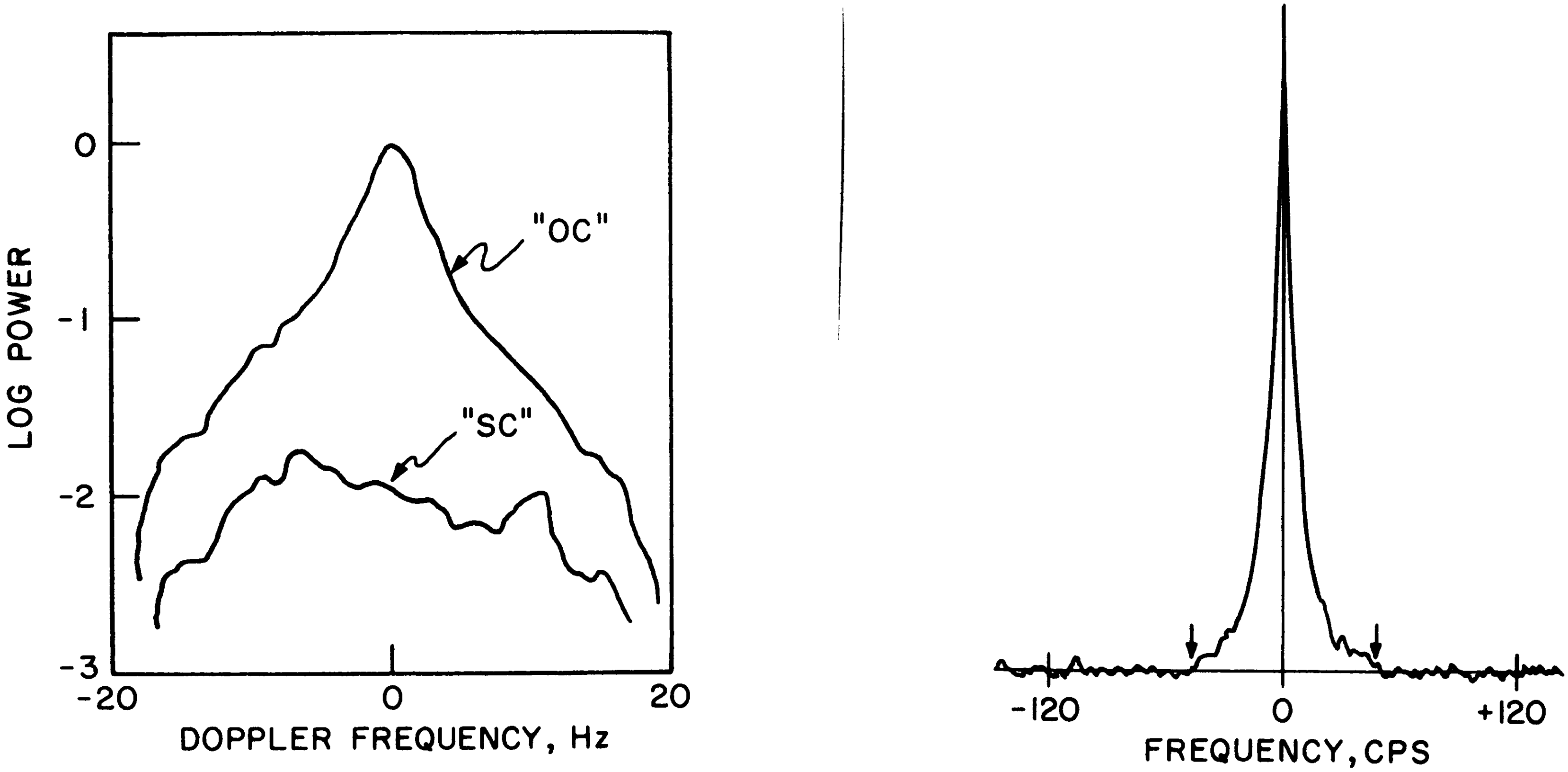

Fig 4. (a) Venus 12.6-cm spectra in orthogonal circular polarizations, after Carpenter (1966). Note the log-scale ordinate.

(b) Mercury 12.6-cm "OC" spectrum after Goldstein (1971). Here a linear-scale ordinate is used, and arrows show theoretical limb position.

relatively high value of θ_{HP} for Ganymede is a demonstration of that body's much greater relative roughness. Although this basic conclusion is certainly correct, the $\cos^n\theta$ monostatic scattering law is merely an empirical convenience, as discussed in Appendix D, and the physical assumptions implicit in its usage break down for $n \gg 1$.

Prior to these radar observations, there had developed a firm consensus that water ice is a major constituent of the surfaces of the outer three Galilean satellites: Europa, Ganymede, and Callisto. This was based on near-infrared (1.0-2.5μ) reflectances (Kuiper, 1957; Moroz, 1965; Gromova et al., 1970; Johnson and McCord, 1971; Lee, 1972; Pilcher et al., 1972; and Fink et al., 1973). Goldstein and Morris (1975) speculated that perhaps the most likely explanation of their Ganymede results was a surface consisting of a "rocky or metallic material embedded in a matrix of ice."

The first systematic study (Campbell et al., 1977, hereafter referred to as CCPS) was undertaken when Jupiter next reached opposition, in autumn 1975. Donald Campbell of NAIC and Gordon Pettengill, Irwin Shapiro and John Chandler of MIT employed the newly improved Arecibo S-band (12.6-cm) radar to observe one satellite per night on 12 nights between September 1975 and January 1976. They used the linearly polarized "flat feed" (Appendix B) adjusted to receive in either the "SL" or the "OL" sense on any given night. Their typical spectra (Fig. 3b) for the outer three satellites are very broad for <u>each</u> polarization. Although μ_L was not determined directly at a specific value of orbital phase Φ, it can be inferred to be approximately 0.5 from the single-polarization cross sections σ_{OL} and σ_{SL}, obtained at different Φ. A similar approach to deriving values of radar geometric albedo leads to $\alpha = 0.42 \pm 0.10$, 0.20 ± 0.05, and 0.09 ± 0.02 for Europa, Ganymede, and Callisto, respectively. CCPS note

> Curiously, the radar cross sections we obtained for Europa, Ganymede, and Callisto show nearly the same relative values as do the optical cross sections (Newburn and Gulkis, 1973; Morrison and Cruikshank, 1974), despite the presumably far deeper penetration into the surface by the radio waves. Perhaps the surface material is reasonably homogeneous to a depth of at least 1 m. Also, the extremely diffuse scattering of radio waves from these surfaces, compared to that from the terrestrial planets, may indicate that erosive smoothing processes on the Galilean satellites are negligible or that substantial internal reflection is occurring within the surface material.

They further note that the trend in albedos is similar to the trend in fractional frost coverage of the satellites, as estimated by Pilcher <u>et al</u>. (1972) and Fink <u>et al</u>. (1973).

Table I is based on Table I of CCPS and gives the pertinent quantitative results of their observations. For reasons described below, their estimates of radii and <u>n</u> are not included. CCPS's least-squares estimates of $\underline{n}_R$ are much smaller than the value estimated by Goldstein and Morris (1975), while the former's weighted mean value of $\sigma_{SL} = 0.5$ is, inexplicably, four times larger than the value of σ_{OC}

TABLE I. Results of the 1975 observations by Campbell *et al*. (1977), based on Table I in that paper.

Target	Date	Φ	Pol'n	n_R	σ (πR^2)	α	μ_L
Io	16 Jan 76	274°	SL		0.3 ±0.1		
Europa	5 Oct 75	71°	SL	1.1±0.2	1.18±0.30		
	27 Oct 75	137°	OL	1.4±0.4	0.49±0.12		
(Europa weighted means)			TL	1.2±0.2		0.42±0.10	0.42±0.15
Ganymede	30 Sep 75	100°	SL	1.4±0.2	0.44±0.11		
	1 Oct 75	150°	SL	1.9±0.3	0.53±0.13		
	1 Nov 75	269°	OL	1.5±0.3	0.30±0.08		
(Ganymede weighted means)			TL	1.5±0.1		0.20±0.05	0.62±0.22
Callisto	28 Sep 75	70°	SL	1.8±0.4	0.27±0.07		
	29 Sep 75	91°	SL	2.1±0.3	0.28±0.07		
	28 Oct 75	0°	SL	1.5±0.3	0.25±0.06		
	30 Oct 75	43°	OL	3.7±1.0	0.11±0.03		
(Callisto weighted means)			TL	1.9±0.2		0.09±0.02	0.41±0.14

reported by the latter group.

CCPS note that the high degree of depolarization and the broad spectra of the outer three satellites are consistent with diffuse scattering from a rough surface, and that these properties plus the very large albedo of Europa would lead one to expect a rough, icy surface for that satellite. Also, CCPS point out that "the spectra of both Ganymede and Callisto are significantly skewed as though one side of each planet as viewed from the earth was more reflective than the other."

CCPS measured $\sigma_{SL} = 0.3 \pm 0.1$ for Io, which was detected only once in three attempts.

In summary, the following major radar properties of the Galilean satellites had been determined prior to the 1976 Jupiter opposition:

1. Europa, Ganymede, and Callisto, as a <u>class</u> of radar targets, are much more efficient backscatterers of 12.6-cm waves than the inner planets.
2. The radar scattering from the satellites is <u>diffuse</u>, with <u>no trace</u> of a quasispecular component.
3. Radar echoes from the outer three satellites are highly depolarized. The ratio μ_L is similar in magnitude to that for the diffuse portion of the lunar echo.
4. Radar geometric albedo, optical geometric albedo, and fractional coverage by water frost are correlated for the outer three satellites.

5. Io stands alone among the Galilean satellites as a relatively weak backscatterer of radar waves. It certainly must be considered separately.

II. B. Observations of the Galilean satellites, 1976-1977: Experimental procedure and data analysis

The 1975 radar results of CCPS established the importance of determining the geometric albedo and polarizing properties of Europa, Ganymede, and Callisto, as accurately and over as wide a range of orbital phase as possible. These bodies were found to be unexpectedly intense radar scatterers; thus, the polarization ratios were relatively easy to measure. As demonstrated for the Moon and Venus (e.g. Pettengill, 1968, p. 310), the polarization of scattered radiation provides significant insight into surface structure. The Galilean satellites, unlike the Moon and Venus, are equally accessible to radar study at all longitudes. Consequently, measurement of α, μ_C, and μ_L as a function of orbital phase proved a straightforward task, at least for the outer three satellites. As we shall see, Io proved the black sheep in this fold, and has presented unusual difficulties to radar observation.

The 1976 and 1977 experiments employed a new "circular" antenna feed, more efficient than that used in 1975 (Appendix B), and capable of receiving simultaneously in two orthogonal senses of either linear or circular polarization. Since circular polarization obviates problems with Faraday rotation (although these are not severe at S-band, the wavelength used in these observations), the quantities σ_{OC}, σ_{SC} and μ_C are somewhat easier to measure than σ_{OL}, σ_{SL} and μ_L. Observations using circular polarization were undertaken in late

1976 and late 1977 at Arecibo by Pettengill, Shapiro and myself from MIT and Campbell from NAIC. The 1976 work has been reported by Campbell *et al.* (1978), hereafter referred to as CCOPS. The 1977 results (Ostro, *et al.*, 1979) are presented in this thesis, for the first time.

The rest of this section will be devoted to a description of the 1976-1977 observations and data analysis. Results of the two studies, which were similar in objectives, will then be combined for discussion.

Observational parameters and system characteristics for the 1976 and 1977 observations are listed in Table II. Eleven nights were available in each year. A given night's observation consisted of about one hour of simple carrier (CW) transmission followed by reception of the echo for a similar duration. The round-trip flight time to Jupiter on the dates of observation was about 70 minutes in each case.

The transmitter carrier frequency was switched among two or more frequencies separated by several kilohertz, to facilitate correction for the background filter shape in analyzing echo spectra (Appendix B). During reception, the sense of polarization was switched between the "OC" and "SC" senses at a rate slow compared to that for frequency switching.

In 1977, a computer controlled the polarization switching and coordinated the integration and output of data (real-time spectra from an on-line array processor) with the echo-delayed frequency-switching cycle. It also managed the injection of a 3.6 K calibration noise pulse into the receiver

TABLE II. Observational parameters and system characteristics for 1976 and 1977 observations of the Galilean satellites at Arecibo.

	1976	1977
One-way antenna gain at zenith	70.54 dB	70.54 dB
Cold sky system temperature at zenith		
"OC" port	41 °K	38 °K
"SC" port	38 °K	36 °K
Antenna one-way beamwidth, full width at half power	2' arc	2' arc
Average transmitter power	350 kw	350 kw
Number of transmitter frequencies per cycle	2	4
Time at each frequency	30 sec	10 sec
Polarization switching control	manual	computer
Time at each polarization per cycle	240 sec	80 sec
Raw data	3-level by 3-level autocorrelation function	power spectrum from array processor
Total analyzing bandwidth in final spectra		
outer satellites	2 kHz	4 kHz
Io	4 kHz	8 kHz
Unsmoothed frequency resolution		
outer satellites	19.4 Hz	9.8 Hz

during the first half-period of reception in each polarization. The 1977 data set therefore consisted of 16 different types of spectra (four frequencies times two polarizations times two calibration states).

To facilitate integration and sorting of data, every ten-second data record was identified with its start time, stop time, polarization, calibration state (on or off), antenna-pointing coordinates, and ephemeris echo delay. Furthermore, to avoid interrupting transmission and reception in order to monitor tracking accuracy (using Jupiter's intrinsic radio emission), antenna tracking was checked using radio sources at the same declination as Jupiter prior to the radar observations.

The above measures, designed to optimize the accuracy of the 1977 determinations of albedo and circular polarization ratio, were based on observing experience gained in 1976. As will be discussed later, values of μ_C and α determined in 1976 for Europa, Ganymede, and Callisto were much larger than had been anticipated.

Because of the unexpectedly large values of μ_C obtained for the outer three satellites, special attention was given to checking the radar system's polarization. This attention took two forms: (1) verifying that the receiving system was actually switching between the desired antenna ports at the correct times; and (2) ensuring that the antenna polarization was, in fact, highly circular. The first point was verified by carrying out two sets of identically structured observations of Europa, the first with the feed adjusted for circular polarization and the second with the feed set for linear polarization. In both cases the power received from the nominal transmitting ("same") port exceeded that received from its orthogonal ("opposite") partner. Observation of leakage from the transmitter verified that the nominal assignments were correct. The degree of circularity of the transmitted and received polarization has been determined both by measurement during construction of the feed and by observation of Venus, whose echoes are known, and were observed, to yield a value of μ_C equal to a few percent (Goldstein, 1970).

Power spectra of echoes obtained in 1976 and 1977 are shown in Figs. 5 and 6, respectively. Spectra for the outer three satellites are smoothed to 10% of the *a priori* limb-to-limb bandwidth, $\underline{f}_{LL}$, as discussed and derived in Appendices D and F.

The 1976 Io spectra, smoothed to 0.2 $\underline{f}_{LL}$, are extremely weak. In 1977, with an improved data-taking system, Io could not be reliably detected (echoes did not exceed five standard deviations, i.e., 5σ, of the accompanying noise fluctuations) in any of three attempts. From 1975 through 1977, Io has been "detected" at a 3σ to 4σ level (0.2 $\underline{f}_{LL}$ resolution) at orbital phases Φ of 25°, 118°, 274° and 287°, but has remained undetected in observations made at $\Phi = 91°$, 151°, 139°, 204°, 243° and 285°. During the 1975, 1976 and 1977 oppositions, successively better systems have yielded estimates of Io's maximum geometric albedo approximating 0.08 (inferred from the σ_{SL} reported by CCPS), 0.04 (CCOPS), and 0.03, respectively. Given all these observational results, it seems possible that we have been mistaking noise for Io. Since the innermost Galilean satellite is barely detectable at best, very little can be said about its surface on the basis of radar observations, except that its albedo probably is no larger than those of the terrestrial planets.

On the other hand, as compared to Io, spectra of echoes from Europa, Ganymede, and Callisto are relatively strong in both polarizations. Parameters of a scattering law of the form $\cos^n\theta$ were estimated from the (unsmoothed) observed power spectra, grouped according to receiver polarization. Weighted-least-squares estimates of the radar cross section σ', the exponent $\underline{n}_R$, and Doppler shift ν_R of the model's center frequency were obtained as described in Appendices E and F. As denoted by the subscript "R", the target radius was constrained to a value derived from optical measurements (Morrison and Cruikshank, 1974): 1550, 2635, and 2500 km for Europa, Ganymede, and Callisto, respectively. Since $\underline{n}$ is highly correlated with $\underline{R}$ and σ', $\underline{n}_R$ probably characterizes surface scattering properties better than $\underline{n}$. As discussed in detail by Jurgens and Bender (1977), simultaneous estimation of $\underline{n}$ and $\underline{R}$ may be very difficult, and "often fails to converge [sic] when the signal-to-noise ratio is below a certain threshold. Convergence, in such cases, may be achieved by reducing the number of free parameters in the estimation...."

A separate estimate of radar cross section σ was obtained by simple integration of the observed signal power over an appropriate portion of the received spectrum. The latter method is considered more reliable for estimating cross section than the former, and only values of σ obtained in this way will be quoted here. As derived in Appendix A, geometric albedo α is equal to one-fourth the normalized cross section.

In the spectra in Figs. 5 and 6, Doppler frequency is plotted relative to the Doppler shift of the estimated center frequency ν_R. Best estimates of ν_R for each night in 1977 are given in Table III. Four figures are shown for each 1977 observation: (a) smoothed spectra taken in "OC" and "SC" polarization senses, (b) a smoothed "TC" spectrum with 0.1 $\underline{f}_{LL}$ resolution, (c) a raw "TC" spectrum with 9 Hz resolution, and (d) an optimally fitted, three-parameter (σ', $\underline{n}_R$, ν_R) model superimposed on the curve in (c).

Tables IV and V give the values of $\underline{n}_R$, σ, and α at each polarization for each night. Radar cross sections have been assigned errors of one-fourth their value to reflect estimated uncertainties associated with system antenna gain, temperature, and transmitted power, which generally dominate statistical fluctuations (Appendix C).

The uncertainties shown for $\underline{n}_R$ and ν_R are derived by a uniform scaling of measurement errors such that the weighted-mean-square of the post-fit residuals equals unity (Appendix C). The scaling factor required is within 10% of unity, except for the Ganymede data of 22 Nov 76, for which it is 1.5. The relatively small deviations of these factors from unity lend support to the validity of the model. Minimum uncertainties equal to 0.2 $\underline{f}_{LL}$ have been assigned to the Doppler shift estimates to protect against systematic errors which may be introduced by the use of a simple symmetric scattering law to represent spectra which are not, in fact, symmetrical.

Also shown for Europa, Ganymede, and Callisto is the polarization ratio μ_C, determined from each night's data except for 7 Dec 76, when μ_L was measured for Europa. The quoted uncertainty in μ has been obtained from the dispersion observed among the results from the separate segments of data obtained in each night's measurements. The 1976 data consisted, nominally, of four (4-minute) spectra at each polarization. The 1977 data consisted of ten (200-second) spectra at each polarization.

TABLE III. Galilean satellites 1977 radar results: Doppler shifts.

Target	Date (1977)	Φ	Mean time of reception (UTC) h m	Duration of observation (min)	Doppler shift for 2380 MHz transmission (Hz)
Europa	23 Nov	236°	07 11	48.9	51,847±20
Europa	27 Nov	281°	06 59	62.7	-14,395±20
Ganymede	25 Nov	30°	07 05	30.7	301,851±17
Ganymede	20 Nov	138°	07 22	62.7	365,350±17
Ganymede	22 Nov	239°	07 16	61.4	88,208±17
Callisto	21 Nov	12°	07 17	62.7	269,725 ± 7
Callisto	26 Nov	120°	07 05	59.3	322,706 ± 7
Callisto	15 Nov	243°	07 46	46.7	165,787 ± 7

TABLE IV. Galilean satellites 1976 radar results: cross sections, albedos, polarization ratios and scattering law exponents (see text). Here, τ is duration of observation and μ is to be interpreted as either μ_C or μ_L.

Target	Date (1976)	Φ	Pol'n	τ (min)	n_R	σ (πR^2)	α	μ
Io	15 Nov	25°	OC	37	6±5	0.18±0.04		
Io	19 Nov	118°	OC	20	12±9	0.14±0.03		
			SC	15		<0.06		
Io	26 Oct	287°	OC	16	14±8	0.20±0.04		
			SC	16		<0.05		
(Io weighted means)					10±4	0.17±0.04	~0.04±0.01	
Europa	20 Nov	39°	OC	17	2.1±0.3	1.03±0.26		
			SC	18	1.9±0.2	1.80±0.45		
			TC		2.0±0.2		0.71±0.18	1.75±0.29
Europa	25 Nov	185°	OC	21	1.5±0.3	1.18±0.30		
			SC	17	2.0±0.3	1.73±0.43		
			TC		1.8±0.2		0.73±0.18	1.47±0.28
(Europa weighted means, circular pol'n only)			OC		1.8±0.2	1.11±0.28		
			SC		1.9±0.2	1.77±0.44		
			TC		1.9±0.1		0.72±0.18	1.61±0.20
Europa	7 Dec	319°	OL	13	1.6±0.4	0.81±0.20		
			SL	11	1.4±0.2	1.68±0.42		
			TL		1.5±0.2		0.62±0.16	0.48±0.08
(Europa weighted means, circular and linear pol'ns)			TC+TL		1.8±0.1		0.69±0.17	

TABLE IV, continued

Target	Date (1976)	ϕ	Pol'n	τ (min)	n_R	σ	α	μ
Ganymede	18 Nov	65°	OC	18	2.0±0.1	0.62±0.15		
			SC	18	1.6±0.1	0.93±0.23		
			TC		1.8±0.1		0.39±0.10	1.52±0.29
Ganymede	22 Nov	266°	OC	7	1.6±0.2	0.58±0.14		
			SC	5	1.3±0.3	0.71±0.18		
			TC		1.4±0.2		0.32±0.08	1.23±0.77
(Ganymede weighted means)			OC		1.9±0.1	0.61±0.15		
			SC		1.6±0.1	0.88±0.22		
			TC		1.7 0.1		0.37±0.09	1.48±0.27
Callisto	19 Nov	102°	OC	7	1.7±0.4	0.20±0.05		
			SC	29	1.4±0.1	0.32±0.09		
			TC		1.5±0.1		0.13±0.04	1.61±0.57
Callisto	27 Nov	225°	OC	15	1.8±0.2	0.30±0.07		
			SC	19	2.0±0.2	0.33±0.08		
			TC		1.9±0.1		0.16±0.04	1.12±0.24
Callisto	14 Nov	304°	OC	19	1.2±0.2	0.22±0.05		
			SC	11	1.2±0.2	0.31±0.08		
			TC		1.2±0.2		0.13±0.03	1.39±0.40
(Callisto weighted means)			OC		1.5±0.1	0.25±0.06		
			SC		1.5±0.1	0.33±0.08		
			TC		1.6±0.1		0.15±0.04	1.24±0.19

TABLE V. Galilean satellites 1977 radar results: cross sections, albedos, polarization ratios and scattering law exponents.

Target	Date	Φ	Pol'n	n_R	σ (πR^2)	α	μ_C
Europa	23 Nov 77	236°	OC	1.6±0.3	0.96±0.24		
			SC	1.9±0.2	1.54±0.39		
			TC	1.8±0.2		0.62±0.16	1.60±0.47
Europa	27 Nov 77	281°	OC	1.9±0.3	0.88±0.22		
			SC	1.2±0.2	1.31±0.33		
			TC	1.4±0.1		0.55±0.14	1.49±0.36
(Europa weighted means)			OC	1.8±0.2	0.92±0.23		
			SC	1.5±0.1	1.41±0.35		
			TC	1.5±0.1		0.58±0.14	1.53±0.29
Ganymede	25 Nov 77	30°	OC	1.4±0.5	0.55±0.25		
			SC	1.3±0.3	0.78±0.23		
			TC	1.5±0.3		0.33±0.08	1.42±0.77
Ganymede	20 Nov 77	138°	OC	1.1±0.1	0.53±0.17		
			SC	0.8±0.1	0.88±0.22		
			TC	0.9±0.1		0.35±0.09	1.66±0.63
Ganymede	22 Nov 77	239°	OC	1.1±0.1	0.50±0.12		
			SC	1.2±0.1	0.74±0.18		
			TC	1.2±0.1		0.31 0.08	1.48 0.32
(Ganymede weighted means)			OC	1.1±0.1	0.52 0.13		
			SC	1.0±0.1	0.79 0.20		
			TC	1.1±0.1		0.33 0.08	1.51 0.27

TABLE V, continued

Target	Date	Φ	Pol'n	n_R	σ	α	μ_C
Callisto	21 Nov 77	12°	OC	1.6±0.2	0.29±0.07		
			SC	1.7±0.2	0.31±0.08		
			TC	1.6±0.2		0.15±0.04	1.07±0.30
Callisto	26 Nov 77	120°	OC	1.7±0.2	0.23±0.06		
			SC	1.5±0.2	0.30±0.08		
			TC	1.6±0.2		0.13±0.03	1.30±0.33
Callisto	15 Nov 77	243°	OC	1.5±0.3	0.29±0.07		
			SC	1.3±0.2	0.32±0.08		
			TC	1.4±0.2		0.15±0.04	1.10±0.23
(Callisto weighted means)			OC	1.6±0.1	0.27±0.07		
			SC	1.5±0.1	0.31±0.08		
			TC	1.5±0.1		0.14±0.04	1.14±0.16

Fig. 5. Spectra of radar echoes obtained in 1976 from the Galilean satellites. The center (zero) frequency corresponds to the estimated Doppler shift for echoes from the subradar point for each night (see text). A positive Doppler frequency corresponds to that portion of the surface which is approaching the observer as compared to the satellite's center of mass (i.e., which lies at greater west longitude as compared to the sub-Earth point). Each spectrum represents the sum of all data taken in a given polarization sense on the night specified. The ordinates are given in units of standard deviations of the associated noise. Dashed and solid lines connecting the observed data points are used to designate the results for "same" and "orthogonal" polarization senses, respectively. All data were taken using circular polarization except those shown in (f), for which linear was used. Each spectrum has been convolved with a smoothing filter whose resolution was 10% of the calculated limb-to-limb bandwidth, except for Io where 20% was used.

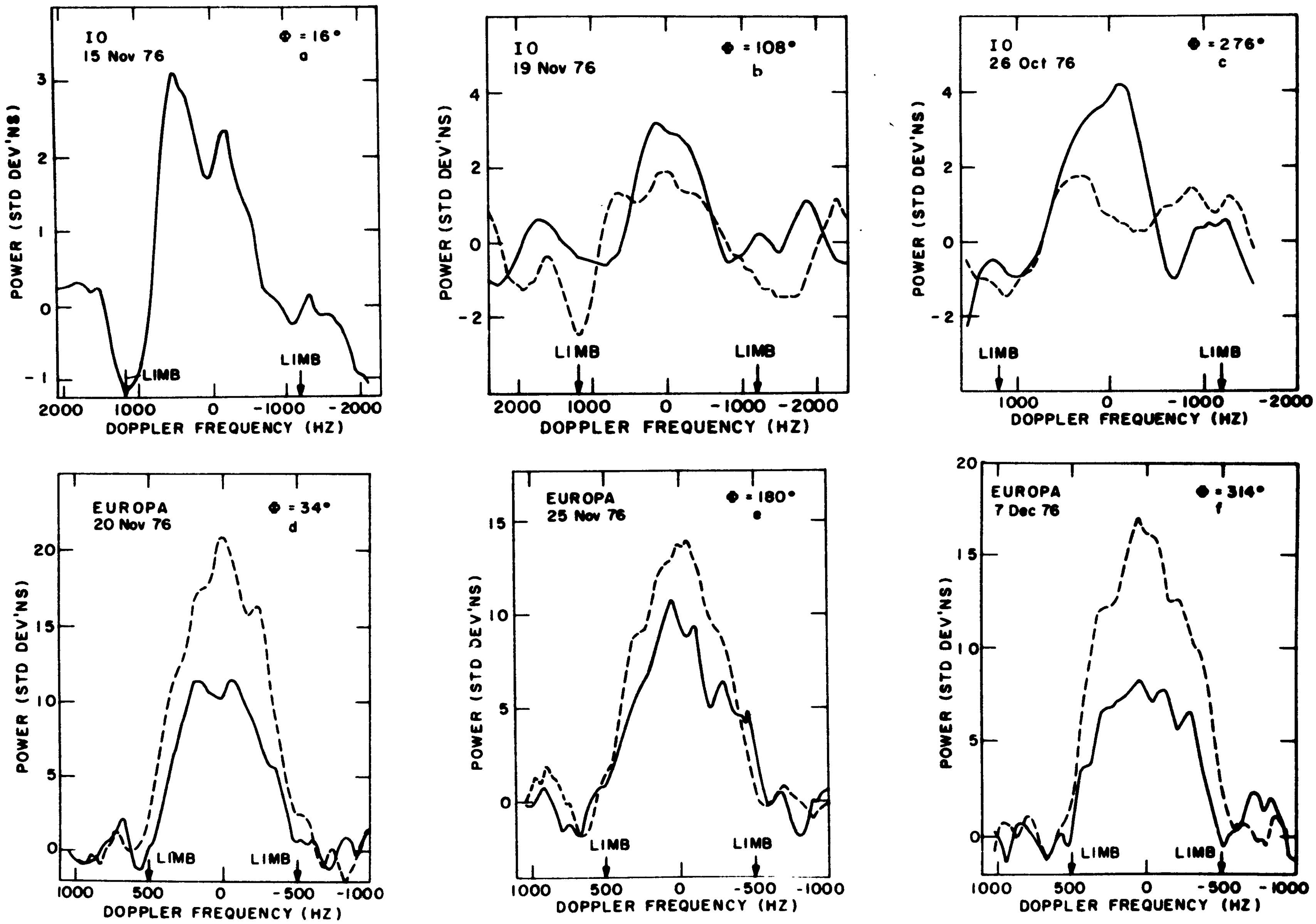
IO
15 Nov 76
Φ = 16°
a
IO
19 Nov 76
Φ = 108°
b
IO
26 Oct 76
Φ = 276°
c
EUROPA
20 Nov 76
Φ = 34°
d
EUROPA
25 Nov 76
Φ = 180°
e
EUROPA
7 Dec 76
Φ = 314°
f
POWER (STD DEV'NS)
DOPPLER FREQUENCY (HZ)
LIMB
LIMB
3
2
1
0
-1
2000
1000
0
-1000
-2000
4
2
0
-2
2000
1000
0
-1000
-2000
4
2
0
-2
1000
0
-1000
-2000
20
15
10
5
0
1000
500
0
-500
-1000
15
10
5
0
1000
500
0
-500
-1000
20
15
10
5
0
1000
500
0
-500
-1000

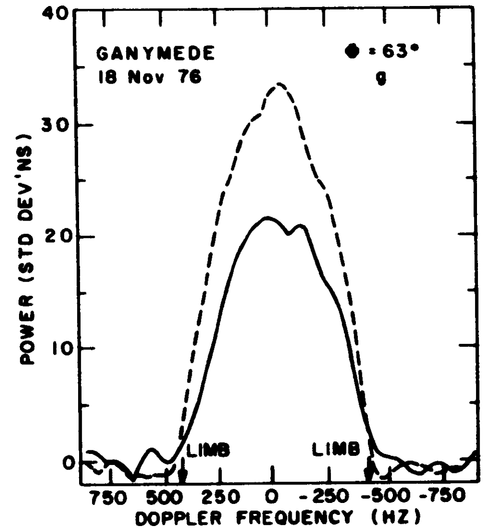
GANYMEDE
18 Nov 76
Φ = 63°
g
POWER (STD DEV'NS)
40
30
20
10
0
LIMB
LIMB
750 500 250 0 -250 -500 -750
DOPPLER FREQUENCY (HZ)

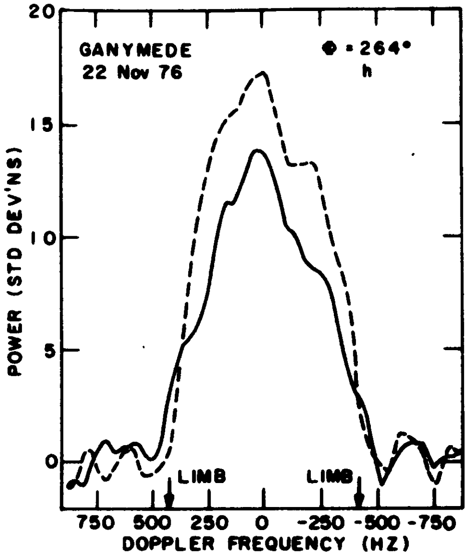
GANYMEDE
22 Nov 76
Φ = 264°
h
POWER (STD DEV'NS)
20
15
10
5
0
LIMB
LIMB
750 500 250 0 -250 -500 -750
DOPPLER FREQUENCY (HZ)

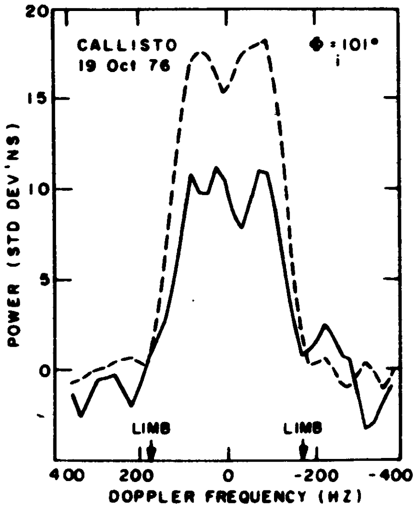
CALLISTO
19 Oct 76
Φ = 101°
i
POWER (STD DEV'NS)
20
15
10
5
0
LIMB
LIMB
400 200 0 -200 -400
DOPPLER FREQUENCY (HZ)

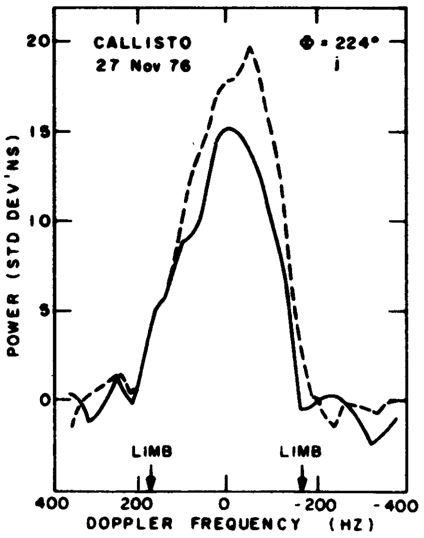
CALLISTO
27 Nov 76
Φ = 224°
j
POWER (STD DEV'NS)
20
15
10
5
0
LIMB
LIMB
400 200 0 -200 -400
DOPPLER FREQUENCY (HZ)

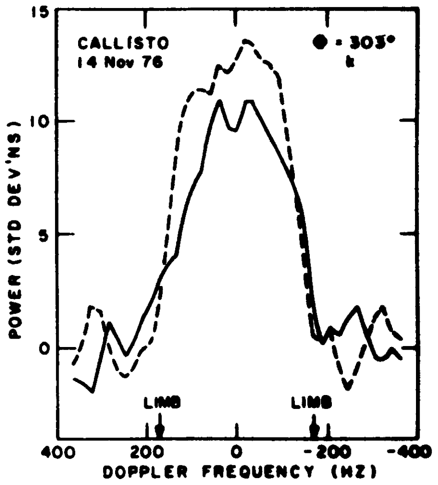
CALLISTO
14 Nov 76
Φ = 303°
k
POWER (STD DEV'NS)
15
10
5
0
LIMB
LIMB
400 200 0 -200 -400
DOPPLER FREQUENCY (HZ)

Fig. 6. Galilean satellites 1977 spectra. Results for each of eight nights are shown in four parts. (A) shows "OC" (light curve) and "SC" (dark curve) spectra, filtered to a resolution equal to 10% of the *a priori* limb-to-limb bandwidth (see text). (B) shows the filtered "TC" spectrum. (C) and (D) both show the raw "TC" spectrum. Best estimates of geometric albedo α, circular polarization ratio μ_C and scattering law exponent $\hat{\underline{n}}_R$ (for "TC" spectra) are given in the upper right-hand corner . The model spectrum corresponding to a scattering law with the exponent $\hat{\underline{n}}_R$ is superimposed on the raw "TC" spectrum in (D). The axes have the same meaning as in Fig. 5. Small vertical bars drawn at "-4 std dev's" designate theoretical limb positions.

EUROPA **236°** **23 Nov 77**

α = **0.62±0.16**

μ_c = **1.60±0.47**

$\hat{n}_R$ = **1.8 ±0.2**

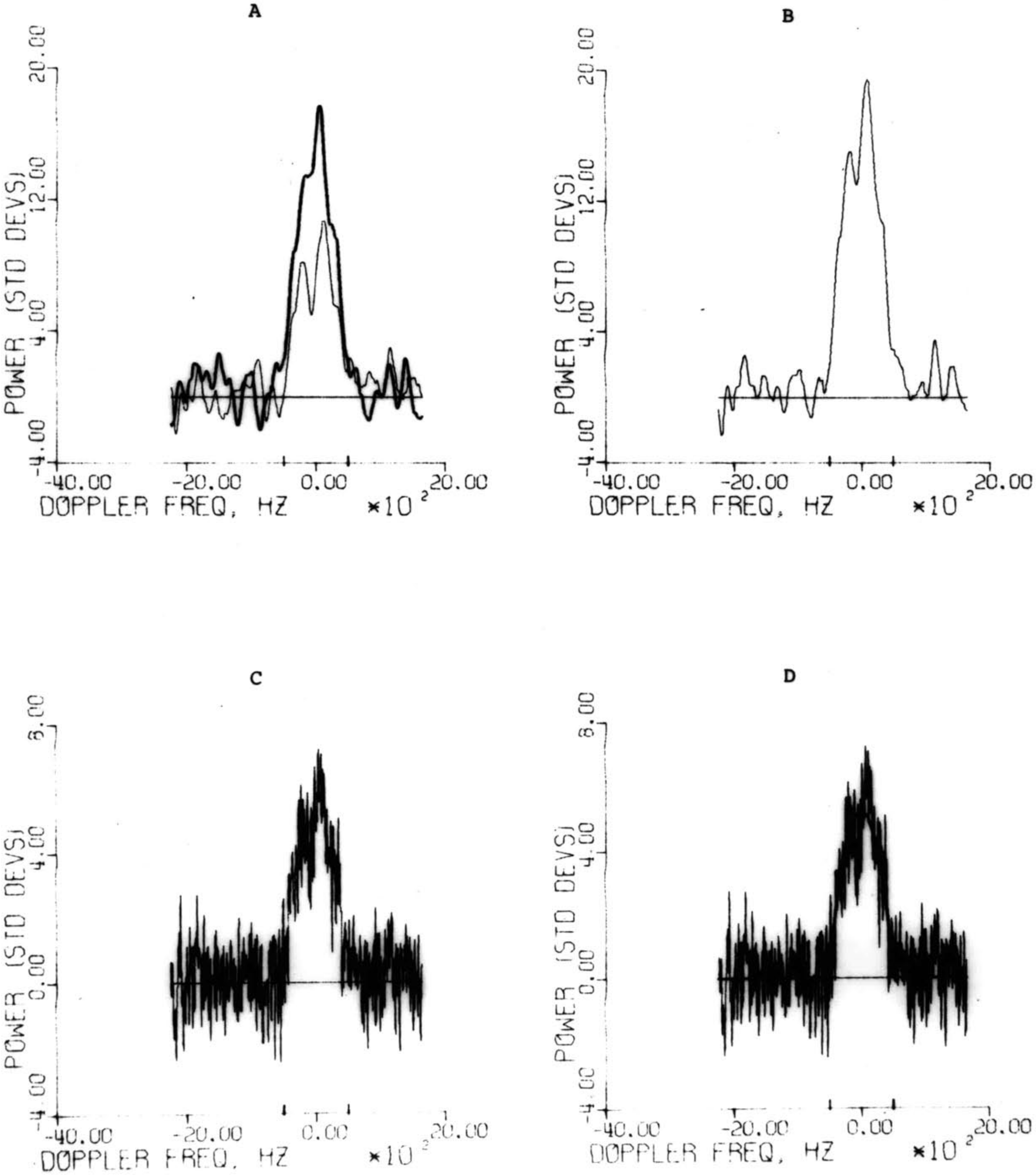

Fig. 6a

EUROPA **281°** **27 Nov 77**

$\alpha = 0.55 \pm 0.14$

$\hat{\mu}_c = 1.49 \pm 0.36$

$n_R = 1.4 \pm 0.1$

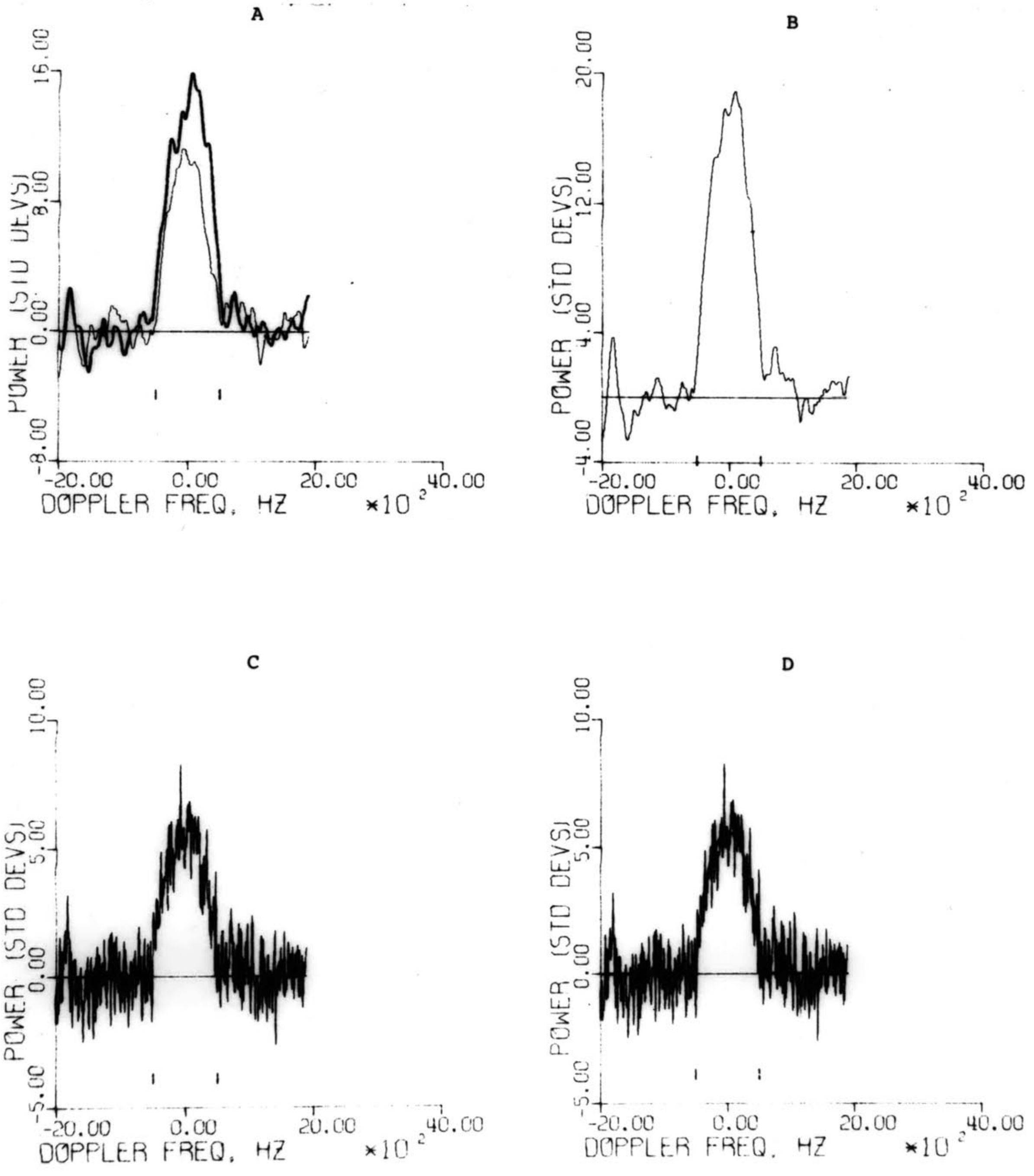

Fig. 6b

GANYMEDE 30° 25 Nov 77

α = **0.33±0.08**

μ_c = **1.42±0.77**

$\hat{n}_R$ = **1.5 ±0.3**

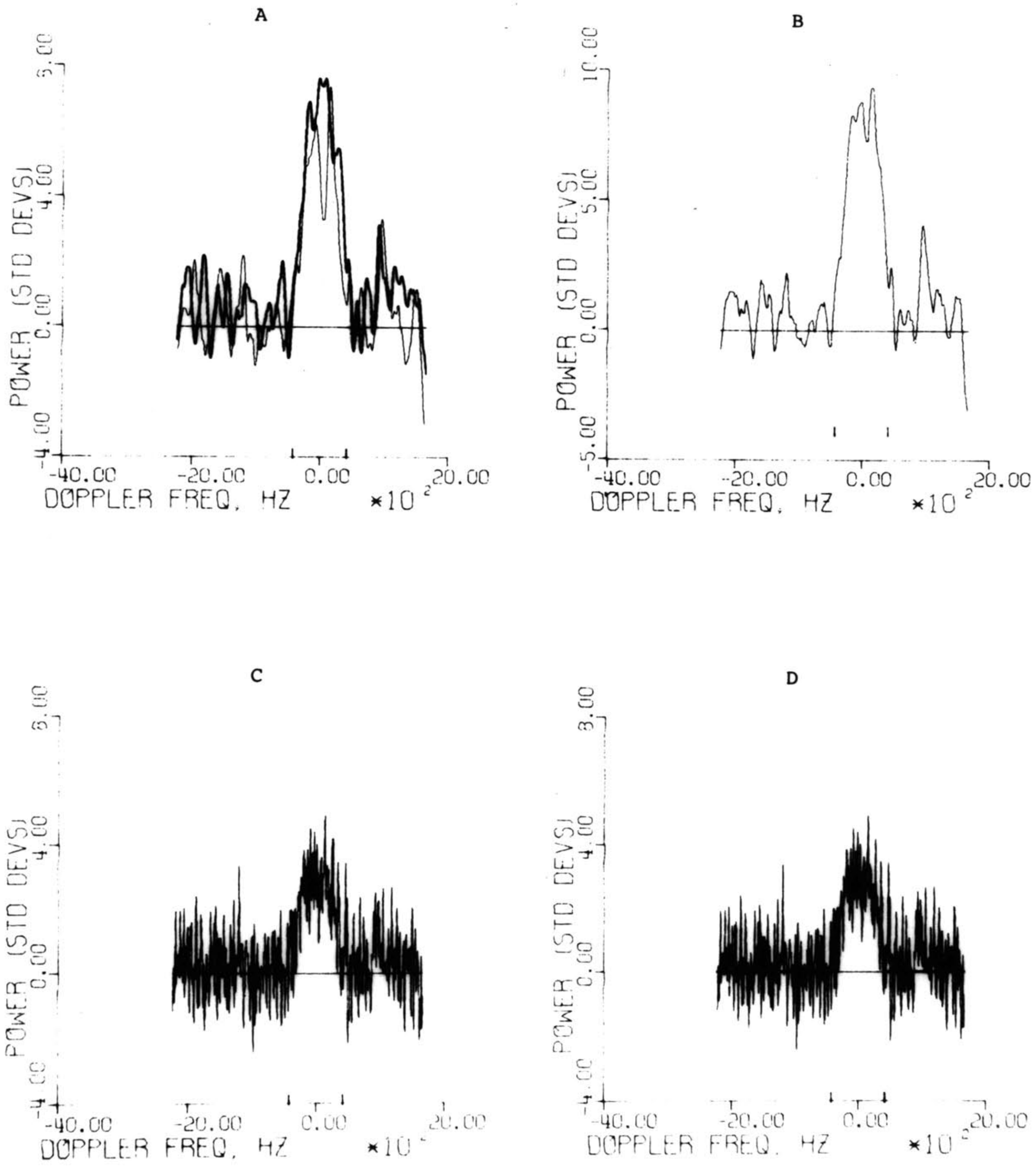

Fig. 6c

GANYMEDE **138°** **20 Nov 77**

α = **0.35±0.09**

μ_c = **1.66±0.63**

$\hat{n}_R$ = **0.9 ±0.1**

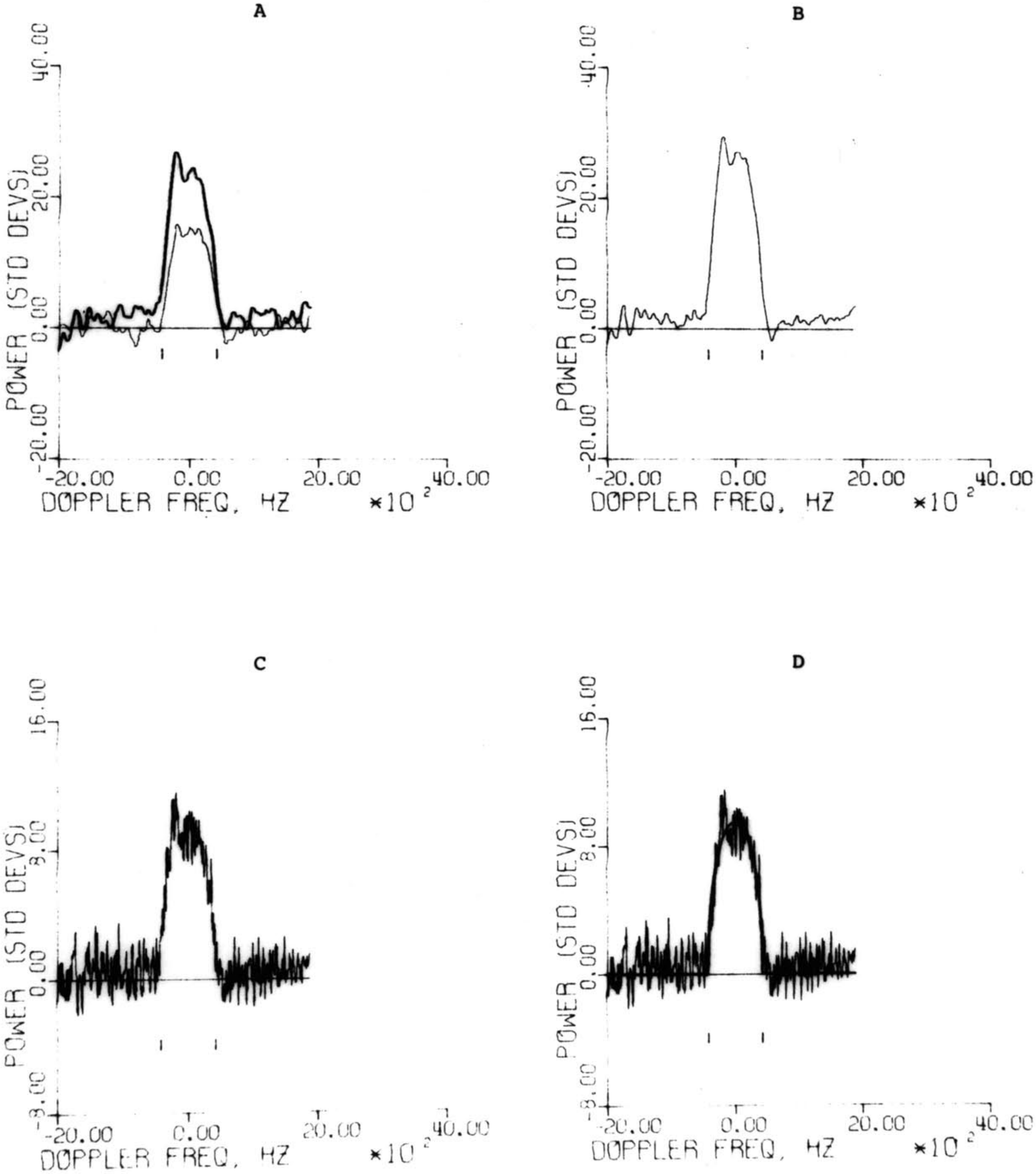

Fig. 6d

GANYMEDE 239° 22 Nov 77

α = **0.31±0.08**

μ_C = **1.48±0.32**

$\hat{n}_R$ = **1.2 ±0.1**

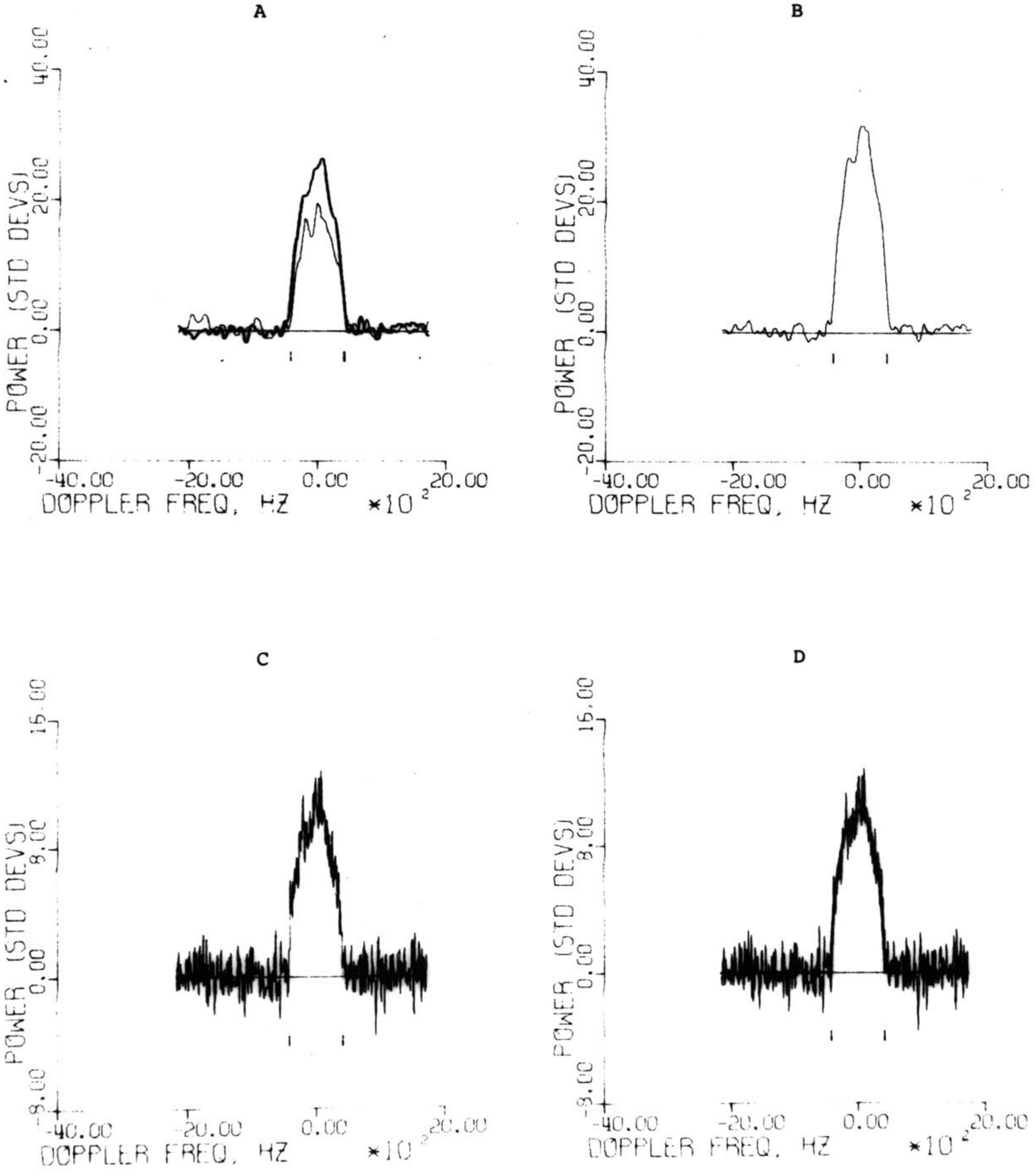

Fig. 6e

CALLISTO **12°** **21 Nov 77**

α = **0.15±0.04**

μ_c = **1.07±0.30**

$\hat{n}_R$ = **1.6 ±0.2**

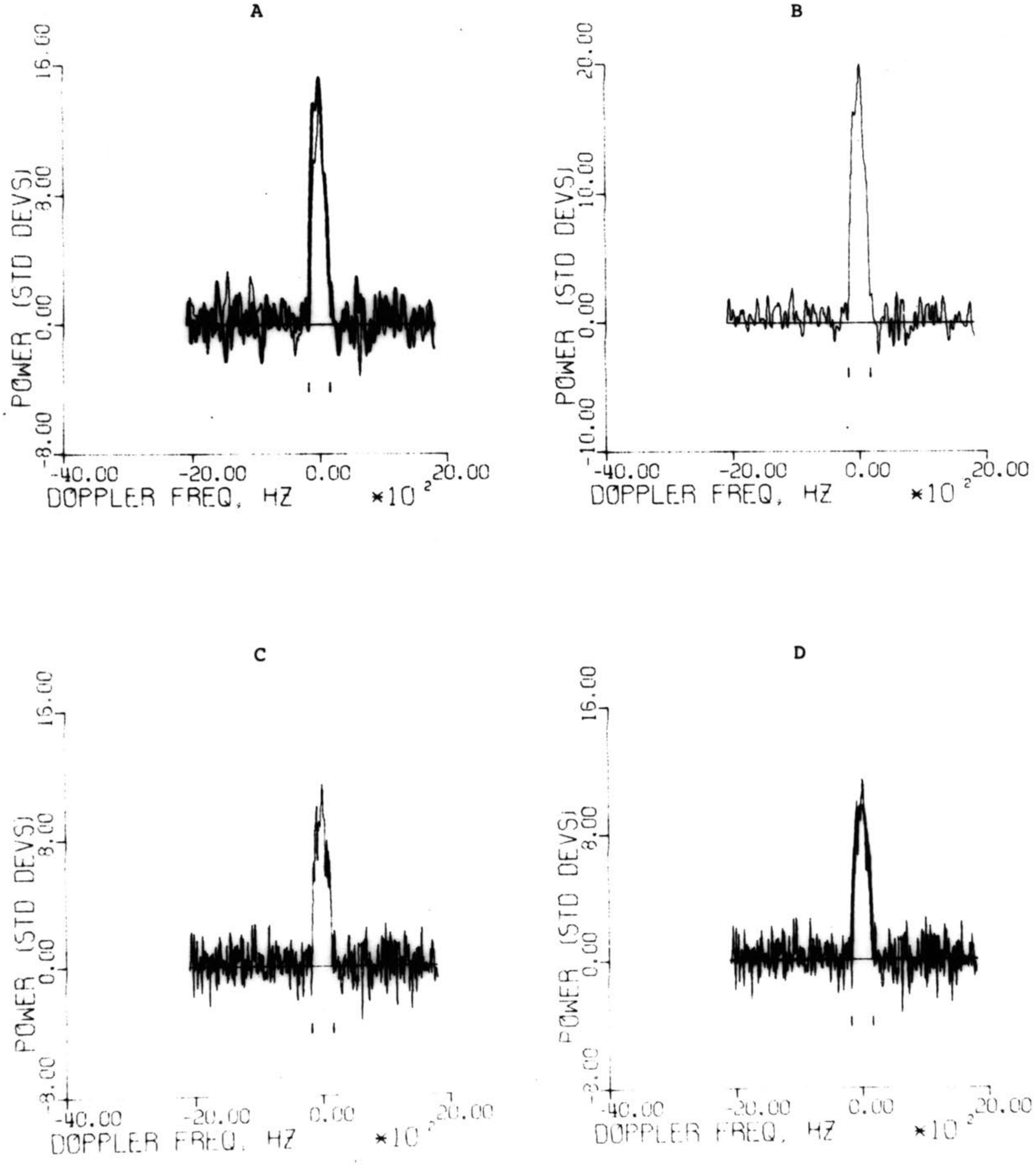

Fig. 6f

CALLISTO **120°** **26 Nov 77**

$\alpha = 0.13 \pm 0.03$

$\mu_C = 1.30 \pm 0.33$

$\hat{n}_R = 1.6 \pm 0.2$

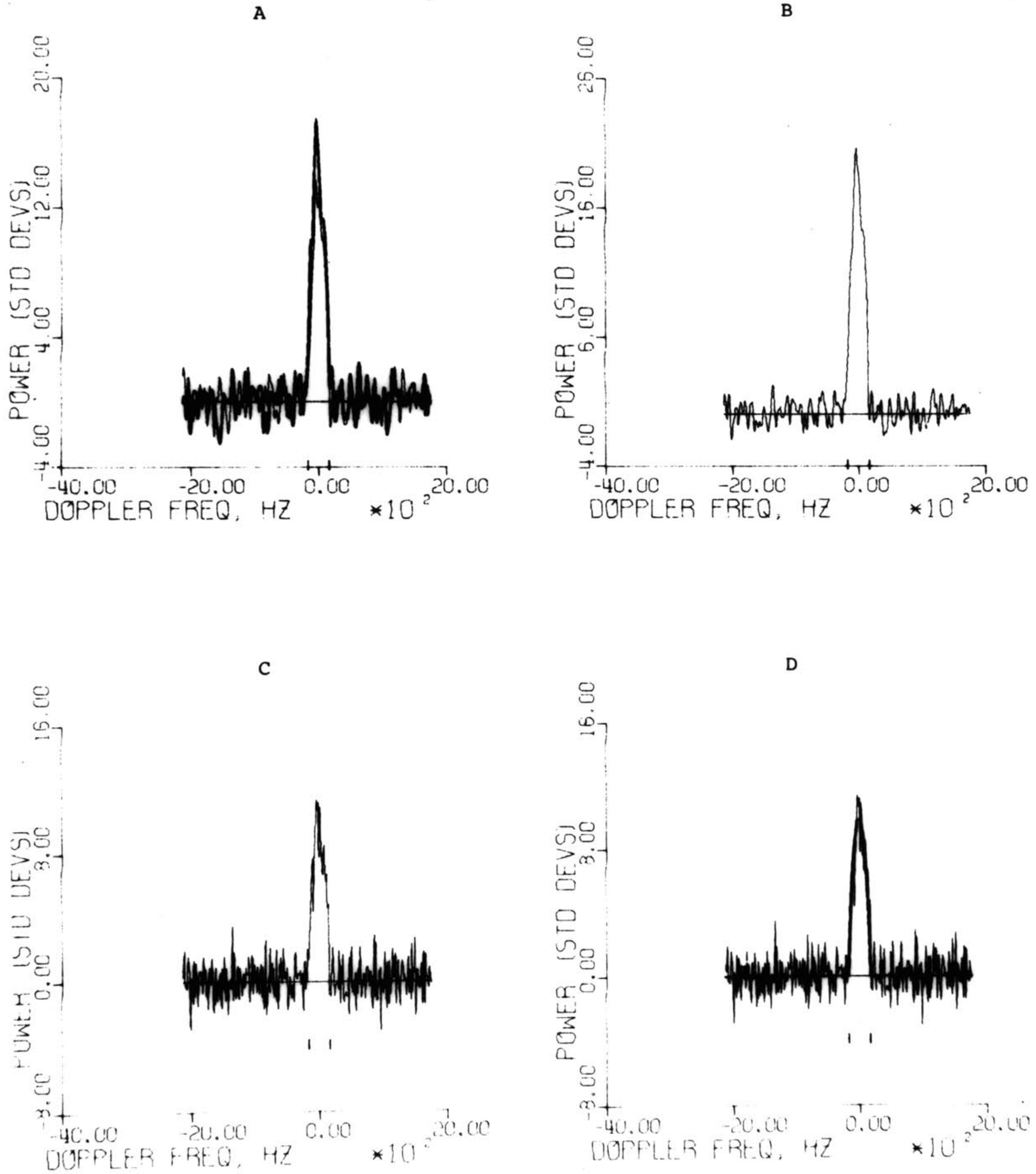

Fig. 6g

CALLISTO **243°** **15 Nov 77**

$\alpha = 0.15 \pm 0.04$

$\mu_C = 1.10 \pm 0.23$

$\hat{n}_R = 1.4 \pm 0.2$

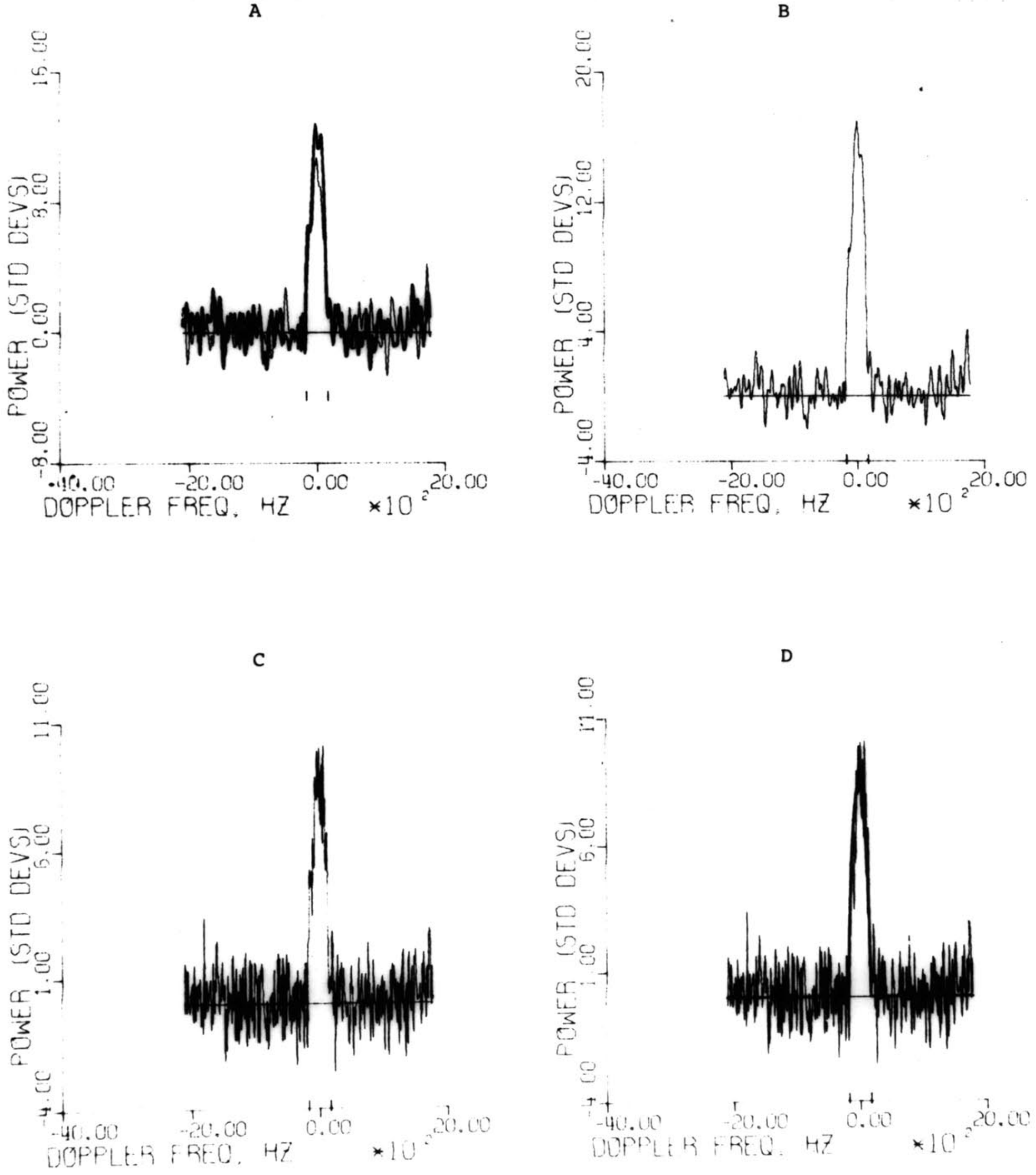

Fig. 6h

II. C. Results of observations and inferences concerning surface structure

Table VI summarizes measurements of scattering-law exponent $\underline{n}_R$, geometric albedo α, and circular polarization ratio μ_C. Weighted means of the values of these quantities determined in 1976 (Table IV) and 1977 (Table V) are listed, along with weighted means for both years.

Figure 7 is a diagram of orbital phases at which the outer three satellites have been observed from Arecibo. Phases for 1975 observations are in parentheses and phases for 1976 are daggered. Measured values of α, μ_C and the summed-polarization $\underline{n}_R$ are given, and skew toward positive or negative Dopplers is noted.

My inferences concerning surface structure derived from estimates of albedo, spectral shape, and scattering-law exponent are discussed in this section. My structural explanation of the anomalous circular polarization ratios will be developed in Section D of this chapter.

TABLE VI. Weighted-mean values of $\underline{n}_R$, μ_C and α for the 1976 and 1977 Galilean satellites observations

	1976	1977	Mean
Europa			
"OC" n_R	1.8 ±0.2	1.8 ±0.2	1.8 ±0.1
"SC" n_R	1.9 ±0.2	1.5 ±0.2	1.7 ±0.1
"TC" n_R	1.8 ±0.1	1.5 ±0.1	1.6 ±0.1
α	0.69±0.17	0.58±0.14	0.64±0.16
μ_C	1.61±0.20	1.53±0.29	1.58±0.16
Ganymede			
"OC" n_R	1.9 ±0.1	1.1 ±0.1	1.5 ±0.1
"SC" n_R	1.6 ±0.1	1.1 ±0.1	1.4 ±0.1
"TC" n_R	1.7 ±0.1	1.1 ±0.1	1.4 ±0.1
α	0.37±0.09	0.33±0.08	0.35±0.09
μ_C	1.48±0.27	1.51±0.27	1.50±0.19
Callisto			
"OC" n_R	1.5 ±0.1	1.6 ±0.1	1.6 ±0.1
"SC" n_R	1.5 ±0.1	1.5 ±0.1	1.5 ±0.1
"TC" n_R	1.6 ±0.1	1.5 ±0.1	1.6 ±0.1
α	0.15±0.04	0.14±0.04	0.14±0.04
μ_C	1.24±0.19	1.14±0.16	1.18±0.12

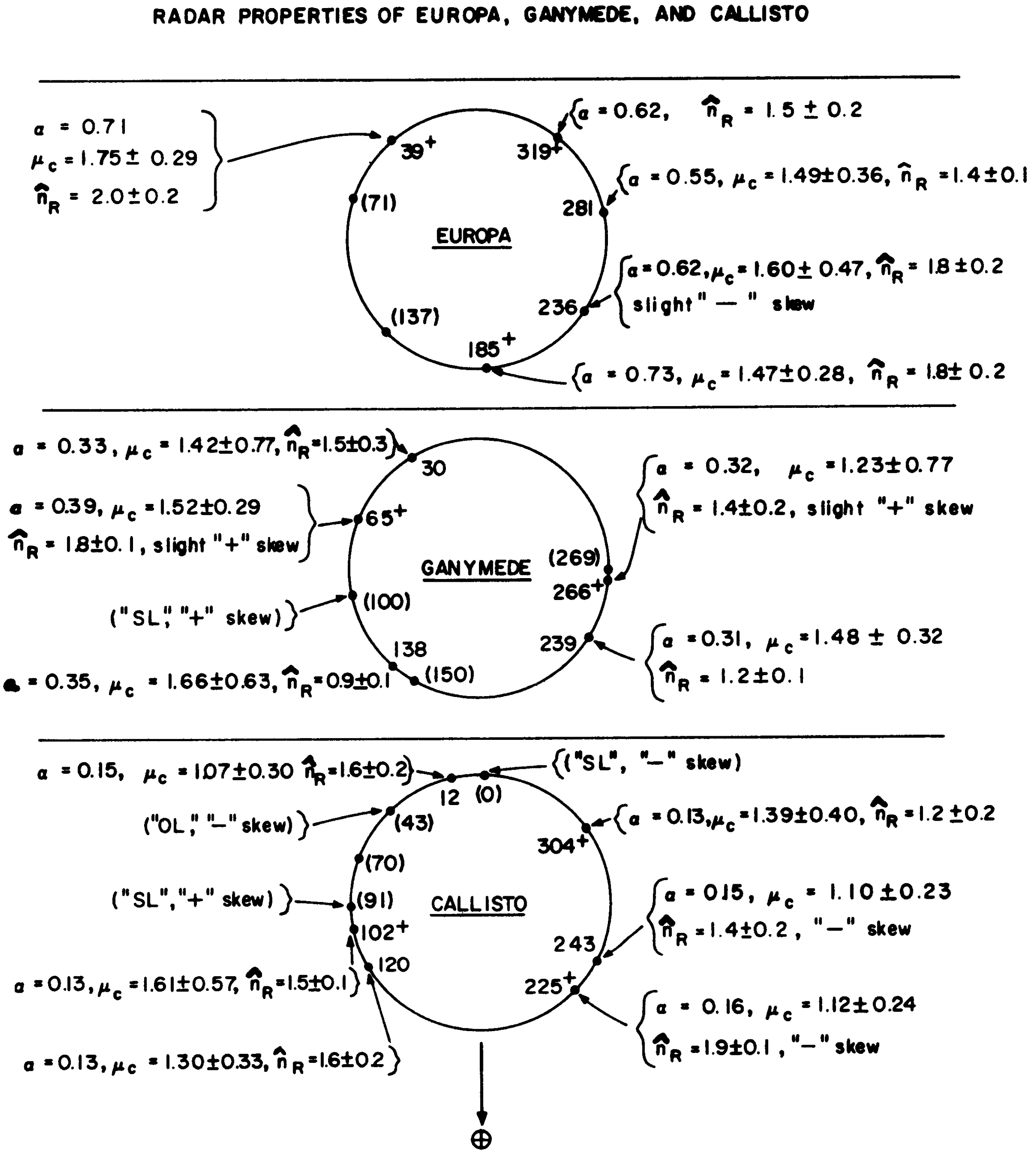

Fig. 7. Geometric albedo α, circular polarization ratio μ_C, "TC" scattering law exponent $\hat{n}_R$ and skew (if any) toward positive or negative Doppler shifts are shown at the orbital phase of observation for 1975 (Φ in parentheses), 1976 (Φ daggered) and 1977.

II. C. 1. Albedos

Albedos measured in 1977 average about 90% as large as those measured in 1976, an agreement well within suspected systematic sources of error. For example, the difference could easily be explained in terms of system temperature calibration errors alone.

However, it is difficult to resolve the discrepancy between the 1976-1977 weighted mean albedos and the earlier 1975 results. The value of $\sigma_{OC} = 0.12$ reported by Goldstein and Morris (1975) is even harder to explain without invoking time-variable 12.6-cm reflectivity. One might speculate on exotic physical phenomena which could suddenly change the effective surface electrical properties by large factors (e.g., eruptions of some aqueous electrolyte, coating vast surface areas with some very reflective material; or a process involving interaction of an icy surface with high-energy particles). My personal view is that there is no strong evidence for time-variable albedos. Since measurement of α at a given orbital phase requires simultaneous measurement of cross section in orthogonal polarizations, the inference of albedos from the 1975 data is probably much less reliable than from the 1976-1977 results.

I have listed in Table VII what I consider the best current estimates of α, μ_C and μ_L for Europa, Ganymede, and Callisto. Except for the Ganymede and Callisto linear polarization ratios, which have been inferred from CCPS, all values are weighted means of 1976-1977 results.

Figure 8 compares the radar geometric albedos in Table VII against the visible-wavelength geometric albedos *p* obtained by several observers, and values for the fraction of each satellite's surface which is covered by water frost as estimated by Pilcher *et al*. (1972). The correlation among these three quantities, first noted by CCPS, is remarkable and suggests that surface ice is chiefly responsible for the relatively high values of α.

Veverka (1977, p. 202) has tabulated, for each satellite, the longitudes Φ_{min} and Φ_{max} of minimum and maximum brightness in the V photometric system ($\lambda \approx 0.54\ \mu$) as determined by Harris (1961), Johnson (1969), Blanco and Catalano (1974 a,b), and Morrison *et al*. (1974). These two quantities provide the simplest parameterization of the satellites' lightcurves, which are nonsinusoidal in shape. Taking weighted averages of the figures in Veverka's (1977) Table 9.10, I calculate (Φ_{min}, Φ_{max}) equal to (282°, 83°), (261°, 61°), and (114°, 269°) for Europa, Ganymede, and Callisto, respectively. These longitudes are denoted by arrows (↓, ↑) in Fig. 9, where measured satellite geometric albedos are plotted as functions of subradar longitude Φ. Weighted mean albedos from Table VII are indicated by horizontal lines in the figure.

Figure 9 suggests that the orbital-phase dependence of radar geometric albedo may mimic the fundamental trends in *p*(Φ) indicated by Φ_{min} and Φ_{max}. In light of the sparseness

TABLE VII. Galilean satellites: best current estimates of polarization ratios and geometric albedos. Values correspond to the weighted mean of results for different phases in 1976 and 1977, except that entries marked with an asterisk are inferred from several single-polarization measurements made in 1975 by CCPS.

Target	μ_C	μ_L	$\alpha,$
Europa	1.58±0.16	0.48±0.08	0.64±0.16
Ganymede	1.50±0.19	*0.62±0.22	0.35±0.09
Callisto	1.18±0.12	*0.41±0.14	0.14±0.04

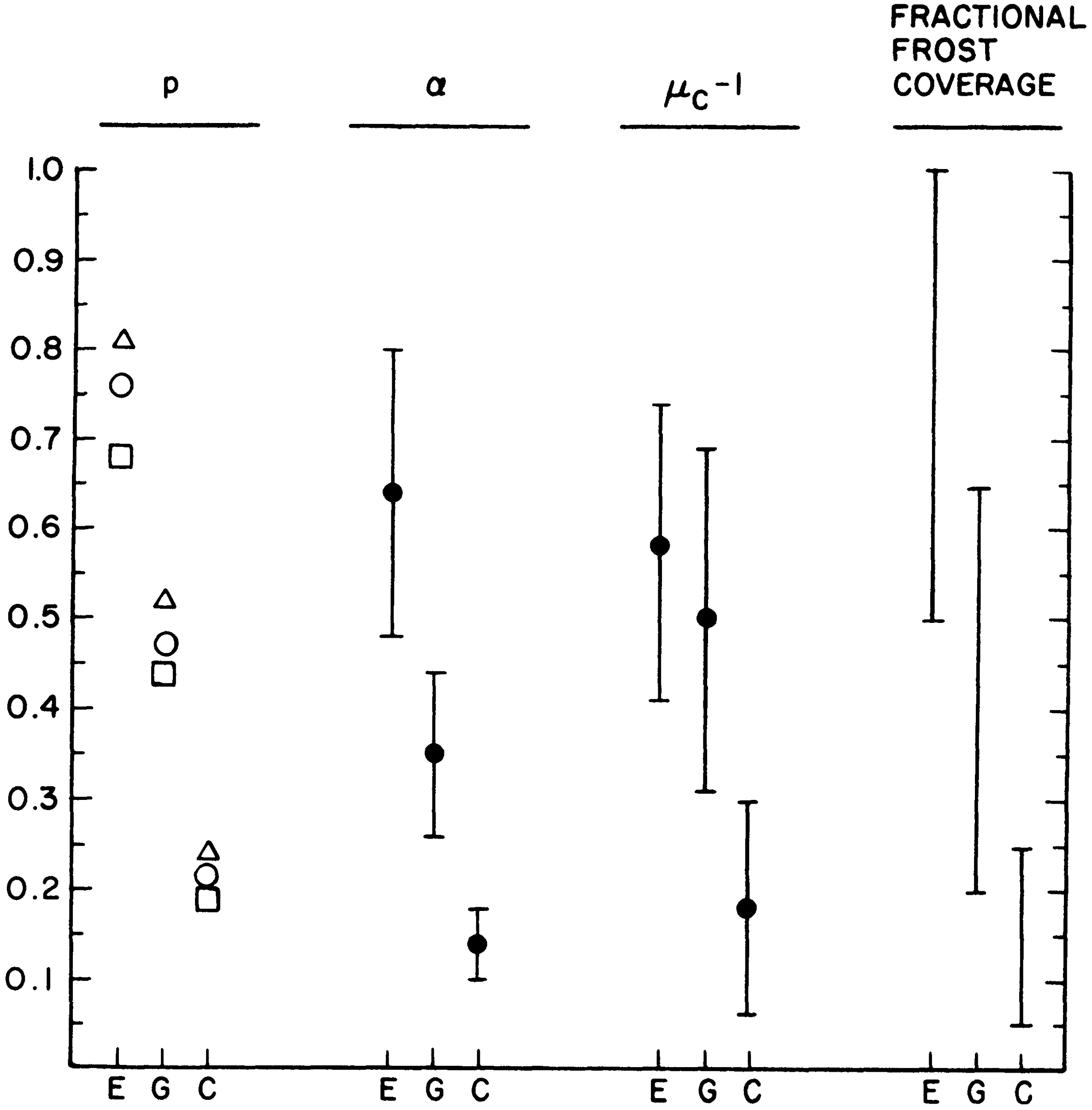

Fig. 8. The radar geometric albedo α, optical geometric albedo p and radar polarization ratio μ_C are shown for Europa (E), Ganymede (G) and Callisto (C), in an attempt to highlight an apparent correlation between them and surface ice. The circles, triangles and squares correspond to values of p determined by Harris (1961), Johnson (1971) and Morrison et al. (1974), respectively. Estimates of fractional frost coverage are by Pilcher et al. (1972).

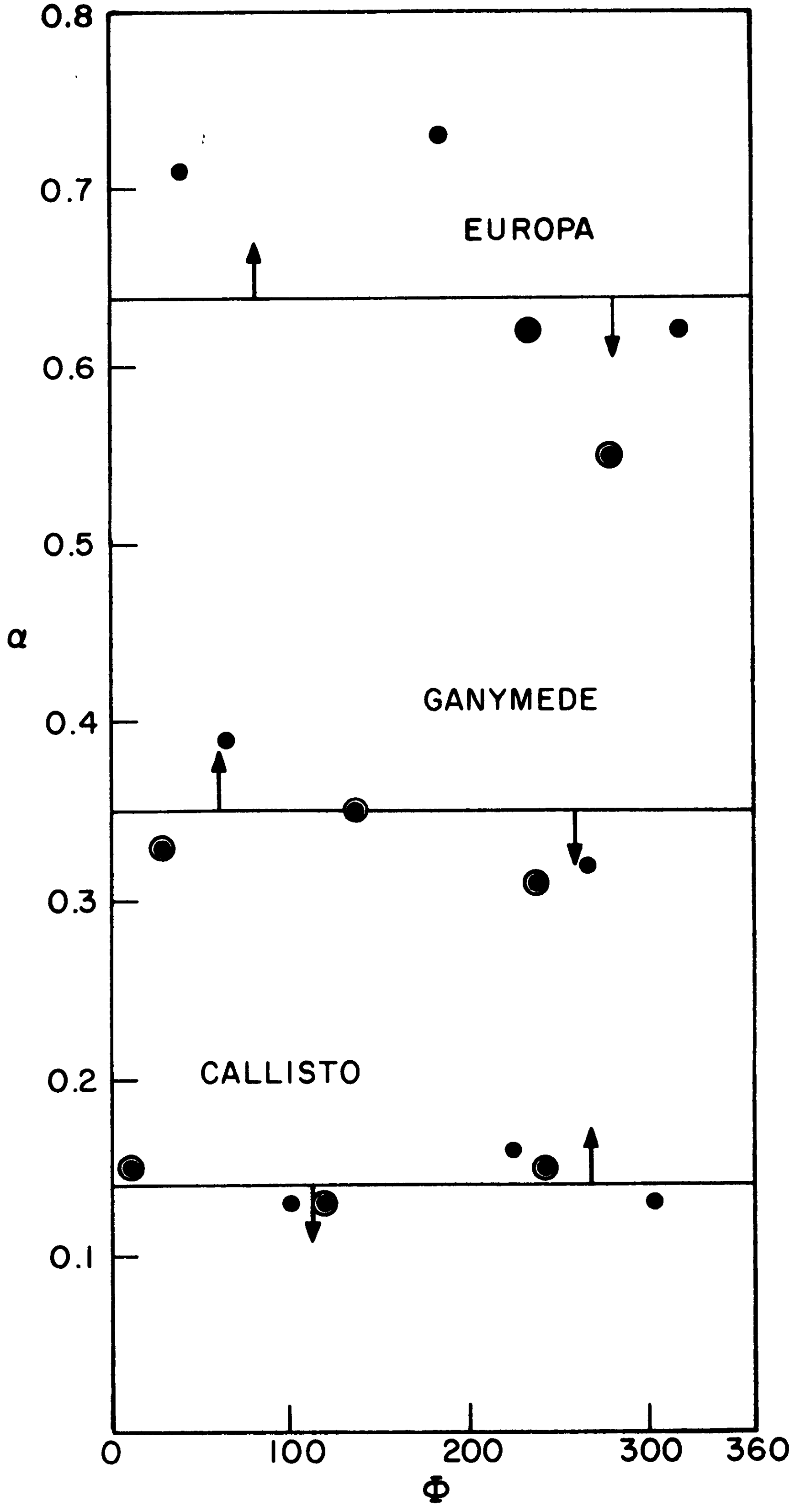

Fig. 9. Galilean satellites' α(Φ) measured in 1976 (dots) and 1977 (circled dots). Horizontal lines are drawn at values of α given in Table VII. Arrows designate longitudes of visible-wavelength brightness minima and maxima (see text).

of data, the estimated 25% uncertainty in α, and the possibility of 1976-to-1977 calibration problems, this conclusion is very tentative. If significant, correlation between $\alpha(\Phi)$ and $\underline{p}(\Phi)$ would constitute additional evidence that surface ice is responsible for the unique radar behavior of Europa, Ganymede, and Callisto. It could also mean that the surface layers responsible for visible-wavelength lightcurves are many radar wavelengths thick.

II. C. 2. Spectral shape and scattering law

As a whole, the spectra in Figs. 5 and 6 are fairly symmetrical, although a few (see Fig. 7) are slightly skewed toward positive or negative Dopplers. Some (e.g., Europa at $\Phi = 236^{\circ}$ and Ganymede at $\Phi = 138^{\circ}$) show small irregularities which may be evidence of surface features. Two spectra, taken at orbital phases about 180° apart, and skewed in opposite directions, might be evidence for surface albedo differences a full hemisphere in size. If such spectra did not "invert" in this manner, i.e., if both were skewed in the same Doppler sense, the sources of scattering enhancement could not be a full hemisphere in extent. However, a very large part of the surface, perhaps a "quarter-sphere" in scale, would certainly have to be relatively brighter (or darker) to account for the spectral skew.

A better description of surface properties cannot be drawn on the basis of spectral asymmetry alone because of (a) the low surface resolution afforded by Doppler strips that are $\sim 0.1\ \underline{f}_{LL}$ wide, and (b) the inability to distinguish composition-related reflectivity variations from structure-related enhancements in backscatter gain.

The differences between the two estimates of $\underline{n}_R$ obtained separately in two orthogonal senses of polarization are insignificant in most cases. An exception occurs when observing Europa at $\phi = 281^{\circ}$, where I find $\underline{n}_R$ equals 1.9 ± 0.3 and 1.2 ± 0.2 for "OC" and "SC" polarization senses, respectively. The latter value is close to the scattering-law exponent corresponding to a uniformly bright disc and may reflect the absence of ice in subradar regions. This possibility is suggested by the relatively low albedo found at this orbital phase, a fact which could also explain the skewness of the spectrum obtained at $\Phi = 236^{\circ}$.

Since estimates of $\underline{n}_R$ in orthogonal polarizations are, in most cases, similar, the summed-polarization scattering law exponent $\hat{\underline{n}}_R$, estimated from "TC" or "TL" spectra, would seem to be an appropriate descriptor of average scattering behavior. Most measured values of $\hat{\underline{n}}_R$ lie in the range $1 \leqslant \hat{\underline{n}}_R \leqslant 2$. In other words, the satellites generally exhibit at least a small amount of limb darkening $(\hat{\underline{n}} > 1)$. As shown in Table VI, the weighted mean value of $\hat{\underline{n}}_R$ for all three outer satellites is 1.5 ± 0.2. Thus the <u>average</u> angular dependence of scattering from these Galilean satellites is quite similar to that for the <u>diffuse</u> portion of the lunar and Venus echoes (Hagfors, 1968; Hagfors and Campbell, 1974).

From the data in hand, μ_C and $\underline{n}_R$ do not appear to be correlated with the orbital phase of the corresponding observations. However, the dispersion among measurements of $\underline{n}_R$ is less for Europa than it is for Ganymede or Callisto.

The summed-polarization estimates of $\underline{n}_R$ for Ganymede are very scattered. As noted in Fig. 7, several Ganymede spectra are slightly asymmetric. Those at $\Phi = 65^{\circ}$, 100°, and 266° are each somewhat skewed in the same directions, suggesting that the sources of these asymmetries are less than hemispherical in size.

Callisto spectra at $\Phi = 91^{\circ}$ and 243° are skewed in opposite directions. This might be evidence that the space-facing hemisphere of Callisto is more reflective than the Jovian side, in conflict with the orbital-phase dependence of albedo suggested by Fig. 9. The rapid change in $\hat{\underline{n}}_R$ from 1.9 ± 0.1 to 1.4 ± 0.2 between $\Phi = 225^{\circ}$ and $\Phi = 243^{\circ}$, taken together with the fact that spectra at these orbital positions are similarly skewed, supports the hypothesis that there are surface inhomogeneities on Callisto as well as on Ganymede which are less than hemispherical in scale.

II. C. 3. Polarization ratios

The 1975 results revealed that Europa, Ganymede and Callisto scatter substantial amounts of linearly polarized incident radiation into both orthogonal receiving polarization planes. A major objective behind the design of the 1976 and 1977 observations was an accurate determination of the ratio of cross sections as measured by two orthogonally polarized receiving systems, using both linearly and circularly polarized transmissions. The good agreement between the single measurement of μ_L (for Europa at $\Phi = 319^{\circ}$) in 1976, and the corresponding value obtained in 1975 by CCPS from determinations of σ_{SL} and σ_{OL} on separate nights, lends some confidence to the ratios given in Table I.

The weighted means of μ_C obtained separately for Europa, Ganymede and Callisto as shown in Table VI and Fig. 7 are extraordinarily high. These satellites are the only radar astronomical targets so far found to have $\mu_C > 1$. The correlation between μ_C and fractional ice coverage of the surface for each of the outer three satellites, as shown in Fig. 8, serves to increase further the suspicion that ice must somehow be responsible, not only for their high geometric albedos, but also for their unusual polarization properties.

The striking differences between the circular polarization properties of the outer three Galilean satellites and those of the terrestrial planets is demonstrated by comparison of the spectra in Fig. 5 and Fig. 6 with the Venus spectra (after Carpenter, 1966) in Fig. 4a. As limits to μ_C for "normal" surfaces, note that an echo from a plane mirror would yield $\mu_C = 0$; _no_ power would be backscattered in the same circular sense as was transmitted. A surface covered with randomly oriented dipoles would yield $\mu_C = 1$, as would any high-order internal or external multiple-scattering process.

Under certain conditions "double-bounce backscatter", involving two reflections from plane boundaries with perpendicular normals, can cause μ_C to exceed unity (Beckmann, 1968, p. 162). However, double-reflection backscatter would not be expected to dominate the total scattering unless there were severe constraints on surface geometry. Indeed, the structural configuration of a surface, presumably composed of water ice and some silicate rock, which can return echoes having $\mu_C > 1$ is not immediately obvious.

II. D. Circular polarization ratios greater than unity: The icy-crater theory

This section is devoted to development of the theory (Ostro and Pettengill, 1978) that the anomalous values of μ_C observed for Europa, Ganymede, and Callisto are due to double-reflection backscatter from nearly hemispherical craters. The original material by Ostro and Pettengill has been slightly revised, here, to include the results of observations and some calculations that were performed while that article was in press.

II. D. 1. The icy-crater theory: Introduction

Europa, Ganymede and Callisto are bright, diffusely scattering objects with unexpected polarization properties. As discussed by CCPS, the high degree of echo depolarization observed for linearly polarized incident waves is consistent with a rough, icy surface. However, the 1976-1977 measurements, which used circularly polarized waves, suggest that the types of surface irregularities found on the Galilean satellites must be very different from those on the inner planets. This chapter examines the nature of these irregularities.

Evans and Hagfors (1966) found values of (μ_L, μ_C) equal to (0.03, 0.09)* for echoes received from the <u>entire</u> surface of the Moon at 23-cm wavelength; for the diffuse component of the lunar echo, they obtained (0.14, 0.50). In contrast, ratios measured for the outer three Galilean satellites average (0.5, 1.4). Table VII shows for each satellite the weighted-mean polarization ratios and geometric albedo.

As already pointed out, these bodies are the first extraterrestrial radar targets for which μ_C has been found to exceed unity. The circular polarization ratio, both optical and radar geometric albedo, and water-ice coverage of the surface (as inferred from spectroscopic data) increase in the order: Callisto, Ganymede, Europa. While the albedos

---

*These values were not directly quoted in the reference but have been inferred from data given there.

and the amounts by which μ_C exceeds unity appear correlated with the presence of ice, the detailed reflecting mechanism which gives rise to the observed behavior is hardly obvious. In the next part of this section, I use geometrical optics and the Stokes-vector formalism to examine several possible configurations which could cause μ_C to exceed unity. In the final part of this section, I present a simple theoretical model of a surface which is both physically plausible and capable of satisfying the observations.

II. D. 2. How can the circular polarization ratio exceed unity?

As we have seen, for Europa, Ganymede and Callisto, the radar scattering must be dominated by some "mystery process" which returns more power in the transmitted sense of circular polarization than in the sense orthogonal to it. All single-reflection backscattering reverses the rotational sense of incident circular waves, so the mystery process must involve at least two reflections. Furthermore, the fact that the degree of polarization (Appendix G) of the observed echoes has a value at least as high as 20% means that the mystery reflection process must be at least partially phase coherent. In other words, the reflections of interest probably arise from surfaces which are large and quite flat at a scale of 12.6 cm, thus justifying the use of a modified form of geometrical optics.

Further restrictions on the mystery process follow from the behavior of the Fresnel amplitude reflection coefficients $r_{\perp}$ and $r_{\parallel}$ (Appendix G) for components of the electric field perpendicular and parallel, respectively, to the plane of incidence. Because the ratio $r_{\parallel}/r_{\perp}$ changes sign when the angle of incidence θ passes through Brewster's angle θ_B, the rotational sense of the reflected component of a circularly polarized incident wave, which reverses for $\theta < \theta_B$, is preserved for $\theta > \theta_B$. For $\theta = \theta_B$, the reflected waves become linearly polarized ($\mu_C = 1$); thus the mystery process must not involve reflections having $\theta \approx \theta_B$. [For water ice, I use a refractive index of 1.78 (Hobbs, 1974, p. 89) yielding: $\theta_B \cong 61°$; a typical index for silicates is 2.4 (Table I of Campbell and Ulrichs, 1969) giving: $\theta_B \cong 67°$.] The mystery process may involve an even number of reflections at angles substantially less than θ_B combined with any number of reflections at angles considerably greater than θ_B, i.e., at grazing angles of incidence. However, multiple reflections at grazing angles are unlikely to be the primary source of backscattered power. (Cube-corner reflectors, which generally cause three reflections at an average angle of about 55°, are thus ruled out.)

A large number of dielectric reflections at random angles of incidence would tend to depolarize the incident wave. Although high-order multiple scattering probably is responsible for part of the total backscattered intensity, it certainly cannot be of significant importance in the mystery process *per se*.

We are thus led to consider in more detail the properties of a backscattering event consisting of a pair of successive reflections, from two dielectric surfaces, at local incidence angles θ_1 and θ_2. Figure 10 shows the polarization ratios as a function of θ_1 for "double-bounce" backscatter ($\theta_1 + \theta_2 = 90°$) from water-ice facets averaged over all azimuths (Appendix G). The curves for μ_L and μ_C reach their maxima when $\theta_1 = \theta_2 = 45°$. However, the backscattered intensity will be proportional to the product $\underline{W}$ of

Fig. 10. Polarization ratios μ_C and μ_L for double-bounce backscatter from pure water ice facets ($\underline{m} = 1.78$) as functions of angle of incidence θ_1; for angles of incidence greater than 45° , use the complement. Note that $\mu_C = 1$ and $\mu_L = 1/3$ at the complement ($\approx 29°$) of the Brewster angle θ_B. The curve marked "W" is proportional to the product of the Fresnel intensity coefficients for angles of incidence θ_1 and $\theta_2 = 90° - \theta_1$ and is discussed in the text.

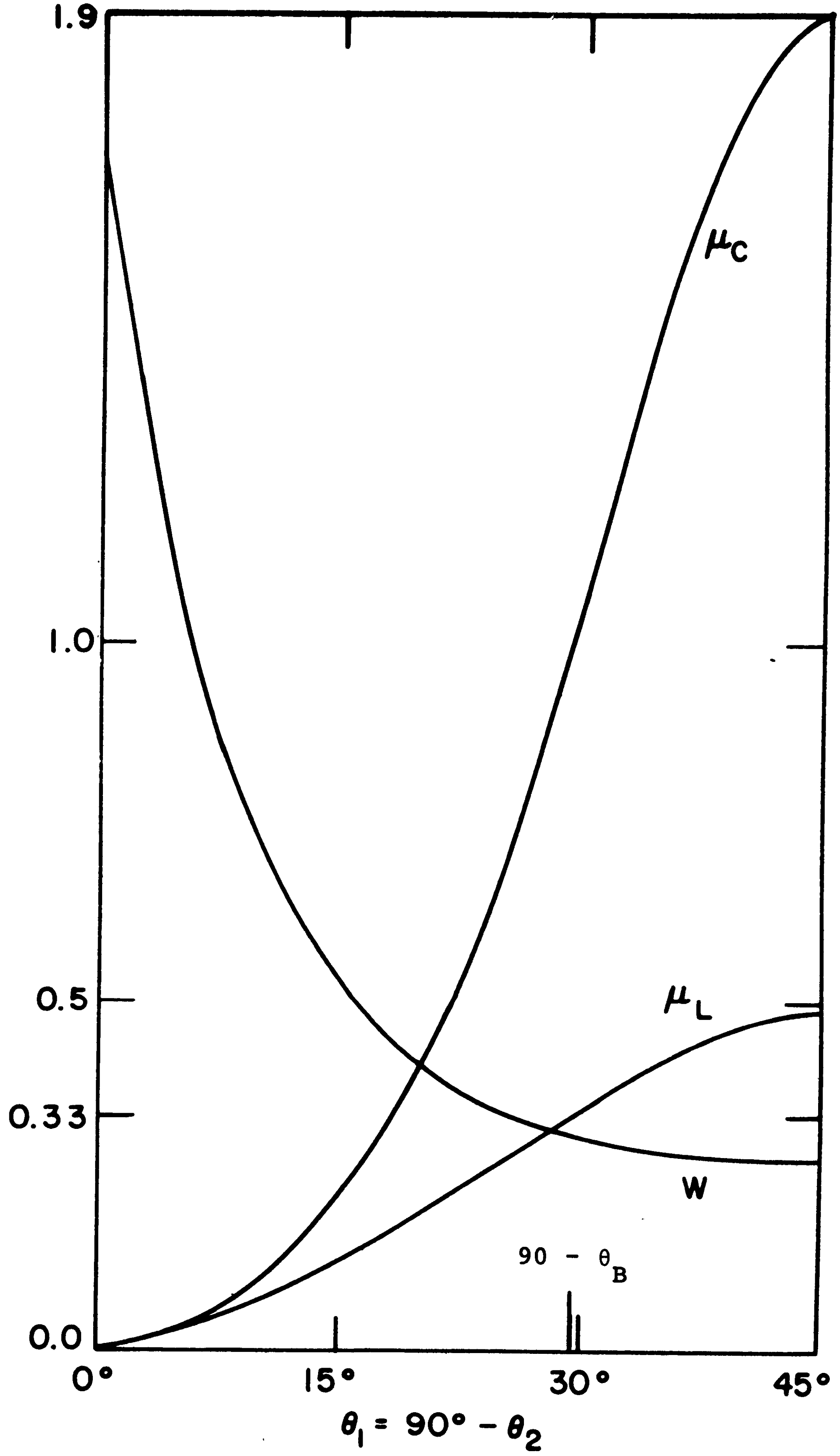
1.9
1.0
0.5
0.33
0.0
0°
15°
30°
45°
$\theta_1 = 90° - \theta_2$
μ_C
μ_L
W
90 - θ_B

the Fresnel intensity reflection coefficients for θ_1 and θ_2; as shown in Fig. 10, W is a minimum at 45°. Of course, the observed backscattered intensity depends upon the facet size, population density and orientation, as well as upon W. The accurate calculation of μ_C for an ensemble of ice facets requires specific assumptions concerning these factors. Nevertheless, I find that double-bounce backscatter from a distribution of randomly oriented large ice facets lacking substantial geometric correlation with their neighbors cannot yield $\mu_C > 1$. Therefore, the mystery process must involve some geometric constraint on surface structure which weights the echo contribution from "45°-double-bounce backscatter" well above that from a single reflection at normal incidence. As the refractive index increases, the maximum value of μ_C and the range of angles over which $\mu_C > 1$ also increase, thus reducing the degree to which this constraint is required. Nevertheless, for any reasonable refractive index the average value of μ_C will exceed unity only if $\theta_1 \approx 45°$ is favored.

I have also considered scattering from discontinuities within a thick layer of ice whose surface is, in some fashion, impedance matched to free space. Randomly oriented silicate rocks with flat surfaces large compared to the observing wavelength, and distributed through the ice like raisins in pudding, can be treated in the same manner as ice facets, above, giving rise to a similar constraint on the value of μ_C. The ratio of the refractive index of the "raisins" relative to the surrounding ice is about 1.35, however, so the behavior for $\mu_C(\theta_1)$ is modified from that shown in Fig. 10 such that μ_C does not reach unity until $\theta_1 = 37°$ and peaks at a value of only 1.25. Thus, an ensemble of randomly oriented subsurface rock facets leads to an even less likely candidate model for the mystery process. My calculations indicate that hollow discontinuities within a layer of ice work no better.

II. D. 3. Scattering from hemispherical craters

In this section, I discuss the results to be expected for radar scattering from an icy surface which is saturated with nearly hemispherical, but not substantially overlapping, craters. The craters are assumed to have interior curvature approximated by facets which are large and flat at the scale of the wavelength (12.6 cm). Thus, geometrical optics may be assumed to hold for this model. The likelihood of finding such surfaces in "real life" is discussed later.

Picture a hemispherical crater located at the subradar point, so the angle $\underline{I}$ between the radar line of sight and the normal to the plane containing the crater rim is zero. Single-reflection echoes will be seen from the bottom of the crater while double-reflection echoes will be returned from a zonal region of the crater wall inclined 45° to the bottom. Double reflections involving angles of incidence very different from 45° are precluded by the spherical geometry. The relative intensity of triple-bounce and higher-order echoes will be small compared to the single- and double-bounce echoes, because the projected areas of the facets decrease as the angles of incidence increase, and because substantial losses of power occur in the successive reflections where each Fresnel intensity coefficient is much less than unity. Since these third- and higher-order multiple reflections are largely depolarized ($\mu_C \approx 1$), they are neglected at this stage.

Single reflections from a facet near the crater bottom normally yield stronger echoes than result from a pair of facets suitably located and oriented for double-reflection backscatter. On the other hand, there are many more such double-reflection pairs than suitably oriented single-reflection facets. Thus, one must do a careful calculation to see which process wins out. In other words, the net scattering matrix (Appendix G) and, therefore, μ_C depend on the refractive index, the facet size, and the distribution of facet normals relative to the local mean spherical radius vector. Since the craters are hemispherical in shape, the geometry of double-bounce backscatter is independent of the crater location on the satellite surface until $\underline{I}$ approaches 45°. At this point, the elliptical projection of the circular rim intercepts the interior annular locus for double-bounce backscatter and μ_C begins to decrease (Appendices H and J).

This model has been investigated quantitatively using the Stokes formalism (Appendix G). At an incidence angle $\underline{I}$ to a given crater, the scattering matrix which results from each configuration of facets producing single- or double-bounce echoes is calculated, weighted by its probability of occurrence, and summed. Armed with this result (the crater scattering matrix $\underset{\sim}{B}$), I calculate the whole-target scattering matrix $\underset{\sim}{C}$ by integrating over the visible hemisphere. The free parameters in the resulting model are refractive index $\underline{m}$, mean facet dimension F (or F_λ measured in wavelengths), crater radius R (or R_λ in wavelengths), and the cutoff angle

ε_c for the angular-distribution probability $P(\varepsilon)$ of facet normals. Here ε is the deviation of a facet normal from the normal to the mean spherical surface. For simplicity, $P(\varepsilon) = P_o(1 - \varepsilon^2/\varepsilon_c^2)$ is chosen, where P_o is a constant of normalization and $P(\varepsilon) \equiv 0$ for $\varepsilon > \varepsilon_c$. Details of the model calculations are given Appendix H.

Figure 11 shows polarization ratios and geometric albedos calculated <u>versus</u> refractive index for several facet sizes. Weighted means of these quantities as listed in Table VII for Europa, Ganymede, and Callisto are also indicated in the figure.

The results appear to be strongly dependent both on the facet size and index of refraction. As illustrated for the case: $F_\lambda = 30$, the geometric albedo α is apparently more sensitive than μ_C to a change in ε_c: Increasing ε_c from 1° to 3° reduces μ_C by less than 10% but cuts α nearly in half. The corresponding variations are less marked for μ_L, which has values generally falling in the range $0.3 < \mu_L < 0.7$, in fine agreement with observation. Although the results are independent of crater size, minimum diameters on the order of one kilometer ($R_\lambda \approx 4000$) are implicitly demanded by my choices of F_λ and ε_c because strict interpretation of F_λ as the mean dimension of actual facets requires $R_\lambda \gtrsim F_\lambda/(2\varepsilon_c)$.

If the craters are assumed to be smoothly curved rather than faceted, with R_λ as an effective (minimum) radius of curvature, then F_λ might be interpreted as the characteristic (maximum) dimension of a coherently reflecting surface

Fig. 11. Calculated polarization ratios μ_C and μ_L, and geometric albedo α as functions of refractive index for several facet sizes F_λ (in wavelengths). Solid curves correspond to $\varepsilon_c = 1$. The weighted means of values for μ_C, μ_L and α obtained in 1976 and 1977 (Table VII) are given at the right side of the figure for Europa (E), Ganymede (G) and Callisto (C).

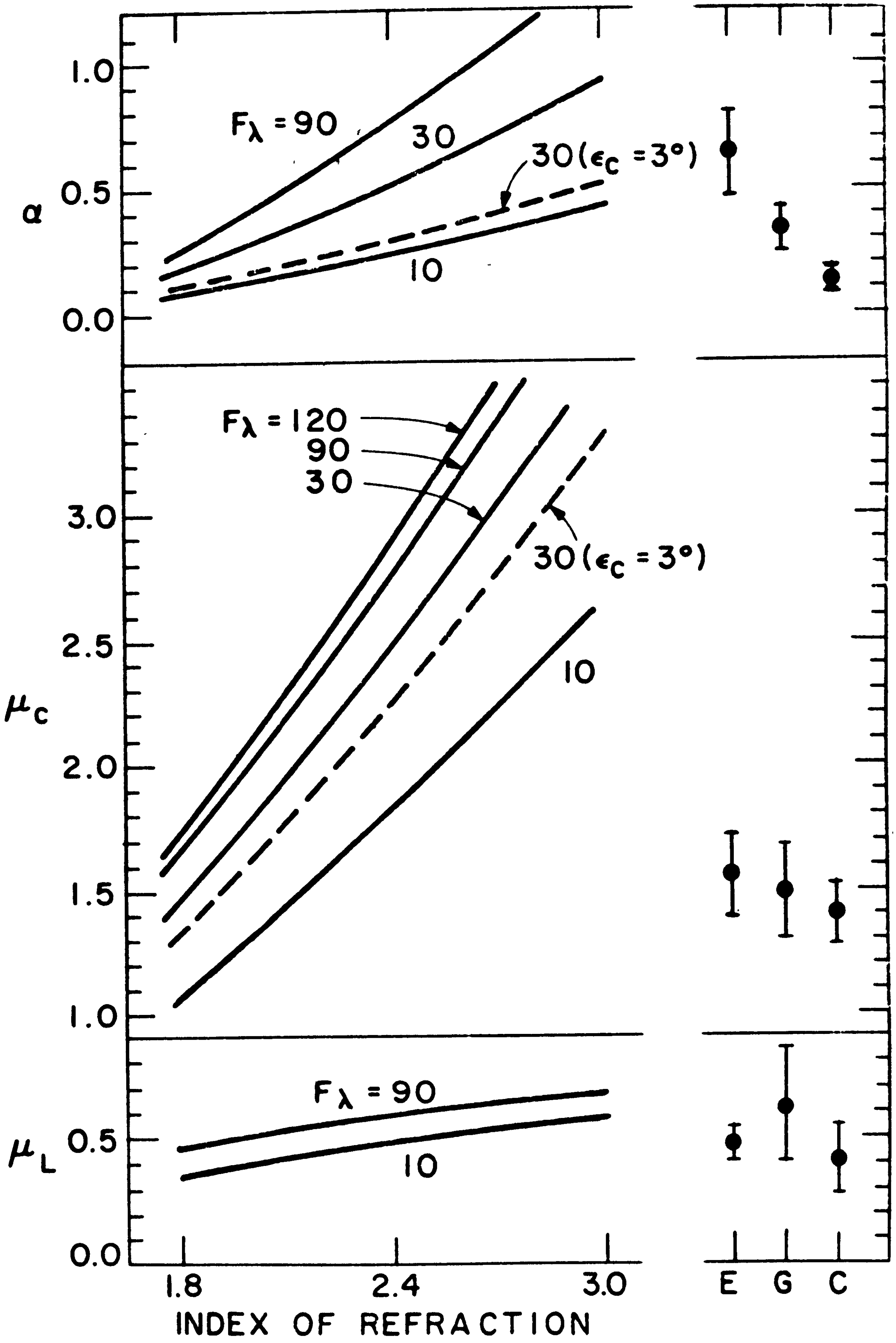
1.0
0.5
0.0
α
Fλ = 90
30
30(εc = 3°)
10
3.0
2.5
2.0
1.5
1.0
μc
Fλ = 120
90
30
30(εc = 3°)
10
μL
0.5
0.0
Fλ = 90
10
1.8
2.4
3.0
INDEX OF REFRACTION
E
G
C

element (i.e., a Fresnel zone). This would imply $R_\lambda \gtrsim F_\lambda^2/2$, or crater diameters greater than or equal to 6, 60, and 500 m for $F_\lambda = 10$, 30, and 90, respectively.

When a law of the form $\cos^n \underline{I}$ is fitted to the scattering law $\sigma_o(\underline{I})$ calculated in Appendix H, $\underline{n}$ falls between 1.6 and 2.0 for all values of the model parameters associated with the curves in Fig. 11. These results are consistent with the corresponding exponents best describing the radar scattering from the Galilean satellites observed in 1976 and 1977, when the satellite radius was constrained to the optically derived value. Figure 12 shows $\sigma_o(I)$ for one set of model parameters, compared to the curve $\cos^2 \underline{I}$. The sharp change in curvature for $\sigma_o(\underline{I})$ at $\underline{I} = 45°$ results from the onset of shadowing of double-bounce echoes by the crater rim at that angle. As illustrated in Fig. 13, μ_C and μ_L, which are essentially constant for $\underline{I} < 45°$, begin to decrease at this point, falling to zero at the limb. Similarly, the power spectrum corresponding to the scattering law (Fig. 12) derived for a representative icy-crater model decreases more rapidly toward the limb than the spectrum for a Lambert law (Fig. 14). This predicted behavior provides a possible experimental test of my model, given sufficient sensitivity to and resolution of the limb echoes. Unfortunately, existing spectra are too noisy to assess the presence of model-predicted limb effects.

The model with ice alone ($\underline{m} = 1.78$) and facets no larger than 90 wavelengths (11 m), while able to accommodate the mean observed circular polarization ratios shown in

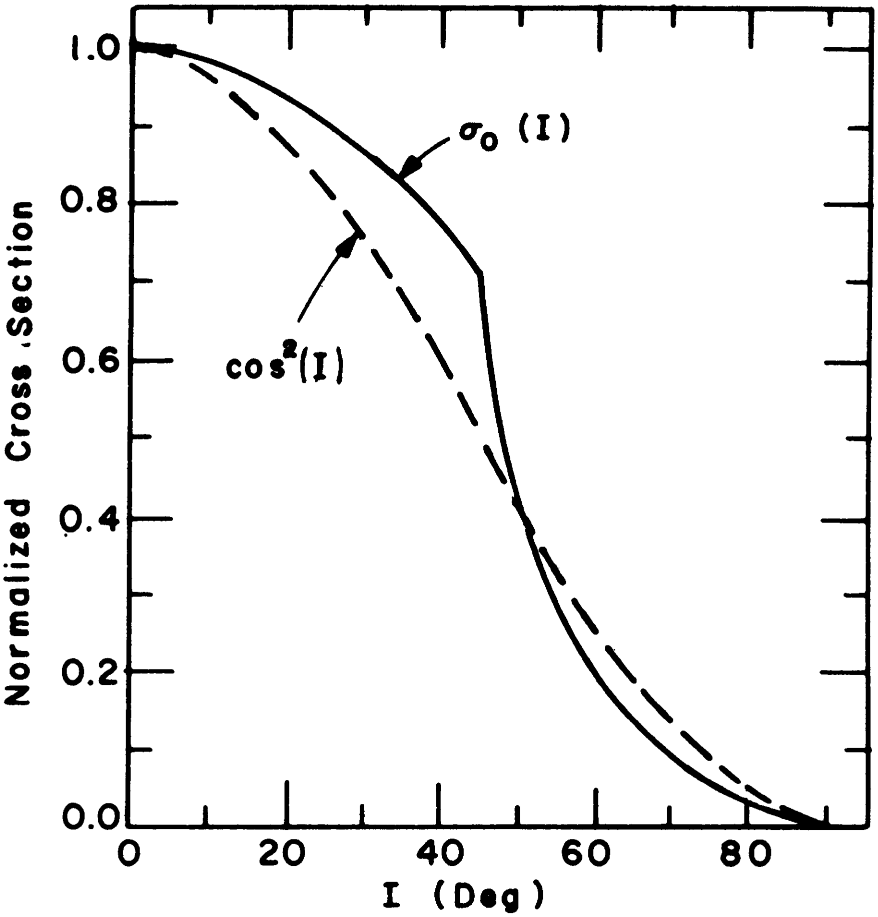

Fig. 12. Normalized scattering law $\sigma_o(\underline{I})$ for $\underline{m} = 1.78$, $F_\lambda = 90$, and $\varepsilon_c = 1°$, compared to $\cos^2 \underline{I}$.

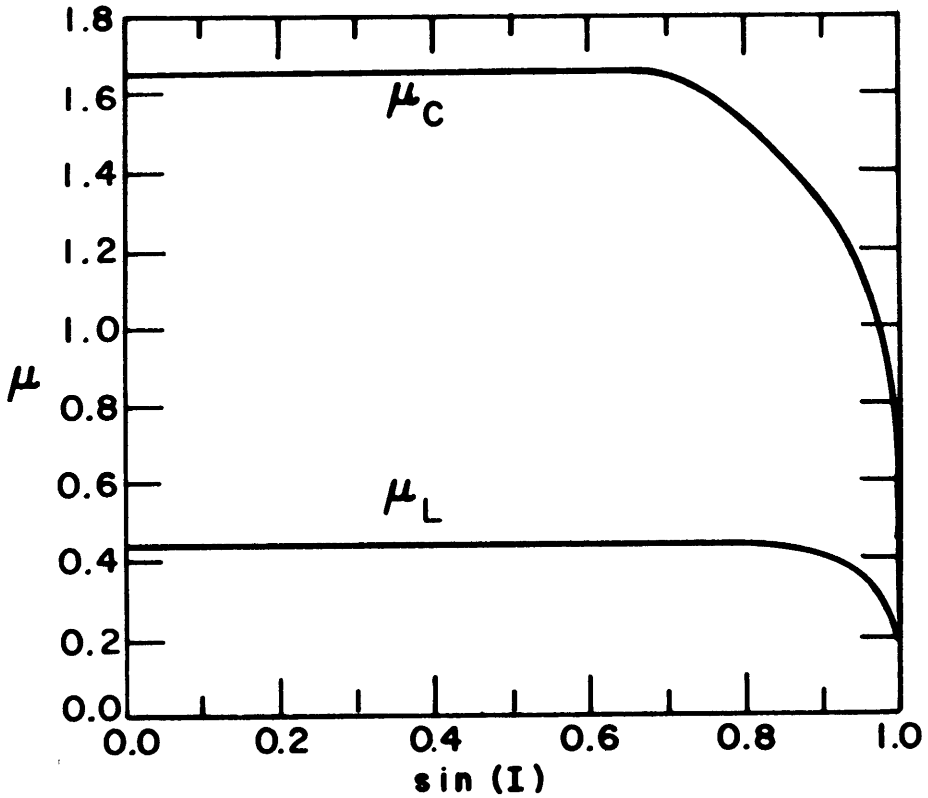

Fig. 13. The polarization ratios μ_C and μ_L for a representative set of model parameters (m = 1.78, $F_\lambda = 90$, $\varepsilon_c = 1°$), as functions of sin I, where I is the angle of incidence to the mean surface.

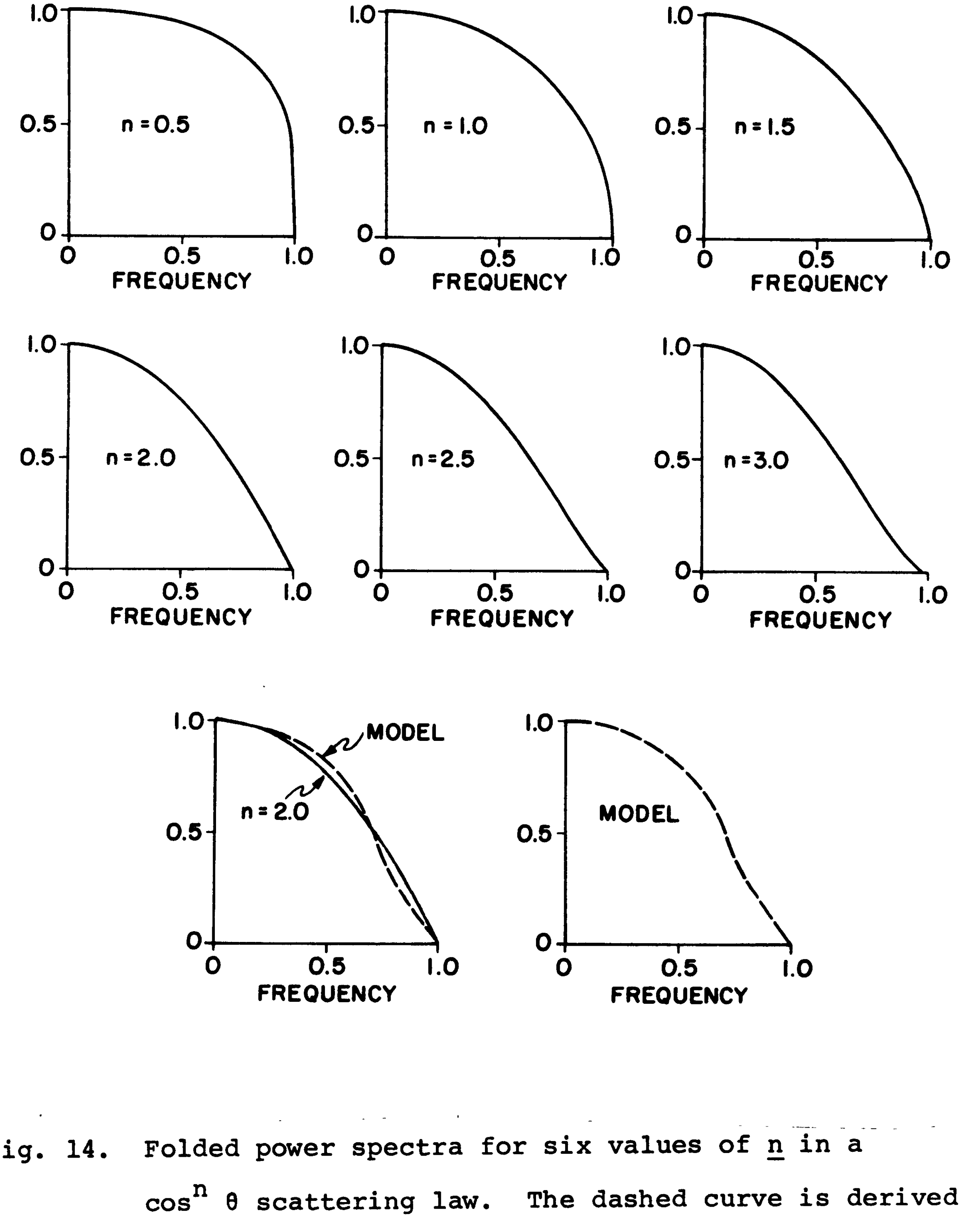

Fig. 14. Folded power spectra for six values of n in a $\cos^n \theta$ scattering law. The dashed curve is derived from the scattering law calculated for an icy-crater model with $m = 1.78$, $F_\lambda = 90$, and $\varepsilon_c = 1^\circ$.

Table VII, is unable to produce the albedos measured in 1976 and 1977 for Ganymede and Europa. Extremely large facets ($F_\lambda \sim 1000$) might resolve the discrepancy, but these seem unlikely. However, a value for the index of refraction intermediate between 1.78 (water ice) and 2.4 (a typical value for acidic rock) readily yields $\alpha \sim 0.4$ for facets having $F_\lambda \sim 60$.

Figure 15 illustrates the effects of adding either completely polarized ($\mu_C = 0$) or completely unpolarized ($\mu_C = 1$) scattering components to the results produced by the model. In these mixed models, I assume the added component does <u>not</u> displace any part of the original. The curves, drawn for a particular set of model parameters, illustrate the reduction in μ_C resulting either from the addition of a component completely polarized in the sense corresponding to single-reflection backscattering, or of an unpolarized component such as might arise from multiple scattering. The circular ratio μ_C falls rapidly when a polarized component is added, dropping from the original value μ_C' to unity in the presence of a fraction of polarized power: $f_P = (\mu_C' - 1)/(\mu_C' + 1)$. The effect of an unpolarized component is less dramatic, so the albedo of any given model can be increased considerably without seriously degrading μ_C. The large scatter in μ_C <u>vs</u>. α determined for the outer three Galilean satellites (Fig. 16) could be due to an unpolarized component whose relative importance is a strong function of surface location.

If the refractive index of the surface is assumed to be

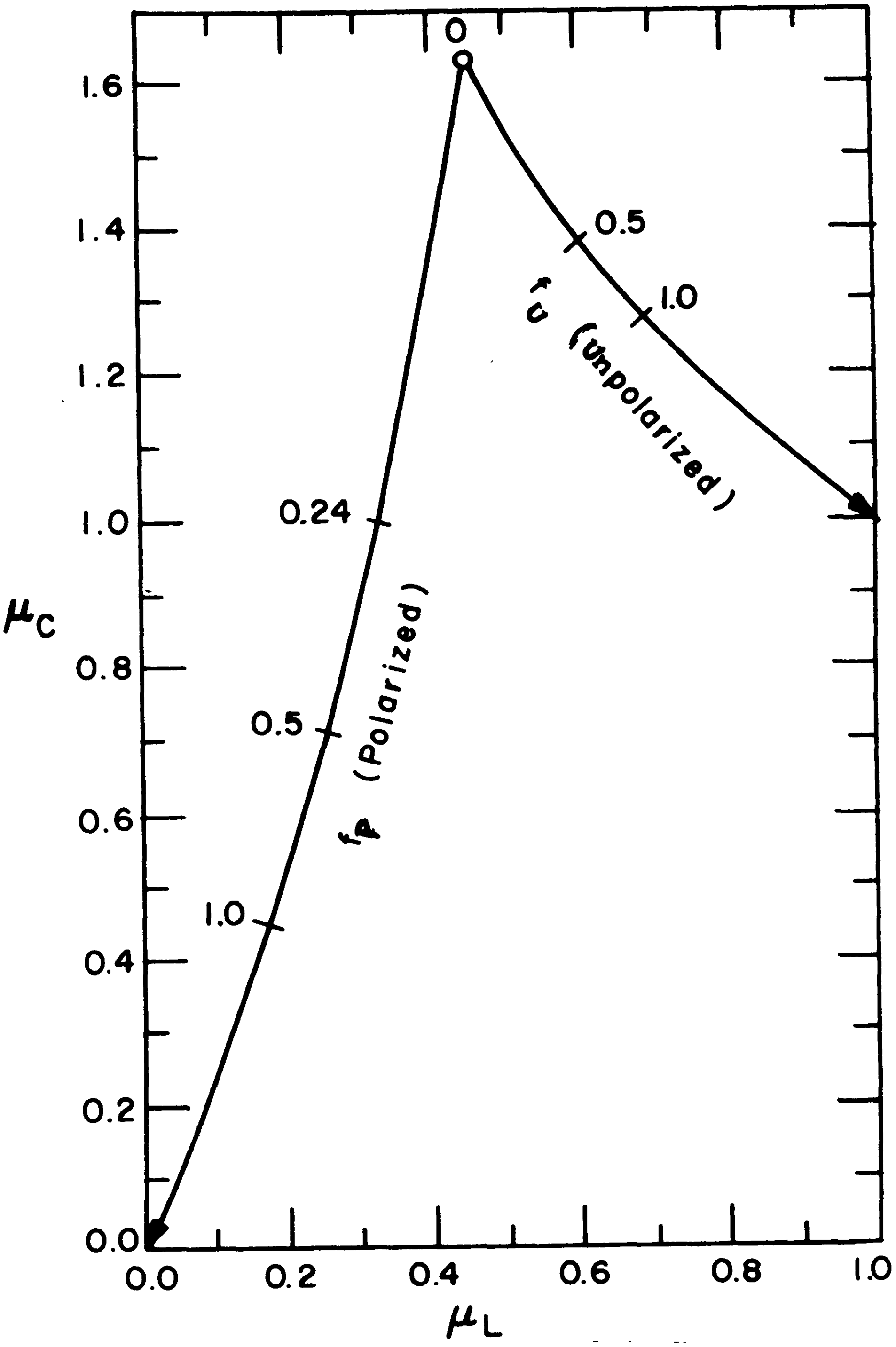

Fig. 15. Polarization ratios for icy-crater "mixed" models, which result from the addition of a fraction f_P of completely polarized power or a fraction f_U of completely unpolarized power, to a model with undiluted polarization ratios μ_C' and μ_L' equal to 1.64 and 0.45, respectively.

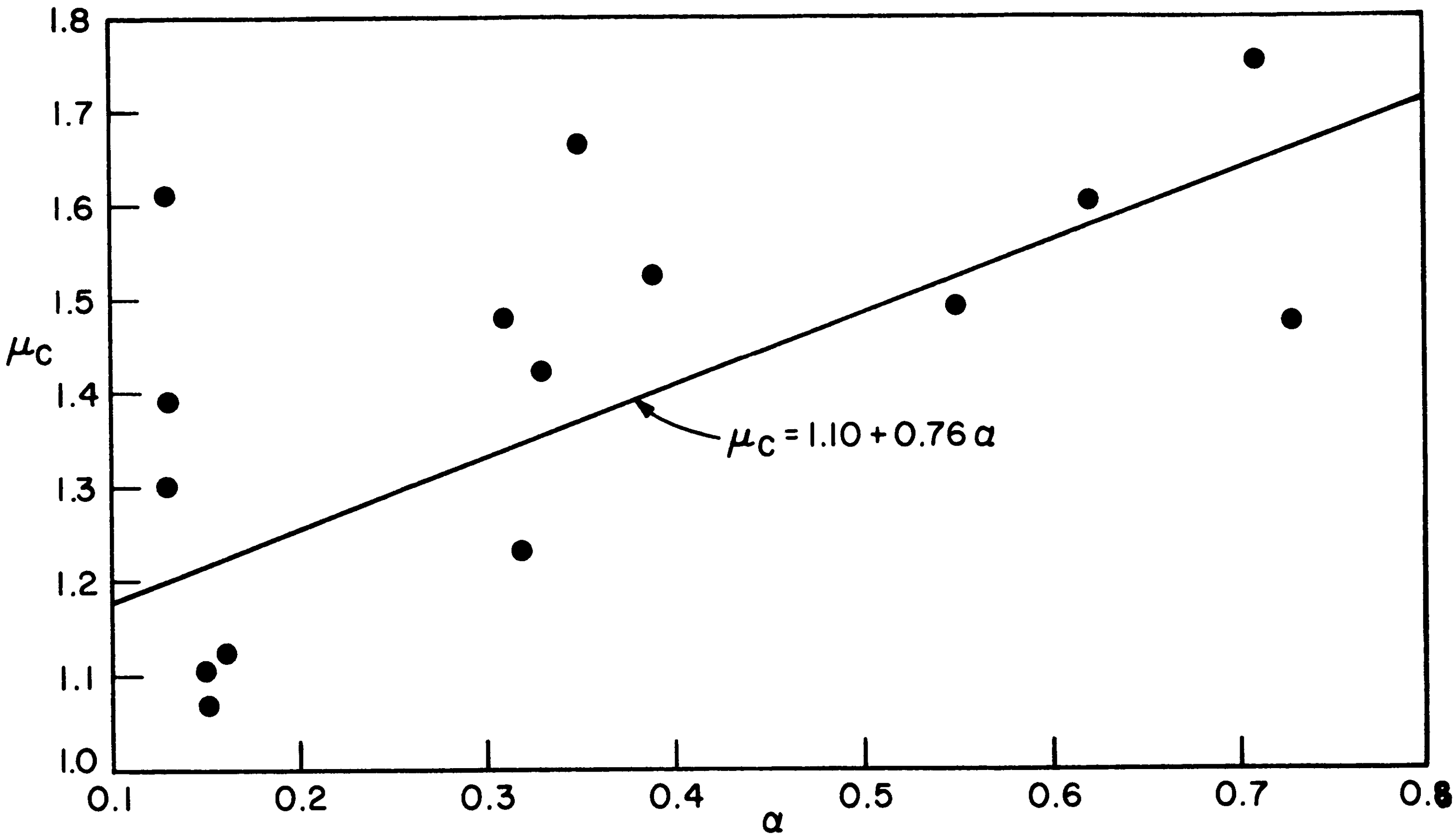

Fig. 16. Circular polarization ratio vs. geometric albedo for the outer three Galilean satellites. The weighted-least-squares best-fit straight line is also shown.

about 2.1, the model works very well and a variety of mixtures of scattering components become possible. For example, if 70% of the radar echo came from hemispherical craters with $\underline{m} = 2.1$, $F_\lambda = 90$, and $\varepsilon_C = 1°$, and 30% came from an added unpolarized component, even the observation of Europa on 20 November 1976, by CCOPS, giving $\mu_C = 1.75 \pm 0.29$ and $\alpha = 0.71 \pm 0.18$, could be satisfied. Although water ice is the only confirmed constituent of the satellite surfaces, it is probably mixed with other compounds. A solid, homogeneous combination of ice and , say, silicate material could have electrical properties intermediate to those of the individual substances. Another possible mechanism for increasing the index of refraction is to form an ice clathrate with a polar guest molecule (Hill et al., 1969).

Both the circular polarization ratio and the albedo decrease if the crater comprises less than a full hemisphere, i.e., if the rim is less than 90° from the crater bottom. For a rim $(90° - \tau)$ from the bottom, the fractional change in either μ_L, μ_C or α averages about -0.02/deg over the range $0° \leq \tau \leq 45°$. If the trim angle τ becomes larger than 25°, I can no longer match Europa's maximum observed albedo (0.73) for physically plausible values of the model parameters. In other words, because of the magnitude of the observed albedos, the crater depth-to-diameter ratio has a lower limit of about 0.35 for my model, in contrast to a ratio of about 0.2 actually measured for craters on the Moon, Mars and Mercury. However, as shown in Fig. 17, the polar-

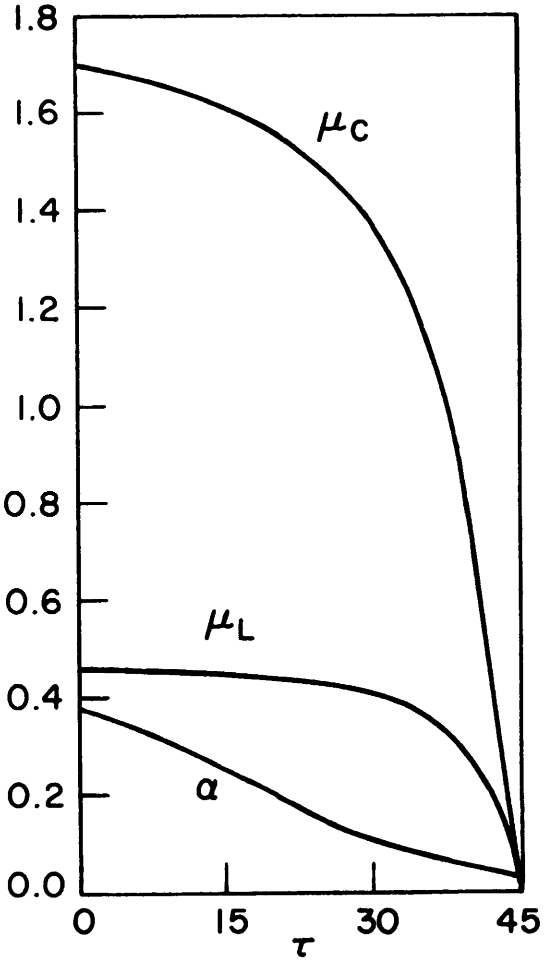

Fig. 17. Circular polarization ratio μ_C, linear polarization ratio μ_L, and geometric albedo α as functions of the trim angle τ for an icy-crater model with $\underline{m} = 1.78$, $F_\lambda = 90$, and $\varepsilon_c = 0°$.

ization ratios are quite independent of τ for $\tau \lesssim 30°$, i.e., for a depth-to-diameter ratio of $\lesssim 0.29$.

With the desirable scattering characteristics of large spherical craters established, I must now face up to the hard question of their existence on the surfaces of the Galilean satellites. To the best of my knowledge, the literature contains no good empirical information on the effects of hypervelocity, large-mass impact cratering of ice. Craters less than about 10 km in diameter on terrestrial bodies are frequently bowl-shaped (Smith and Sanchez, 1973) and there is evidence that craters formed in brittle materials are hemispherical but texturally uneven (Diedrich et al., 1965). However, large impact craters in the siliceous material of the inner solar system are rarely hemispherical. They are often eroded, partially filled in with rubble, and superimposed. To a limited extent, my model can accomodate the latter three characteristics. The interior surfaces need not consist of perfectly planar facets, since the geometrical optics approximation will remain valid as long as the local radii of curvature are everywhere large compared to the wavelength (12.6 cm). Furthermore, a pile of rubble at the bottom of each crater actually strengthens my model by suppressing single-bounce contributions near the subradar point more than it degrades double-bounce contributions at angles I near 45°.

Lack of sphericity is more difficult to accommodate. As indicated by the dependence of μ_C on ε_C, my model breaks down for even moderate departures from sphericity. Furthermore, because of their size, the craters must be assumed to date from an early epoch of the solar system. (The craters apparently must have minimum diameters on the order of several hundred kilometers, regardless of the physical interpretation of F_λ.) Johnson and McGetchin (1973) extrapolate the viscosity of ice measured at 268 K down to the surface temperatures of the Galilean satellites (about 135 K) and show that creep deformation should have obliterated all but the smallest and most recent craters. Their calculations are based on the extrapolated mechanical properties of pure water ice, however, and I note that the low-temperature viscosity of ice, and the reaction of ice to shock, have yet to be measured. There is evidence (Hobbs, 1974, p. 57) that at the surface temperatures of the Galilean satellites, water ice: Ic (with a cubic crystalline structure) may be more stable than hexagonal ice: Ih. Amorphous (vitreous) ice may also exist on these bodies. The physical properties of these exotic forms of ice are difficult to study in the laboratory and are poorly known. Furthermore, the modification of mechanical properties which results from admixture of ice with silicates or carbonaceous material is relatively unpredictable.

As an interesting example of such modification, I note that mixtures of soils and ice called "permacrete" have been used in polar regions as a construction material because of their apparent advantages over pure ice or even concrete

(Hobbs, 1974, p. 344). Ice mixed with starch, paper mash, or fibrous materials such as wood pulp is much stronger than ice alone. Perutz (1948) describes the discovery of this phenomenon during a World War II project, suggested by Geoffrey Pyke, to construct an iceberg aircraft carrier. Pure ice was found unreliable as a structural material because of an unpredictable resistance to explosive impacts. However, engineers found that (to quote Perutz) "inclusion of a small percentage [~4%] of wood pulp improved the mechanical properties of ice in a spectacular manner. In its resistance to projectiles and explosives, it was weight-for-weight as good as concrete. While a (pure) ice block 60-cm square and 28-cm thick was severely cracked by the impact of a revolver bullet, a similar block of pykrete (named after Pyke) suffered only insignificant damage, consisting of a crater about 2.5 cm in diameter and 1.2 cm deep."

A final difficulty in rationalizing the existence of a surface such as my model postulates lies in accommodating the full spectrum of overlapping crater sizes expected to have been produced by meteoritic infall. The scattering properties of craters too small for my geometrical optics approach to treat are unknown, although they may well possess at least some of the desired characteristics. Their presence on the inner surfaces of the large craters upsets the symmetry demanded by the model, however, and may lead to a degradation in the desired scattering properties of the large craters. The recent measurement (Goldstein, 1978) of

$\mu_c \approx 1.8$ for Ganymede at $\lambda = 3.5$ cm may indicate that craters in a certain size range backscatter with higher values of μ_c at a wavelength of 3.5 cm than at a wavelength of 12.6 cm.

Meanwhile, I continue to defend the assumption of hemispherical icy craters on two grounds: First, I have not yet conceived any other approach that appears to explain the observed polarization ratios. Second, I feel that present knowledge of the Jovian environment and its past history, of the composition of the Galilean satellite surfaces, and of the effects resulting from hypervelocity impacts on ice is too limited to preclude the possibility that surfaces consistent with the major premises of my model exist.

In conclusion, it appears that a model which postulates that significant parts of the surfaces of Europa, Ganymede and Callisto are covered with an icy layer at least several kilometers thick and saturated with hemispherical craters can explain nearly all the observed radar behavior. Furthermore, despite its imperfections, no other physically plausible model appears to be compatible with the observations. While the circumstances of this model have been explored for an appreciable variation in its parameters, much further work obviously remains to be done. A more thorough analysis of the dependence of μ_c and α on ε_c would certainly be useful. Also, models having either a distribution of facet sizes or more realistic angular distributions $P(\varepsilon)$ have yet to be investigated. A particularly challenging project would be a physical optics formulation of the problem of scattering from hemispherical craters.

In the same vein, more complete measurements of the radar backscattering properties of the Galilean satellites, with improved accuracy and finer frequency resolution, would narrow the range of acceptable model parameters and permit the testing of some of the model's predictions.

II. E. Surfaces of the Galilean satellites: Conclusions

The values for μ_C which exceed unity, measured in 1976 and 1977 for Europa, Ganymede, and Callisto, are the most striking aspect of these objects' radar scattering behavior. The correlation among μ_C, α, $\underline{p}$ and surface frost coverage suggests that the previously unobserved radar properties are related to the presence of surface layers of water ice which are much thicker than a radar wavelength. This conclusion is supported by the apparent similarity in reflectivity variations with orbital phase, when viewed at radar and visible wavelengths.

The hypothesis that the circular-polarization behavior is caused by double-reflection backscatter from nearly hemispherical icy craters is certainly not free from difficulty, but stands as the only currently proposed explanation for how μ_C can exceed unity. If the first- and second-order scattering from icy craters is supplemented by a depolarized ($\mu_C \approx 1$) return arising from additional scattering processes, the model can account not only for the observed circular and linear polarization ratios and angular scattering laws, but also for the large geometric albedos as well. The weakness of the μ_C/α correlation for observations of a given satellite at different orbital phases can be taken as evidence for the existence of just such an additional component. Indeed, any of the processes invoked (Chapter I) to explain the depolarization of echoes from the

Moon and Venus may also be operating on the Galilean satellite surfaces.

The correlation between μ_C, α, $\underline{p}$ and fractional frost coverage for Europa, Ganymede, and Callisto may reflect differences in overall crustal compositions as determined by different geochemical histories (Consolmagno and Lewis, 1978), as well as differences in susceptibility to erosion and other surface-altering processes.

Variations in μ_C, α, $\underline{n}_R$, and spectral shape as a function of Φ suggest the presence of surface inhomogeneities on Europa, Ganymede, and Callisto. As argued above, the areal extent of many of the surface features on the three satellites seems somewhat smaller than hemispherical in scale. On the other hand, similarity of the radar and visible-wavelength brightness curves, if significant, could mean that there are intrinsic differences in the surfaces of the satellites' leading and trailing hemispheres.

III. SATURN'S RINGS

III. A. Radar picture of the rings prior to thesis work

Saturn's rings present particular problems to radar detection at Arecibo, not the least of which is the greater than two-hour time delay, which, because of sky coverage constraints at Arecibo, limits the duration of observation to about half an hour per night. As with the Galilean satellites, observations are planned to coincide with Saturn's closest approach, i.e., at opposition. Because of the inclination of the ring plane to the ecliptic, the "opening angle" $\underline{B}$ (the Saturnocentric declination of Earth) varies from year to year. Thus the projected area of the ring plane and the fraction of the rings that is visible also vary between observations at different apparitions. In this sense, the rings present a time-variable radar target.

Interpretation of the results of radar observations of the rings compounds the challenge of making the observations. The ring-particle composition, size, shape, and spatial distribution are essentially unknown. In addition to a dependence on radial distance from the center of Saturn, there is also a suggestion that some properties also depend on azimuthal position. To model the bulk scattering properties of the rings at any given wavelength generally demands an assessment of (1) the relative importance of Rayleigh, Mie, and Fresnel single scattering, and (2) the relative importance of single scattering *vs.* multiple scattering. Finally, any physically acceptable model of Saturn's rings must be consistent with the results of passive microwave, optical and infrared observations at various wavelengths as well as with the radar results.

In this section I discuss the radar experiments prior to my observations without dwelling on the interpretation of results. In Sections B and C, I describe the 1976 delay-Doppler study (Pettengill, Ostro, Campbell and Goldstein, 1979) and the 1977-1978 CW studies (Ostro and Pettengill, 1979), respectively, in which μ_C and α were first measured at 12.6-cm wavelength. Detailed discussions of the radar properties of the rings, including synthesis of the results of all radar work to date, is presented in Sections D, E, F and G. The final section (H) of this chapter contains my conclusions concerning constraints on the structure of the rings.

For Saturn's rings, the projected target area to which radar cross section and geometric albedo are normalized corresponds to one or more of the major ringlets into which the rings as a whole are divided. (The question of *particle* cross section is more complex.) The best *a priori* estimate of ringlet boundaries for use at radar wavelengths is based on years of optical observations. To expedite comparison of several radar studies from 1973 to 1978, I have adopted my own "canonical" ringlet dimensions, as presented in Appendix K, and have normalized all cross sections and albedos to the visible projected area of the combined A and B rings.

The first radar detection of the rings was achieved by Goldstein and Morris (1973), using the Jet Propulsion Laboratory's "Mars" antenna system. In this work they averaged CW observations made in December 1972 and January 1973 at 12.6-cm wavelength, using the "OC" sense of polarization, with the results reproduced in Fig. 18. In developing a theoretical comparison, they assumed a B-ring reflectivity twice that of ring A and calculated a theoretical spectrum, shown as the dashed curve in Fig. 18. Their data appeared to be consistent with homogeneous scattering from the optically defined A and B rings, except at Doppler shifts corresponding to echoes near the center of the observed power spectrum, where the echo strength exceeded that predicted. Goldstein and Morris suggested that the source of this "low-Doppler excess" (LDE) could be diffuse reflection from Saturn itself if the planet had a reflectivity of 13%, or from ring particles at greater radii than those seen optically.

Goldstein and Morris (1973) determined a value for σ_{OC} of 0.68 (Goldstein <u>et al</u>., 1977) at a ring opening angle $|B| = 26.4°$. Such a high cross section was the first indication that a substantial portion of the ring particles must be at least several centimeters in size.

A more extensive study of the rings was undertaken in December 1974 and January 1975 by Goldstein <u>et al</u>. (1977) at $|B| = 24.4°$. In this study, monostatic, 3.5-cm, circularly polarized CW observations were made at JPL; furthermore,

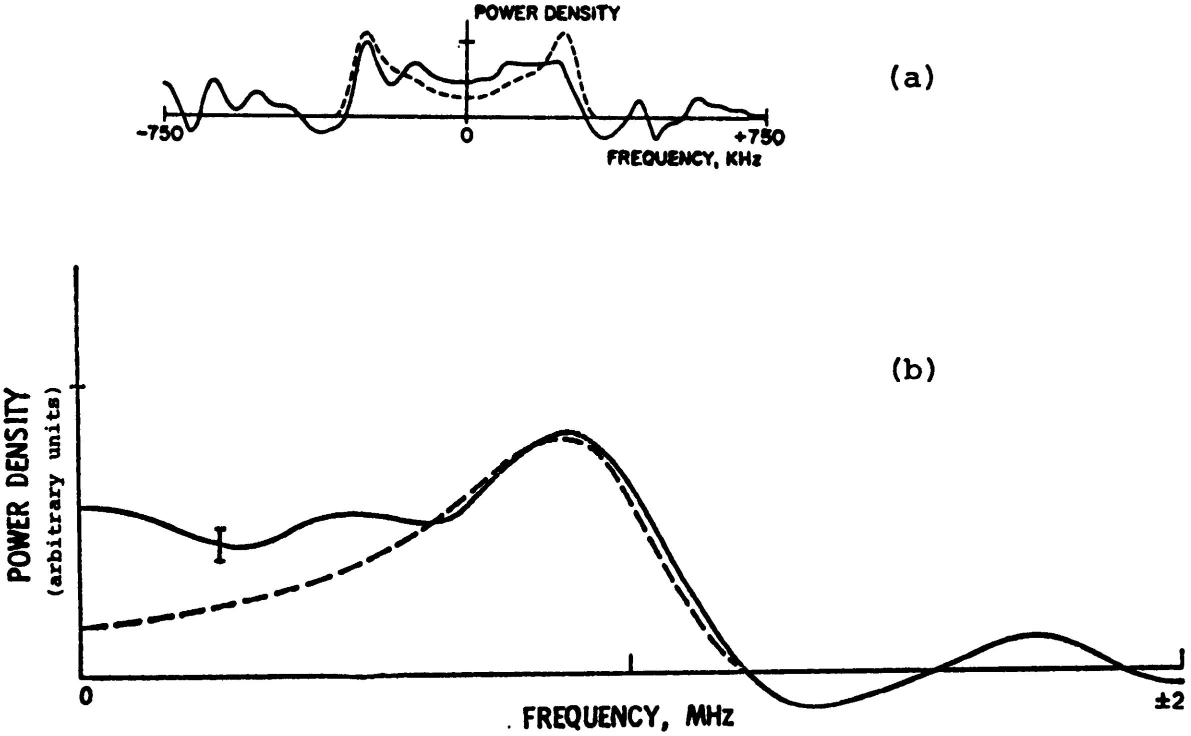

Fig. 18. (a) is a reproduction of the 12.6-cm Saturn's rings spectrum obtained by Goldstein and Morris (1973). (b) is a reproduction of the 3.5-cm folded spectrum obtained by Goldstein *et al*. (1977). The error bar is plus and minus one standard deviation. The spectra in both (a) and (b) are compared to that expected from an isotropic ring model with an A:B-ring reflectivity ratio of one half (dashed curve).

bistatic, 12.6-cm, linearly polarized CW observations were also conducted, with reception at Goldstone (alternating every 15 minutes between "SL" and "OL" polarization) of Arecibo's transmission. This group reported values of $\mu_C = 1.00 \pm 0.25$ and $\sigma_{OC} = \sigma_{SC} = 0.68 \pm 0.13$ (corresponding to $\alpha = 0.34 \pm 0.06$) at 3.5 cm, and a value of $\mu_L = 1.0 \pm 0.3$ at 12.6 cm. Figure 18 shows their 3.5-cm "TC" spectrum, folded about the Doppler frequency corresponding to the Saturn system center of mass under the assumption of "left/right" (+/- relative Doppler shift) symmetry. Comparison with their model, which again assumed an A-ring-to-B-ring reflectivity ratio of 0.5, clearly shows a strong LDE, "amounting to about 18% of the total received power."

Goldstein et al. (1977) offer three possible explanations for the LDE: (1) ring-plane particles beyond the outer edge of ring A; (2) a halo of particles out of the visible ring plane, orbiting in planes highly inclined to the line of sight; or (3) particles suspended in the Saturn atmosphere, corresponding to a component of cross section for Saturn itself of $\sigma_{OC} \approx \sigma_{SC} \approx 0.15$.

In summary, the 1973-1975 observations showed that (1) Saturn's rings backscatter and depolarized both 12.6-cm and 3.5-cm radar waves with remarkable efficiency, as compared to scattering observed from the inner planets; and (2) the assumption of symmetric scattering from the A and B rings, with the A:B reflectivity ratio taken to be one half, satisfactorily explains the essential shape of the power spectrum, except at low absolute Doppler shifts, where an excess is observed.

III. B. The 1976 observations: Delay-Doppler resolution of the rings

The pre-1976 results suggested that the optically defined A and B rings were responsible for most of the observed radar echoes from the rings; however, the source of the LDE was unknown. In an attempt to determine directly the spatial distribution of radar backscattering particles, a measurement which obtained useful resolution of the echoes from the ring system simultaneously in both delay and Doppler shift was undertaken. Figure 19 shows ring-plane contours corresponding to constant Doppler shift and delay for ring particles freely orbiting Saturn; also shown are the boundaries of the ringlets defined in Appendix K. The values given for the contours are calculated for $|B| = 21.4°$, corresponding to January 1976, and must be scaled by $\cos B / \cos 21.4°$ for other values of $\underline{B}$. The calculations used in Fig. 19, including those accounting for the shadowing of the rings by the planet, are described in Appendices F and L.

The transformations between geometric location and time delay and Doppler shift are quite different for the rings as compared to corresponding transformations for scattering elements located on a rotating rigid sphere. The rings occupy a spectral bandwidth of more than half a megahertz at S-band and extend over nearly two seconds in delay. Echoes at a particular delay-Doppler coordinate can originate from particles widely separated in space, in analogy with the

Fig. 19. Contours of constant delay and Doppler shift, drawn in the plane of Saturn's rings for $\underline{B} = 21.4^{\circ}$. The value (113 msec) of the delay bias shown here corresponds to an average for the six data sets obtained in 1976. The effective delay resolution is sketched on the right. Ringlet boundaries and Saturn's shadow are also indicated.

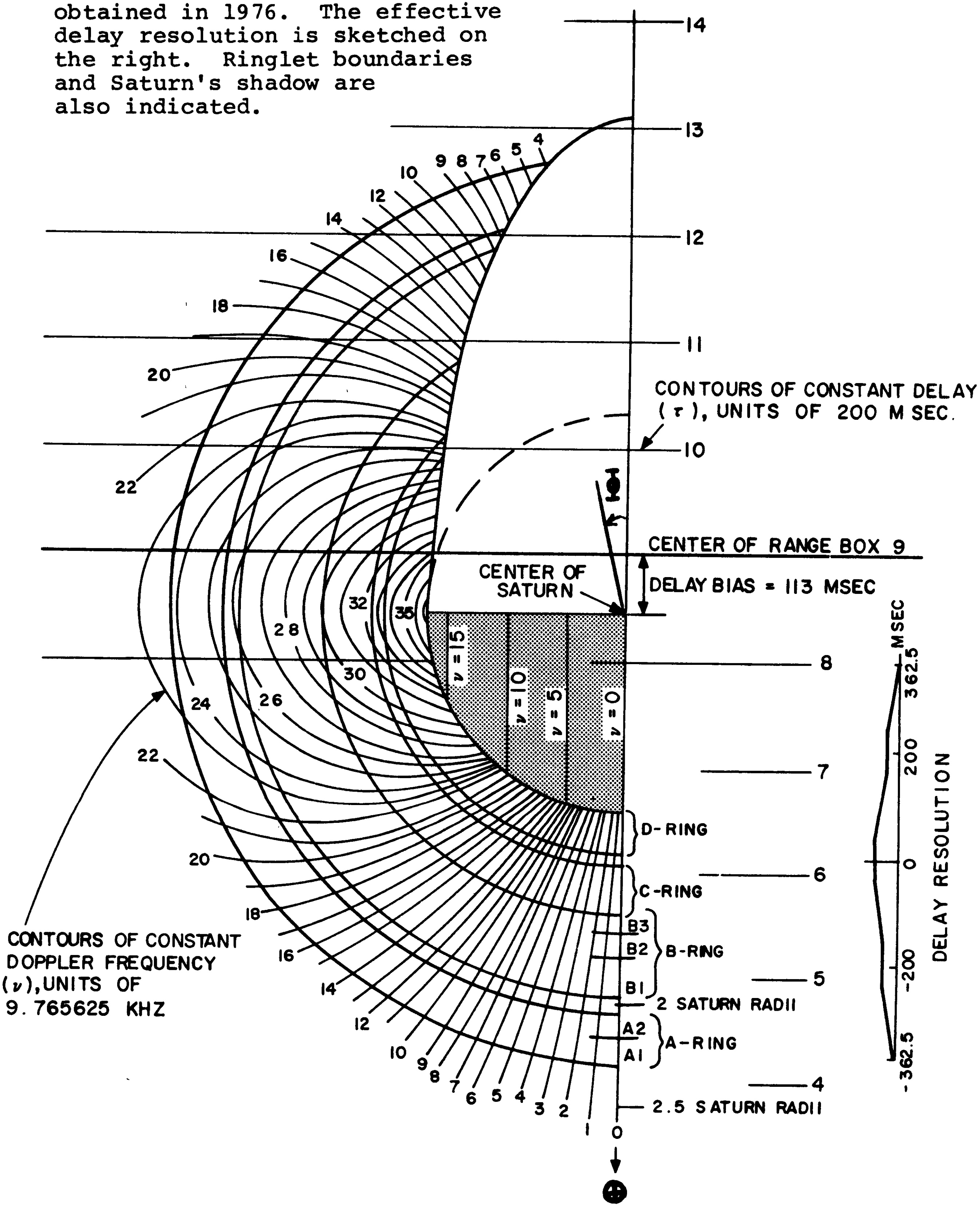

hemispheric ambiguity associated with echoes from a rotating rigid sphere (Campbell, 1971).

Saturn's rings are extremely overspread (delay depth times spectral bandwidth $\gg 1$) and cannot be simultaneously investigated in both delay and Doppler with coherent-pulsed or phase-coded CW waveforms without aliasing (Green, 1968). This obstacle was partially overcome (Pettengill, Ostro, Campbell and Goldstein, 1979) in January 1976 with a monostatic/bistatic, 12.6-cm, linearly polarized experiment using a frequency-stepped CW waveform. The Arecibo transmitter was cycled among eight discrete carrier frequencies located at 1-MHz intervals and distributed over an 8-MHz band centered at 2380 MHz. The dwell time at each frequency was 400 msec, giving the entire sequence a 3.2-sec delay ambiguity (which comfortably exceeded the expected delay distribution of the radar echoes). Echoes were received at both Arecibo and Goldstone. Despite the fourfold larger integration time available at Goldstone, the bistatic echoes were much weaker than the monostatic echoes because of the relatively small size of the Goldstone antenna. Nevertheless, the two modes of operation provided a useful check between the data reception and reduction procedures used at both sites.

During reception, the first local oscillator was continually adjusted to remove the Doppler shift arising from Saturn's apparent line-of-sight relative velocity. In a similar fashion, the sampling of the echoes was "drifted" in time to compensate for the changing delay to Saturn. The resulting sequential samples of echo amplitude were clipped, correlated and accumulated as described in Appendix B. The autocorrelator output, integrated for 125 msec, was transferred to digital magnetic tape every 200 msec. Two successive 200-msec data sets correspond exactly to the 400-msec dwell interval of the originally transmitted sequence of frequencies. Thus the echo was oversampled in delay by a factor of two, compared to the minimum resolution necessary, and 16 power spectra were obtained for each 3.2-sec receive-cycle, yielding the overlapping delay resolution sketched in Fig. 19.

After autocorrelation and storage, the data were subsequently sorted, stacked and summed, resulting in 16 autocorrelation functions. These were then Fourier-transformed with ~10-kHz resolution to yield 16 spectra, one for each half-dwell "range box".

The range box corresponding approximately to the center of Saturn could be predicted from the a priori ephemeris. However, the echoes were strong enough to locate this central range box from the appearance of the spectra, even prior to removal of the background filter shape. The 16-range-box sequence of spectra was then cycled such that the range box positioned at the smallest positive (i.e., excess) delay relative to the center of mass of Saturn was called number 9; the original order of the range boxes was maintained (Fig. 19). The "end" range boxes (numbers 1 and 16) thus contained only background noise power and could be used to estimate the level of rms fluctuations in the noise. The baselines determined in this fashion were then removed from the remaining 14 spectra.

Five nights' observations yielded six independent subsets of observations with useful signal strength. The corresponding integration times are listed in Table VIII. The total data spectrum (integrated over all data sets and all 14 rangeboxes for each data set) is shown in Fig. 20. For each run, the 14 single-rangebox spectra were folded about their zero-Doppler centers to enhance the signal-to-noise ratio and to partially compensate for possible asymmetries resulting from antenna tracking errors.

Using the numerical model of the Saturn system described in Appendix F, weighted-least-squares regression was used to assess the relative backscattering efficiency of particles at selected radii lying in rings A, B, C, and D, as well as in (1) an A' ring, extending from 2.3 to 2.65 Saturn radii; (2) an X ring, interior to the inner edge of the D ring, orbiting within the Saturn atmosphere but at Keplerian velocities; and (3) a P "ring" of particles uniformly distributed over the visible Saturn "surface" and corotating with the planet. A delay bias parameter $\hat{\tau}$, equal to the delay of the center of Saturn relative to the middle of range box number 9, was also estimated from each run's data. Because of the delay oversampling, data at a particular frequency but in adjacent range boxes were correlated

TABLE VIII. Least-squares estimates of the delay bias parameter $\hat{\tau}$ for Saturn's rings 1976 delay-Doppler data. Here, $\hat{\tau}$ is defined as the delay of rangebox number nine relative to the center of Saturn (Fig. 19).

Run #	Date (Jan 1976)	Receive start time	Duration of observation (sec)	$\hat{\tau}$ (msec)
1	19	01 30 30	2220	57±9
2	22	01 24 30	1808	79±9
3	25	01 09 40	2124	77±10
4	26	01 02 50	1120	150±15
5	26	01 25 40	844	188±21
6	27	01 08 40	1676	153±14

Fig. 20. Saturn's rings 1976 spectrum, smoothed to 50-kHz resolution. Arrows show positions of the spectral "edges" expected from a model with just A and B rings. The "two-sided" spectrum in (a) has been folded about zero Doppler frequency in (b). The spectrum for the best-fit two-parameter model (Table IX) is shown as the dashed curve.

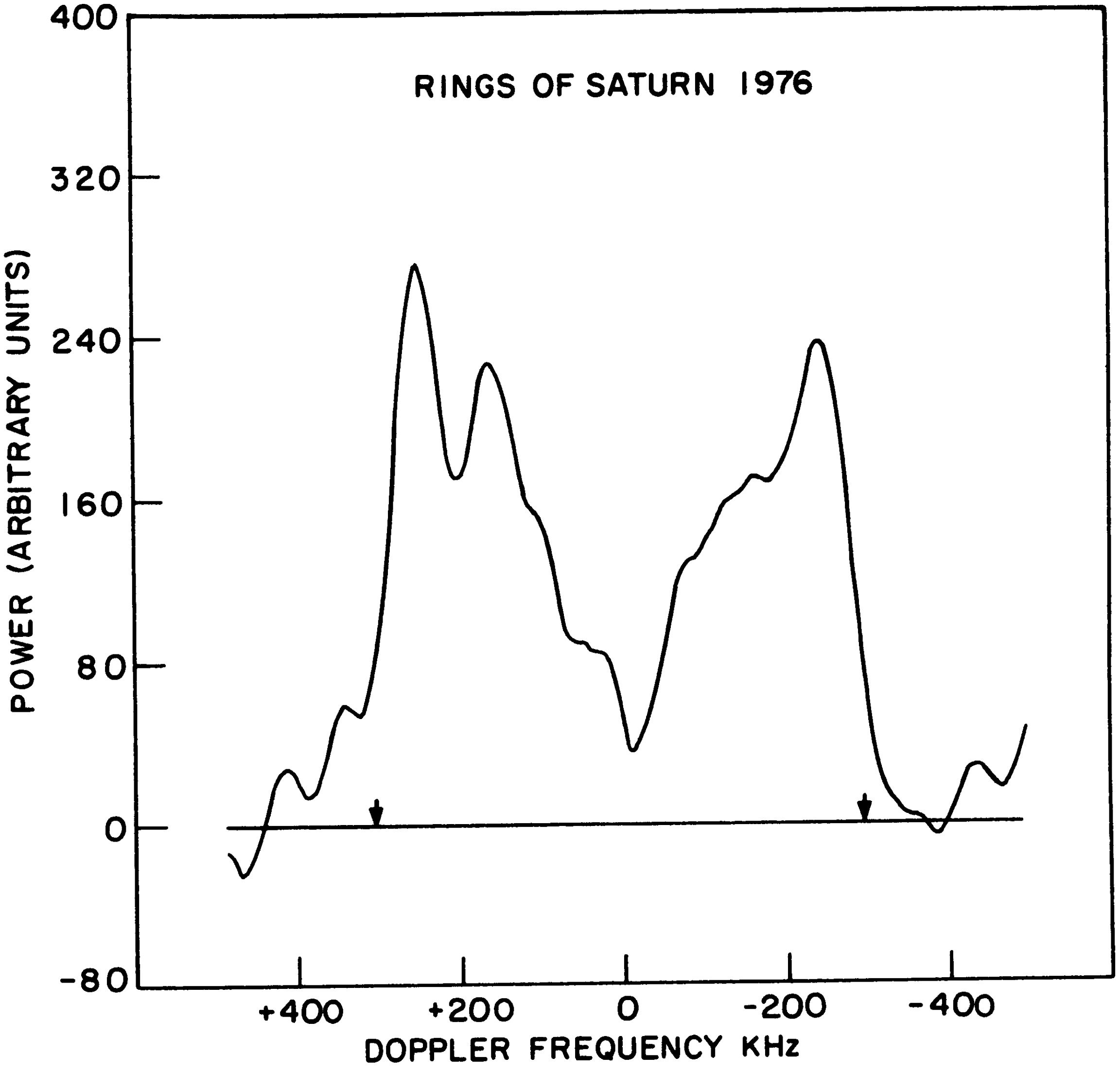
RINGS OF SATURN 1976
POWER (ARBITRARY UNITS)
400
320
240
160
80
0
-80
+400
+200
0
-200
-400
DOPPLER FREQUENCY KHz

Fig. 20a

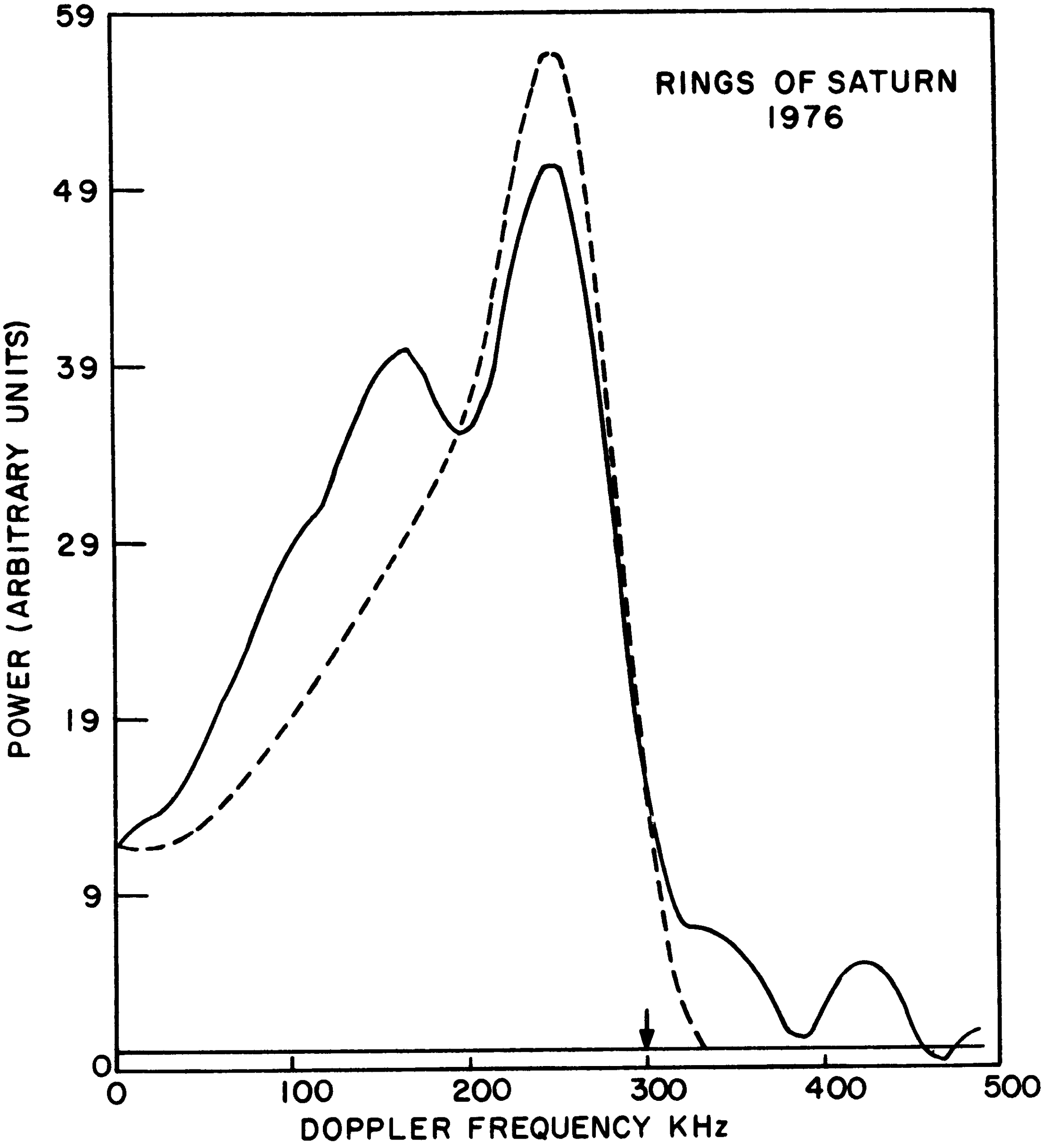
RINGS OF SATURN
1976
POWER (ARBITRARY UNITS)
DOPPLER FREQUENCY KHz
0
9
19
29
39
49
59
0
100
200
300
400
500

Fig. 20b

and had to be weighted accordingly in the parameter estimation calculations (Appendix E).

Table VIII lists the best estimates of $\hat{\tau}$ obtained for each run. There was no evidence, either in the appearance of the spectra or in the least-squares estimations obtained from them, of a significant echo component corresponding to any of the model's A', X, or P rings. On the other hand, the parameters corresponding to the A- and B-ring reflectivities yielded statistically significant results.

Fixing the delay-bias parameters to their estimated values, and eliminating the A', X, and P rings, I then employed a second model with seven parameters to assess in detail the radial distribution of scatterers within the region occupied by the A, B, C and D rings.

In this model, the A and B rings were subdivided as described in Appendix K so that the seven parameters corresponded to relative reflectivities of ringlets A1, A2, B1, B2, B3, C, and D, as shown in Fig. 19.

For each of the six runs, the rms noise fluctuation was determined from data at spectral locations known to be free from echo power. The formal errors corresponding to estimates of parameters from an individual data set are proportional to this rms noise level, but have been scaled to give a goodness-of-fit χ (Appendix E) equal to unity.

The estimates of ring reflectivities for the six runs have been combined into a final weighted average, normalized so that the strongest ringlet (B1) has unity reflectivity.

The results, presented in Table IX and Fig. 21, constitute the best estimate of relative reflectivities for the seven-parameter model. Results for a five-parameter model containing neither a D ring nor a C ring, are also shown. When a simple two-parameter model with just an A ring and a B ring is fitted to the data, the six-run best estimate of the A:B reflectivity ratio is 0.86 ± 0.06. The 6-run average goodness-of-fit X is shown in Table M for the seven-, five-, and two-parameter estimations. Clearly, the two parameter model is a fair approximation of the better, but more complicated, five- and seven-parameter models.

The best-fit model for any given run depends on that run's delay bias. As is evident from Table VIII, the six runs fall conveniently into two groups of runs with nearly the same delay biases. The delay-Doppler data have been separated accordingly, summed, and plotted in Figs. 22a,b. Also shown, as the solid curves, are the reconstituted spectra for each range box corresponding to the best-fit seven-parameter model. These models incorporate average values of delay bias, and have been adjusted in amplitude only. Comparison with results of other radar observations of the rings will be facilitated by Fig. 20b, which shows a folded spectrum, integrated over all six runs, and smoothed to 50-kHz resolution. A similarly filtered, amplitude-adjusted, best-fit two-parameter model is given as the darker curve in Fig. 20b.

The measured value of the "SL" cross section for January 1976, normalized to the projected A-plus-B-ring visible area

(Appendix K), was $\sigma_{SL} = 0.83 \pm 0.21$. A single night was spent on an unsuccessful attempt to measure μ_L. Assuming that $\mu_L \approx 0.4$, for reasons to be discussed in Section III. D, one can estimate $\alpha \approx 0.29$ for this data.

TABLE IX. Saturn's rings 1976 estimates of ringlet relative reflectivities.

Ringlet	Boundaries	7-Parameter model	5-Parameter model	2-parameter model
D	1.010-1.220	0.22±0.11	--	--
C	1.280-1.530	0.06±0.08	--	--
B3	1.530-1.625	0.76±0.20	0.89±0.17	1.00
B2	1.625-1.755	0.57±0.14	0.56±0.14	
B1	1.755-1.950	1.00±0.08	1.00±0.08	
A2	2.030-2.165	0.74±0.10	0.73±0.10	0.86±0.06
A1	2.165-2.290	0.68±0.10	0.67±0.10	
Ave. "goodness of fit" χ		.932	.934	.935

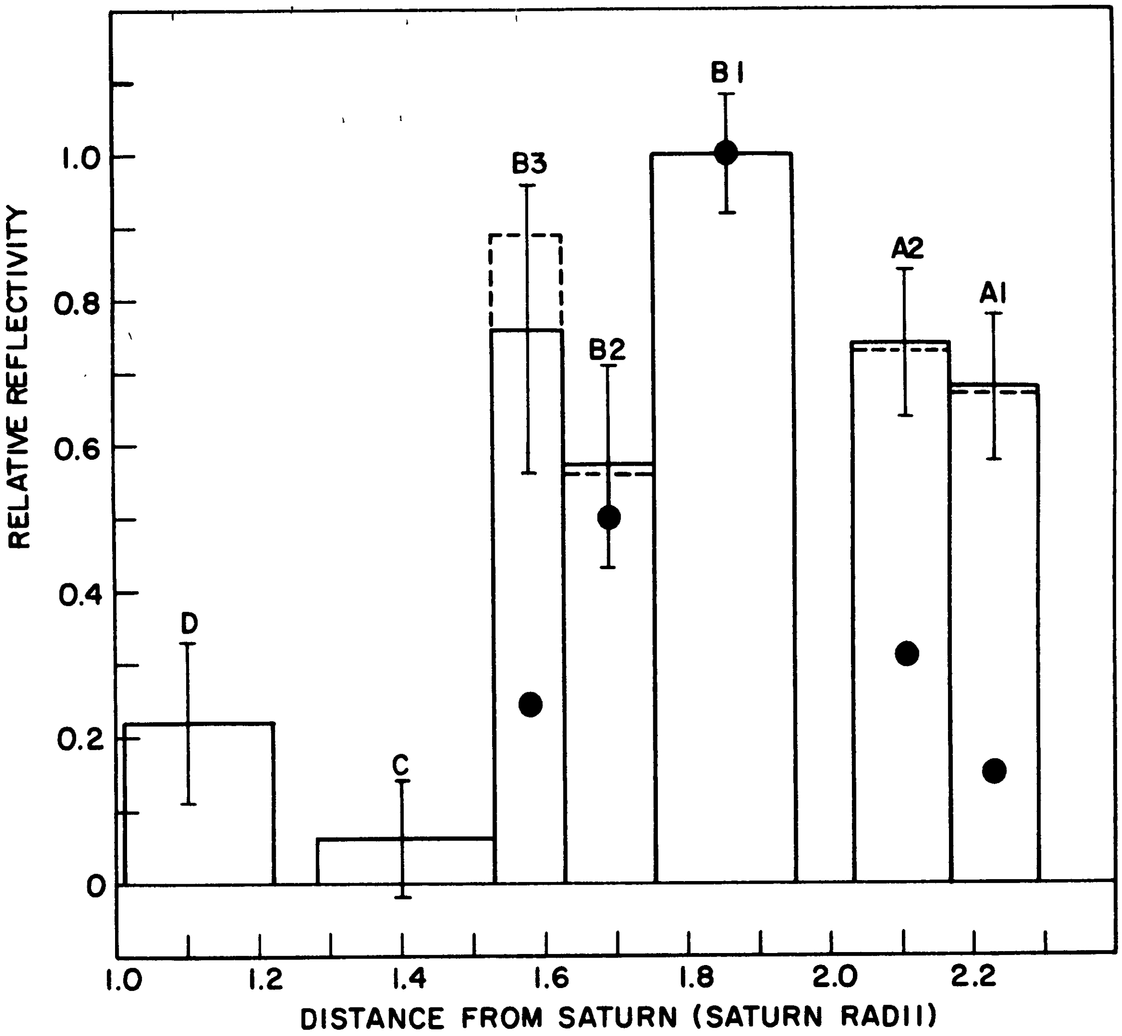

Fig. 21. Weighted-least-squares estimates of ringlet relative reflectivity for a seven-parameter model are shown. Vertical lines indicate plus and minus one standard deviation of formal error. Dashed lines show the results of a five-parameter (no C or D ring) estimation (see text). Large dots denote estimates of ringlet relative optical depth after Cook *et al.* (1973).

Fig. 22. Saturn's rings 1976 delay-Doppler data. Folded spectra for the 12 central range boxes are shown at 10-kHz resolution. (a) and (b) correspond to summations of data sets with similar values of delay bias, as discussed in the text.

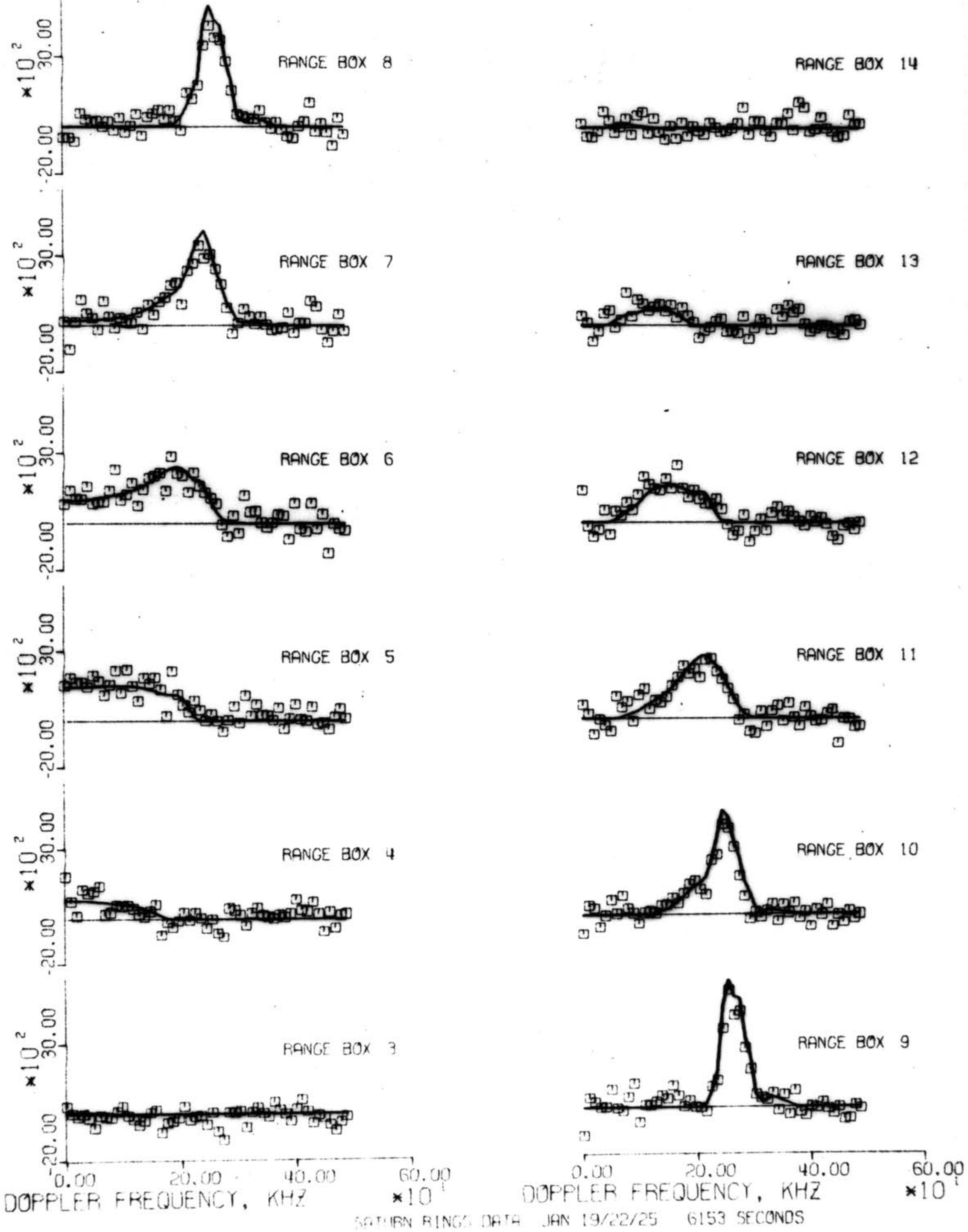
RANGE BOX 8
RANGE BOX 7
RANGE BOX 6
RANGE BOX 5
RANGE BOX 4
RANGE BOX 3
RANGE BOX 14
RANGE BOX 13
RANGE BOX 12
RANGE BOX 11
RANGE BOX 10
RANGE BOX 9
×10²
30.00
-20.00
0.00
20.00
40.00
60.00
×10¹
DOPPLER FREQUENCY, KHZ
SATURN RINGS DATA JAN 19/22/25 6153 SECONDS

Fig. 22a

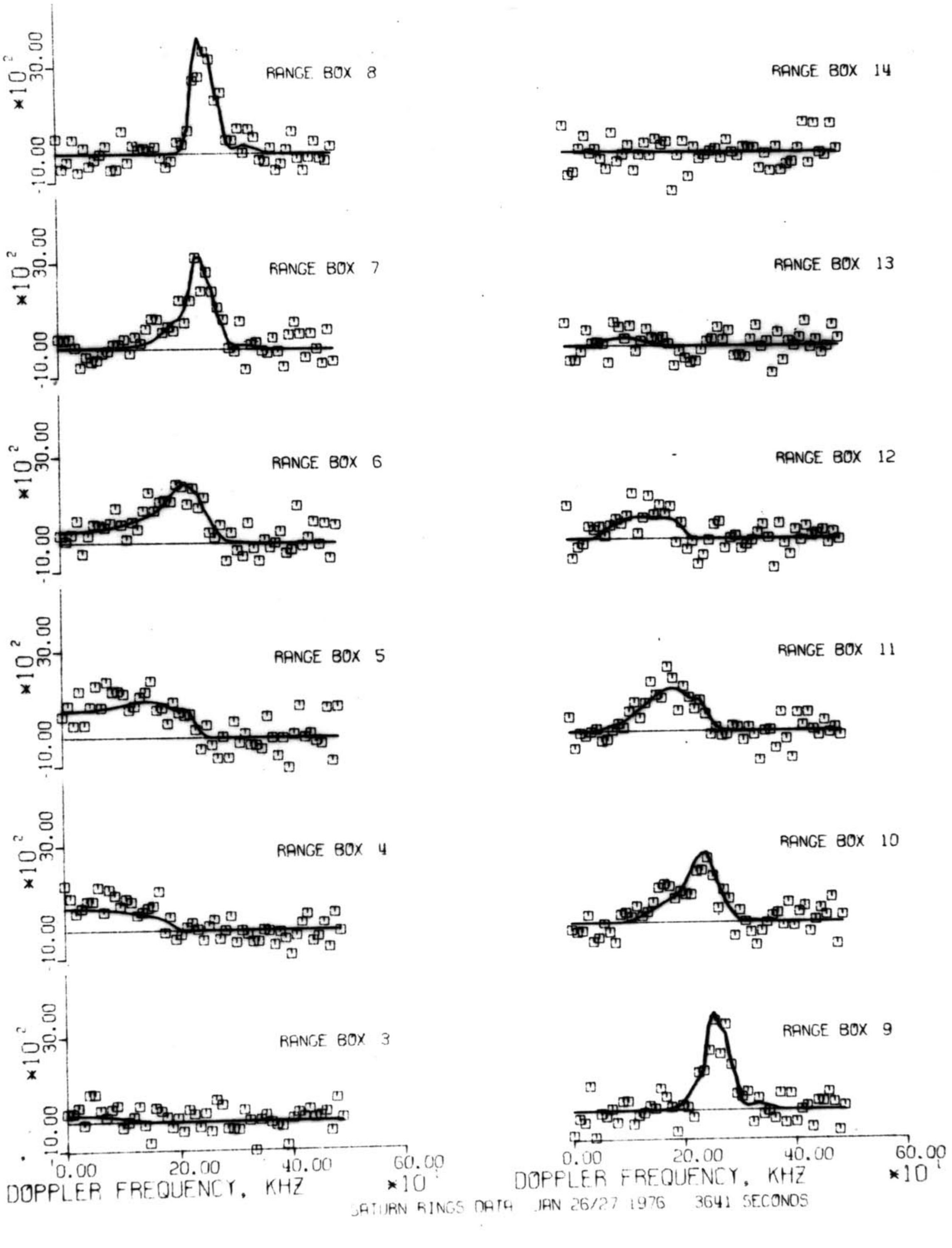

SATURN RINGS DATA JAN 26/27 1976 3641 SECONDS

Fig. 22b

III. C. The 1977-1978 circularly polarized observations: Measurement of μ_C and α at 12.6-cm wavelength

Plans to repeat the 1976 delay-Doppler experiment on January 1977 were ruined by transmitter problems, although several nights did become available two months after opposition in late March. Unfortunately, the echo strength was too low for the delay-Doppler data to be useful. The weakness of the echo was surprising, even after accounting for the effects of greater distance and the degradation (for this experiment!) associated with the use of a new feed. As we shall see later, this reduction may be associated with a smaller ring-opening angle in 1977 ($|B| = 18.2°$) than in 1976 ($|B| = 21.4°$).

On the third available night in 1977 (April 1), the same circular-polarization-switching, frequency-switching CW technique as had been used for observing the Galilean satellites in 1976 (Section II. B) was employed to determine μ_C and α for Saturn's rings. The 12.6-cm circular polarization ratio had been shown to be greater than unity for the outer three (icy) Galilean satellites, and about unity at 3.5-cm wavelength for Saturn's rings, which were also known to contain water ice. Since the rings' opening angle would close down rapidly from $|B| \approx 21°$ in 1976 to $|B| \approx 0°$ in 1980, it was felt that albedo measurements made during this period might prove useful in the estimation of ring-plane thickness. This matter will be discussed later.

The same polarization-and-frequency-switching observing technique was used exclusively when Saturn next reached opposition in February 1978. The rings, which had closed down to $|B| = 11.7°$ by then, were observed monostatically from Arecibo on six consecutive nights from 17-22 February. The data-taking configuration employed the digital autocorrelator in the three-level by three-level oversampled mode (Appendix B) to enhance signal-to-noise ratio. A total of 29 three-minute-integrated spectra were obtained in each rotational sense of circular polarization. For the 1977 and 1978 observations, thermal noise was the major source of error in the cross section measurements and, as described in Appendix B, has determined the weight to be applied to individual determinations of σ_{SC} and σ_{OC} in calculating their average values.

System characteristics, observational parameters, and primary quantitative results (including μ_C and α) for 1977 and 1978 are given in Table X. Spectra for 1977 and 1978 are shown in Figs. 23a-d.

The circular polarization ratio corresponding to a wavelength of 12.6 cm is only about 0.5 [as compared to the value of unity reported by Goldstein et al. (1977) at $\lambda = 3.5$ cm] for these observations. The geometric albedo at this wavelength corresponding to a weighted mean value for $|B|$ of 13° is only about 75% as large as α at 3.5 cm and $|B| = 21.4°$.

TABLE X. Saturn's rings 1977 and 1978 radar results, observational parameters and system characteristics.

		1 Apr 77	Feb 78
B		-18.19°	-11.70°
sin |B|		0.31	0.20
Proj. area (A,B rings), 10^{15} m^2		7.791	4.925
Round trip echo delay		$02^h23^m28^s$	$02^h17^m04^s$
Mean time of reception, UTC		01^h53^m	05^h30^m
Integration time	"SC"	756 s	4824 s
	"OC"	810 s	4743 s
	"TC"	1566 s	9567 s
System temperature	"SC"	78.4 K	67.1 K
	"OC"	78.7 K	74.0 K
	Ave.	78.6 K	70.7 K
Transmitted power		340 kw	303 kw
One-way antenna gain		68.9 dB	68.7 dB
Zenith angle of Saturn at transit		0° 20'	4° 20'
Absolute cross section (10^{15} m^2)	σ_{OC}	4.77± 1.19	3.76±0.94
	σ_{SC}	2.73±0.68	1.49±0.37
	σ_{TC}	7.50±1.88	5.25±1.31
Normalized cross section	σ_{OC}	0.61±0.15	0.76±0.19
	σ_{SC}	0.35±0.09	0.30±0.08
	σ_{TC}	0.96±0.24	1.07±0.27
μ_C		0.57±0.12	0.40±0.05
α		0.24±0.06	0.27±0.07

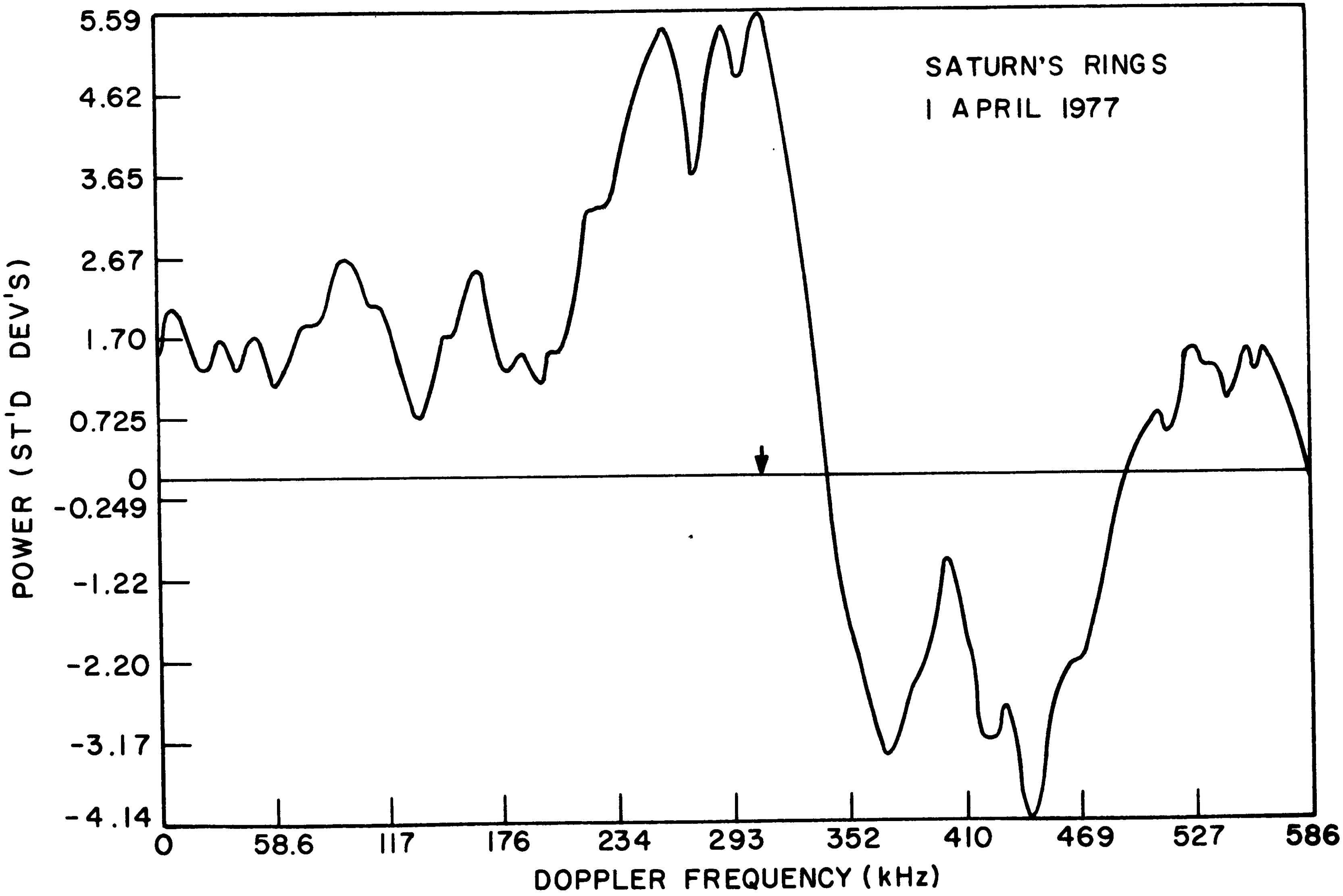

Fig. 23a. Saturn's rings "TC" spectrum from 1 April 1977, folded about zero Doppler and smoothed to 125-kHz resolution. Arrow has same meaning as in Fig. 20.

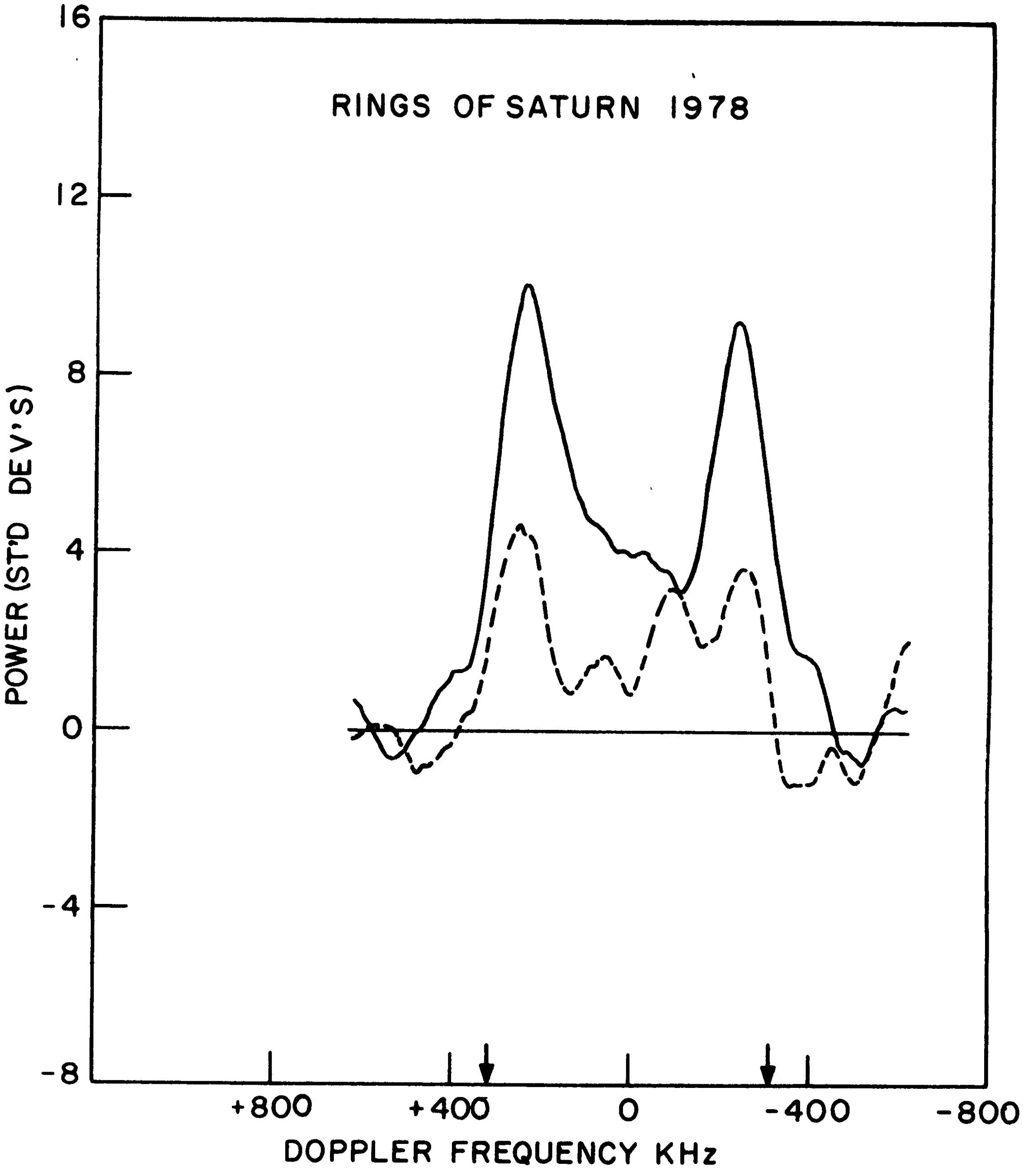

Fig. 23b. Saturn's rings 1978 spectra measured in "SC" (dashed curve) and "OC" (solid curve) polarization senses. Resolution is 100 kHz.

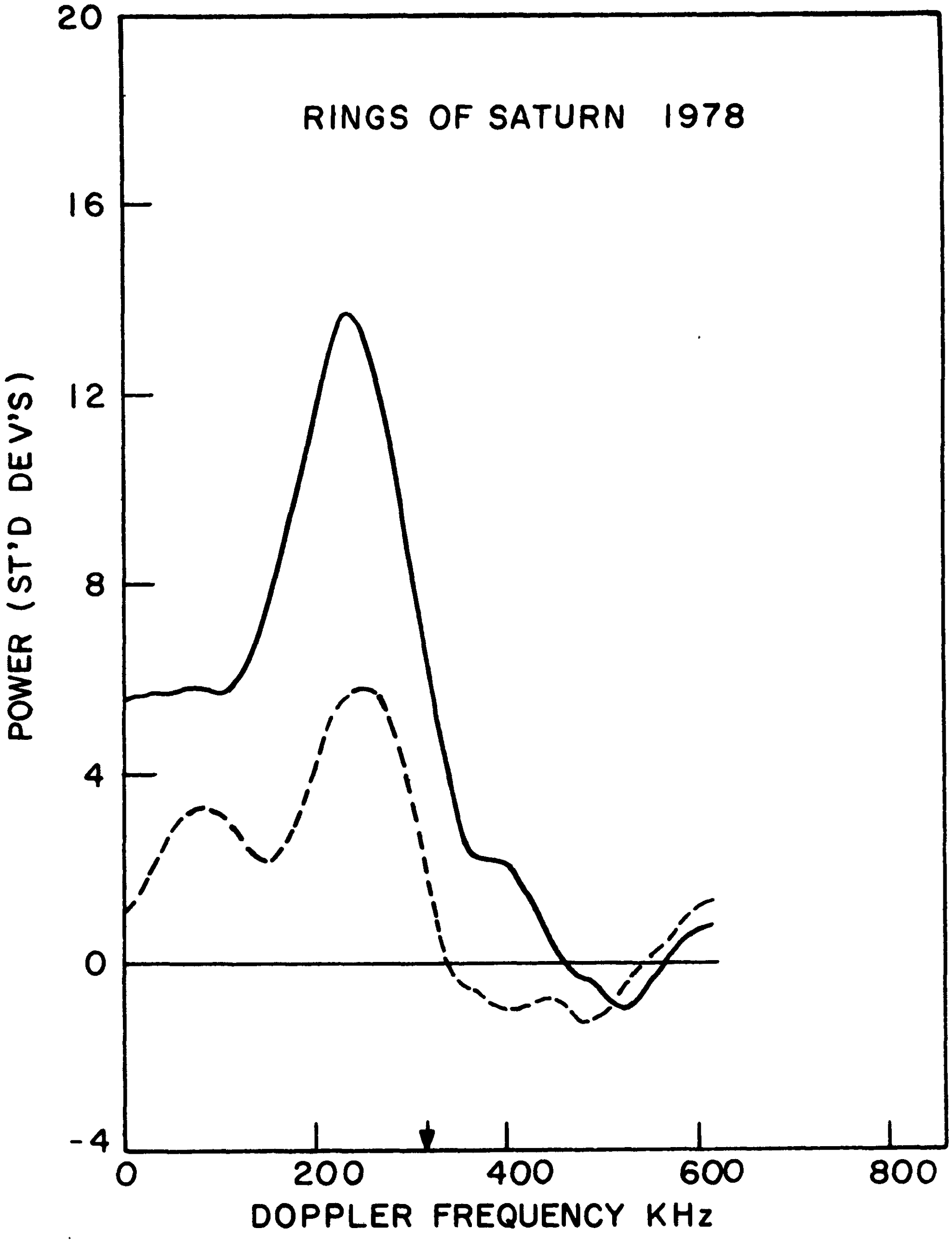

Fig. 23c. Same as Fig. 23b, but spectra have been folded about zero Doppler shift.

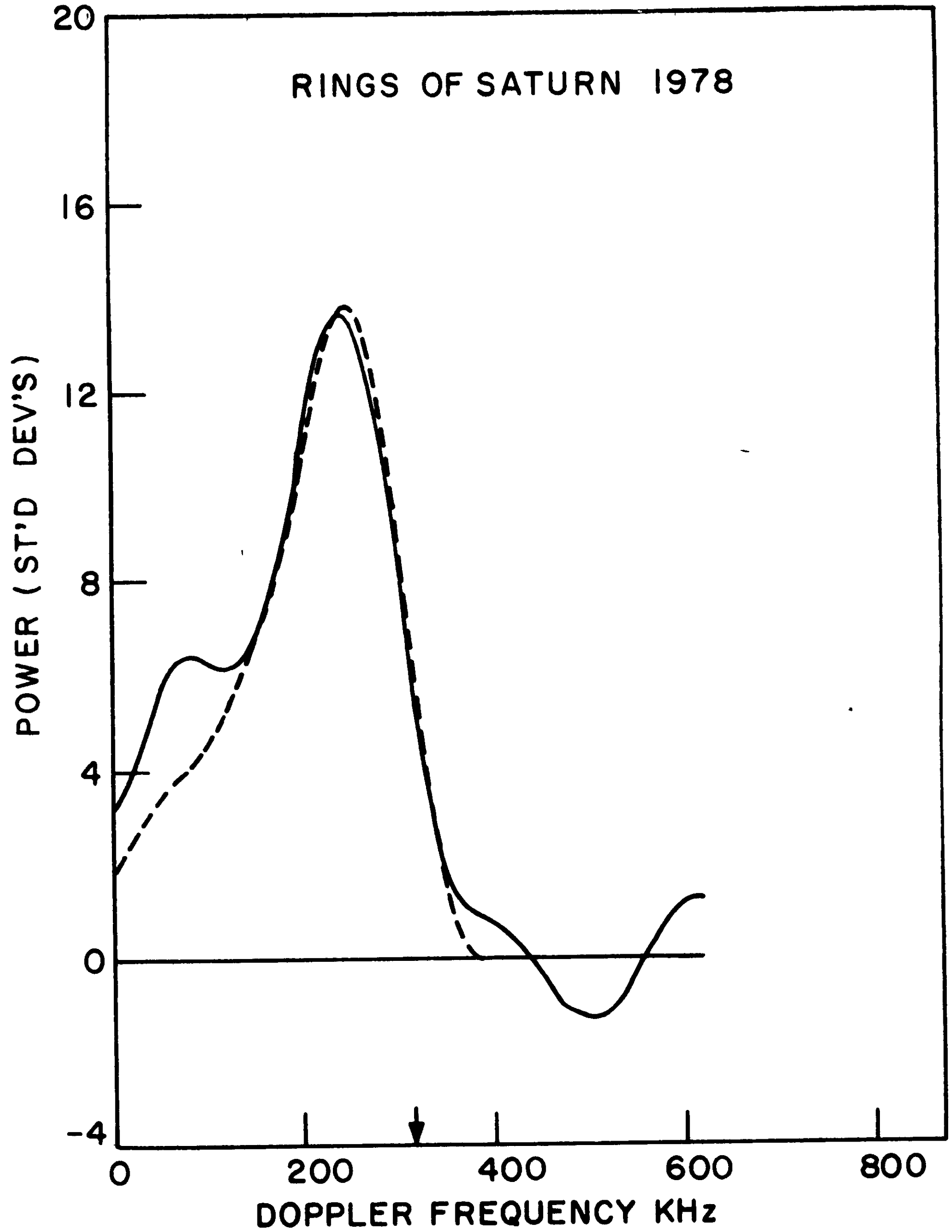

Fig. 23d. Saturn's rings 1978 folded "TC" spectrum (solid curve) is compared to the best-fit two-parameter model (dashed curve).

In the following sections of this chapter, I shall discuss particular radar properties of the rings determined from 1973 through 1978, and their possible bearing on ring structure.

III. D. Spectral symmetry

Folding Saturn's rings power spectra about zero Doppler shift relative to that corresponding to the planetary center of mass conceals any left/right (L/R) asymmetry that may exist between echoes at positive and negative relative Doppler frequencies. From the two-sided power spectra obtained from 1973 through 1978, there do not appear to be L/R asymmetries which cannot be explained as arising from plausible pointing* uncertainties and statistical fluctuations in the signal and/or associated noise.

For the 1976 delay-Doppler data, one would expect L/R asymmetries caused by tracking errors to be correlated at all delays. Since the moment of the power distribution about zero Doppler shift varies noticeably with delay (Fig. 19), the ratio x_i of power in the left (positive Doppler) half of the echo spectrum to power in the right (negative Doppler) half is not observed to be constant at all range boxes $\underline{i}$. Figure 24 compares these power ratios to their mean $\bar{x}$ and normalizes them to the rms fluctuation σ about that mean for a six-run sum of the 1976 data. Range boxes numbers 3 and 14 contain little signal and were not used in the calculation of $\bar{x}$ or σ. Smoothing over about half a range box is implicit in Fig. 24 due to scatter in $\hat{\tau}$ among the six data sets.

---

*The Arecibo pointing uncertainty at the time of the observations was ~0.3'. The one-way full beamwidth at half power is ~2'. (Saturn's rings subtend slightly less than 1' in their largest dimension.)

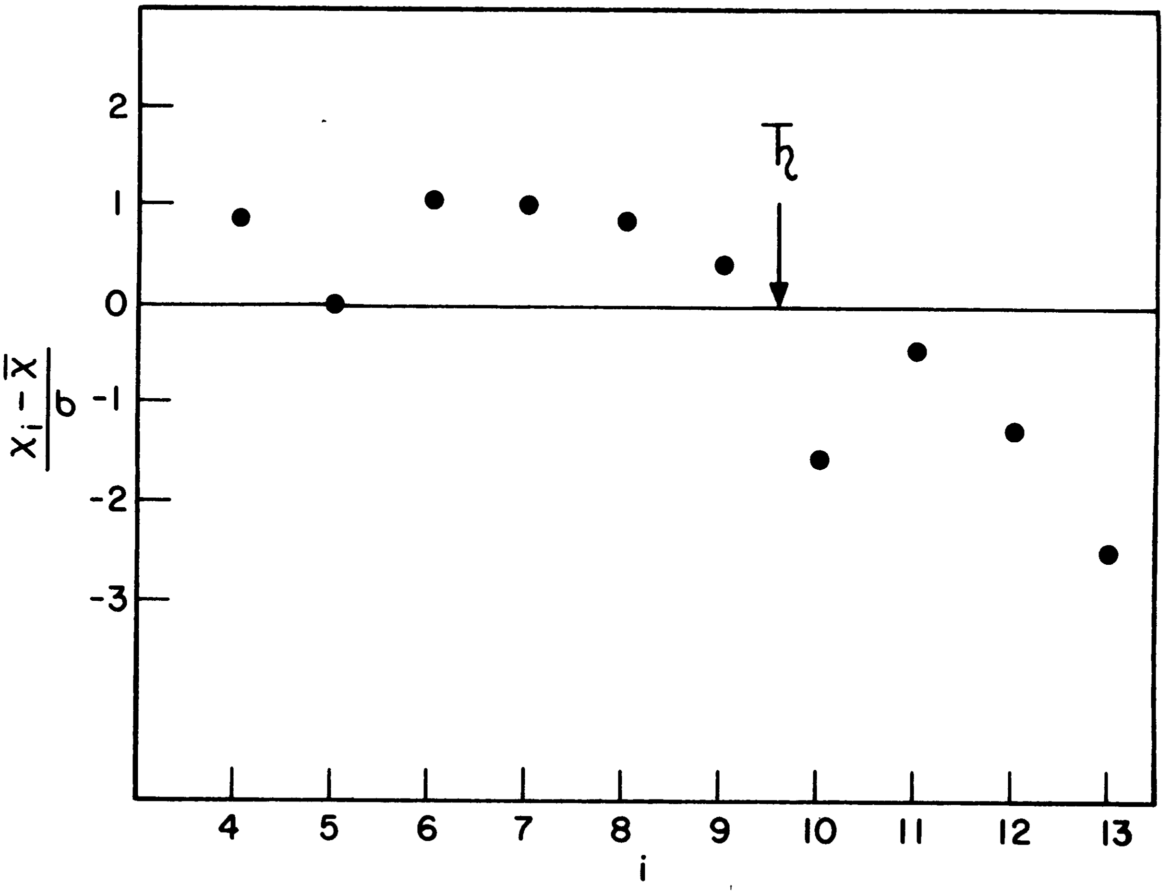

Fig. 24. Saturn's rings "L/R" power ratio (see text) for the 1976 delay-Doppler data. This ratio (x_i) is plotted relative to the average ($\bar{x}$) and normalized to the rms fluctuation σ about that mean, for range boxes (i) numbers 4 through 13. The average position of Saturn in delay is indicated.

The total spread in x_i is only about three standard deviations, certainly of marginal statistical significance. The slope of the apparent, nearly linear correlation among the x_i could be due to azimuthally asymmetric scattering from the rings. Such asymmetry, if physically significant, would require the quadrants centered on $\Phi = 135^\circ$ and $\Phi = 315^\circ$ to be more efficient scatterers than the opposite quadrants. (Here, orbital phase Φ is measured in the same manner as for the Galilean satellites.) This is consistent with visible-wavelength azimuthal brightness variations in ring A (Lumme and Irvine, 1976; Reitsema et al., 1976), as well as the L/R asymmetries marginally suggested in the radar data. Azimuthal variations in B-ring visible-wavelength brightness have been reported (Ferrin, 1974), but unlike the A-ring variations, these can be accounted for as a result of instrumental smearing (Reitsema, et al., 1976) .

Since the antenna gain pattern is the same for either rotational sense of circular polarization, μ_C should be independent of tracking error. Although this is strictly valid only for a truly simultaneous two-channel experiment, it should largely hold for the February 1978 measurement of circular polarization ratio by virtue of the rapidity of polarization switching and the consequent averaging of a large number of single-polarization cross section measurements.

To investigate the possibility of L/R differences in μ_C, the 1978 radar cross sections shown in Table X were recalculated as described in Section III. C, except that the spectra were split into left and right sections along the central Doppler-frequency axis. Treating the rings as two separate targets, weighted mean values of σ_{OC}, σ_{SC}, σ_{TC} and μ_C were calculated. This will be referred to as analysis "B" to distinguish the results from those of analysis "A" reported in Table X. In a third set of calculations (analysis "C"), the rings were split into three targets, corresponding to left, central, and right spectral bands. Results of analyses "A", "B" and "C" are presented in Table XI.

Analysis "B" indicates no significant L/R asymmetry in cross section or polarization ratio. The same conclusion holds for L/R asymmetry in analysis "C". The central spectral section apparently has a slightly lower μ_C than either the left or right section. However, the maximum deviation of the "L", "C" and "R" values of μ_C from the overall ("Σ") average value of μ_C is only ~1 σ, probably not physically significant.

In summary, observations from 1973 to 1978 show no evidence for an intrinsic L/R asymmetry in scattering from Saturn's rings. Although azimuthal variations in radar reflectivity similar to those reported at visible wavelengths might explain the apparent correlation of L/R ratio with delay seen in the 1976 data, errors in antenna tracking may be a more likely, if less intriguing, explanation. I conclude that the statistical accuracy of the existing data is too low to infer the presence of any L/R asymmetry in the intensity or polarization state of the radar echo from Saturn's rings.

TABLE XI. Saturn's rings 1978 analyses of spectral symmetry. Absolute radar cross sections, in units of $10^{15} m^2$, and μ_C are presented for three separate analyses of received power spectra. Analysis (A) results were given in Table X. Analysis (B) splits the rings into two separate targets at the zero Doppler-frequency data point. Analysis (C) divides the rings into three spectral regions: "L", "C" AND "R", occupying 20%, 60%, and 20% of the left-to-right spectral analyzing bandwidth, respectively. The central (C) section is approximately delineated by the line-of-sight tangent to the inner edge of the B ring and nearly fills the "front" quadrant of orbital phase, from $\Phi = 135^\circ$ to $\Phi = 225^\circ$ (Fig. 19). Hence this "C" section excludes the spectral "wings" which originate from the east and west ansae.

	(A)	(B)		(C)		
POL'N	Σ	L	R	L	C	R
SC	1.49±0.17	0.76±0.12	0.73±0.12	0.53±0.08	0.53±0.13	0.43±0.08
OC	3.76±0.19	2.05±0.13	1.71±0.13	1.09±0.08	1.70±0.14	0.97±0.08
TC	5.25±0.25	2.81±0.18	2.44±0.18	1.62±0.11	2.23±0.16	1.40±0.11
μ_C	0.40±0.05	0.37±0.06	0.43±0.08	0.49±0.08	0.31±0.08	0.44±0.08

III. E. Spectral shape and the low-Doppler excess

Spectra obtained at $|B| = 26.4°$ and at $|B| = 24.4°$ showed significant "excess" power at low Doppler shifts relative to a model having an A:B-ring reflectivity ratio of 0.5. Although the 1976 delay-Doppler results suggest a ratio nearer unity, the gross spectral shape is not very sensitive to this parameter, so the physical reality of the LDE at high values of $|B|$ is not put in question by changes in A:B relative scattering efficiencies.

Surprisingly, there is no evidence, at a statistically meaningful level, for an LDE in the 1976-1978 spectra (Figs. 20 and 23) obtained at smaller values of $|B|$. Even if the noise "bumps" in the folded 1978 "OC" and 1976 "SL" spectra actually result from excess signal at low Doppler shifts, the LDE has certainly decreased considerably since 1975. That the "bumps" in the 1976 spectra are indeed due to noise fluctuation is suggested by the fine agreement of spectra in individual range boxes with the best-fit model (Fig. 22)

If the pre-1976 LDE's were caused by any of the three mechanisms suggested by Goldstein and Morris (1973) or Goldstein _et al_. (1977), their sudden disappearance (or, at least, severe decrease) could not be explained in terms of the relatively small decreases in $|B|$. (I ignore the possibility of extreme time-variability of _intrinsic_ radar properties, which might result from such exotic phenomena as hail storms in Saturn's upper atmosphere.)

A fourth possible explanation (Franklin and Colombo, 1978) involves a clustering in the particle size distribution produced by self gravitation between neighboring particles. Their theory predicts that the effective particle cross section is increased when the particles are moving nearly across the line of sight and decreased when moving along it. This process, which depends on azimuthally variable particle alignments, would be more noticeable in an optically thin ring than in an optically thick one, and it probably would not hold for ring B. It might hold for ring A, but perhaps only above some minimum value of $|B|$, to ensure that the line-of-sight optical depth not be too large. Franklin and Colombo note that the magnitude of the LDE predicted by their model is considerably less than that observed. On the other hand, their model appears to explain the azimuthal brightness variations observed at visible wavelengths (Section III. D). It may be very difficult for Franklin and Colombo to reconcile, in a single model, the decrease in the radar LDE with the simultaneous increase in the optical azimuthal asymmetries reported by Lumme *et al*. (1977).

An attractive feature of the Franklin-Colombo theory is that it could potentially explain the LDE *without* invoking particles beyond the visible ring boundaries. Another explanation (Ostro, 1976) which also avoids this problem postulates large, synchronously rotating particles with azimuthally anisotropic single-scattering albedos. Such anisotropy could be due to extreme variation in composition or surface roughness over the particulate surface. Unfortunately, as shown by Peale (1977), synchronous rotation would require particles hundreds of meters in dimension, low collision frequencies, and/or a non-tidal rotation-damping mechanism. Also, no physically plausible basis for longitude-dependent particle reflectivity is apparent.

Suppose that the LDE is an A-ring phenomenon, Then its sudden demise near $|B| \approx 22°$ could be related to the occultation by Saturn of the far side of that ring. As shown in Table XII, the rear quadrant ($-45° \leqslant \Phi \leqslant 45°$) of the A ring was occulted to a considerably greater degree at $|B| = 21.4°$ than at $|B| = 24.4°$. This is especially true for the outer parts of the A ring. From $|B| = 24.4°$ to $|B| = 21.4°$, the visible fraction of the A1 ringlet's rear quadrant dropped from 92% to 72%. Thus, this part of the ring system might be responsible for the LDE, and changing ring geometry might explain its sudden decrease.

TABLE XII. Visible fractions of ringlets for various values of the opening angle |B|. Also given are values corresponding to the "rear quadrants" of the A1 and A2 ringlets (see text). The "minimum unshadowed ρ" is the minimum distance, in units of Saturn radii, of an unshadowed ringlet.

	|B|				
Ringlet	26.4	24.4	21.4	18.19	11.70
B3	.84	.83	.82	.81	.79
B2	.87	.86	.84	.83	.81
B1	.91	.89	.87	.85	.83
A2	.99	.94	.91	.88	.86
A1	1.00	.98	.93	.90	.87
B	.88	.87	.85	.84	.82
A	.99	.96	.92	.89	.86
A2 rear quad	.96	.76	.64	.52	.44
A1 rear quad	1.00	.92	.72	.60	.48
Min unshadowed ρ	2.09	2.24	2.52		

III. F. Ringlet relative reflectivities

The estimates of relative reflectivities obtained from the 1976 data analyses are presented in Fig. 21 and Table IX. Figure 21 also shows visible-wavelength estimates (Cook et al., 1973) of relative optical depth for the outer five ringlets.

The boundaries of the ringlets given by Cook et al. (1973) are nearly identical to those used here (Appendix K). The estimated relative reflectivity for the B1 ringlet is extremely high, consistent with a variety of visible-wavelength observations (Fig. 22 of Pollack, 1975). It should be noted that the correlation (Appendix E) between the estimates of the model parameters corresponding to relative reflectivities of adjacent ringlets is ~ 0.5, while other covariances are ~ 0.1. This fact supports the conclusion that the B1 region is indeed the most radar-reflective part of Saturn's rings. The A:B1 and B3:B1 reflectivity ratios appear somewhat larger at 12.6-cm wavelength than at visible wavelengths.

The estimated A:B reflectivity ratio (0.86 ± 0.06) is quite significant. Fitting a two-parameter model to the folded "TC" spectrum obtained in February 1978 results in an A:B reflectivity ratio of 1.2 ± 0.3; the "OC" spectrum alone gives 0.8 ± 0.2. As noted earlier, estimation of an A:B reflectivity ratio from power spectra is much less reliable than from the inversion of delay-Doppler data.

Nevertheless, the agreement of the 1978 result with that from 1976 is reassuring. The A:B reflectivity ratio determined here is considerably higher than 0.5, a value determined from visible-wavelength observations (Cook, et al., 1973), and assumed in the construction of the model used to compare against the $|B| = 26.4°$ radar spectrogram (Goldstein and Morris, 1973).

The geometric albedo α of the rings, in terms of the albedo α_i of the i^{th} of $\underline{N}$ ringlets, is

$$\alpha = \Sigma\, \alpha_i\, A_i \;/\; \Sigma\, A_i$$

where A_i is the visible area of the i^{th} ringlet and the summations extend from one to $\underline{N}$. The estimated relative reflectivities r_i are proportional to the albedos:

$$\alpha_i = K\, r_i$$

so

$$K = \alpha\, \Sigma\, A_i \;/\; \Sigma\, r_i\, A_i$$

For the two-parameter model, I calculate

$$K = 1.07\, \alpha$$

For $\alpha \approx 0.30$, the A- and B-ring albedos are then ≈ 0.28

and ≈ 0.32, respectively. These albedos are less than those determined for Europa and Ganymede (Table VII). As discussed by Cuzzi and Pollack (1978), the actual single-particle, single-scattering albedo required to satisfy the radar observations depends on the particle size and shape, and on whether the rings are one or many particles thick. This problem will be discussed further in Section G.

Inversion of the 1976 delay-Doppler data shows no evidence for either a C ring or an A' ring. Ferrin (1975) set an upper limit of 0.01 on the visible-wavelength optical depth τ_o of any ring external to the A ring; Smith, et al. (1975) estimated $\tau_o \sim 10^{-7}$ for this hypothetical A' ring. Cook and Franklin (1958) presented evidence that the optical depth of ring C is on the order of 0.1. Within estimated uncertainties, the radar results are consistent with these optical results.

As shown in Fig. 21, the seven-parameter estimation does suggest the presence of a radar D ring. Some suggestion of echo power at absolute Doppler shifts greater than those predicted from models having only A- and B-ring components also exists in the 1978 "OC" spectrum, but not at a highly significant level. As can be seen from its relatively small dimensions in Fig. 19, the D ring would have to be a very efficient scatterer to be radar discernible at a statistically respectable level. The published spectra for data taken prior to 1976 show no evidence for a D ring.

The D ring discovered by Guerin (1969, 1970) is apparently more tenuous than the C ring, having an estimated optical depth $\tau_o \approx 0.02$ (Ferrin, 1974). Thus, the radar sugestion of scattering from the D ring, as weak as it is, is somewhat surprising. As already pointed out, the D ring is not needed to explain the major behavior of the observed radar scattering. If a D ring exists which is relatively more reflective than the C ring at radar wavelengths, its constituent particles must be considerably larger than those in the C ring.

All factors considered, I conclude that there is only marginal evidence for the existence of a radar D ring. Indeed, the delay-Doppler radar data argue more persuasively <u>against</u> the presence of radar-reflective material in the C ring than <u>for</u> significant radar-reflective material in the D ring.

III. G. Cross sections, albedos, and polarization ratios

Table XIII summarizes all values of albedos, cross sections and polarization ratios reported to date for Saturn's rings. Ideally, one would desire values of α, μ_C and μ_L measured at 3.5-cm and 12.6-cm wavelengths for each value of $|B|$. As it stands, Table XIII is only one-third complete for 12.6-cm data, nearly empty for 3.5-cm data, and replete with apparent discrepancies. For instance, $\mu_C = 1.00 \pm 0.25$ at 3.5 cm and $|B| = 24.4^\circ$, but at 12.6 cm we have $\mu_C = 0.57 \pm 0.12$ at $|B| = 18.2^\circ$ and $\mu_C = 0.40 \pm 0.05$ at $|B| = 11.7^\circ$. To accept these data as reliable, one must conclude either that μ_C is wavelength dependent, or that μ_C decreases as the ring opening angle closes down, or both.

Consider for a moment the three S-band measurements of polarization ratios in Table XIII. If the rings' polarization properties were essentially independent of $|B|$, μ_C would appear to be only 50% as large as μ_L. I claim that this is very unlikely. Although both μ_C and μ_L must approach unity in the limit of complete randomization of the transmitted wave, such as might be produced by some high-order multiple scattering process, μ_L is less than μ_C for all theoretical models of radar backscattering with which I am familiar. Furthermore, I know of no radar experiment resulting in $\mu_L > \mu_C$. Although I will not attempt to prove that μ_L cannot exceed μ_C, this contention stands as a reasonable assumption in lieu of any evidence to the contrary.

TABLE XIII. Saturn's rings normalized cross sections, geometric albedos and polarization ratios reported to date.

Authors	|B|	λ	Pol'n	σ	μ	α
Goldstein and Morris (1973)	26.4°	12.6 cm	OC	0.68±0.17		
Goldstein *et al.* (1977)	24.4°	12.6 cm	TL		μ_L=1.0 ±0.3	
		3.5 cm	OC	0.68±0.13		
			SC	0.68±0.13		
			TC		μ_C=1.00±0.25	0.34±0.06
Pettengill *et al.* (1979)	21.4°	12.6 cm	SL	0.83±0.21		
Ostro and Pettengill (1979)	18.2°	12.6 cm	OC	0.61±0.15		
			SC	0.35±0.09		
			TC		μ_C=0.57±0.12	0.24±0.06
Ostro and Pettengill (1979)	11.7°	12.6 cm	OC	0.76±0.19		
			SC	0.30±0.08		
			TC		μ_C=0.40±0.05	0.27±0.07

Suppose that at $|B| = 26.4°$, $\mu_C \approx \mu_L \approx 1$. This would imply that $\sigma_{SC} \approx 0.68$ at that opening angle. In this case, one would be forced to conclude that as the rings closed down from $|B| = 26.4°$ to $|B| = 11.7°$, σ_{SC} plunged from ≈ 0.68 to ≈ 0.30 while σ_{OC} remained nearly constant. This result would be extremely difficult to explain. Although the rings' polarization properties certainly may vary with tilt angle, it seems more reasonable to assume that <u>both</u> μ_C and μ_L are considerably less than unity at $|B| \approx 25°$, in conflict with the value of μ_L reported by Goldstein <u>et al</u>. (1977). Measurement of μ_L using a bistatic radar configuration requires extreme care with respect to the determination of polarization position angles. Of all the entries in Table XIII, I feel that the value reported for μ_L is probably the least reliable, while the 1978 measurement of μ_C is probably the most reliable. From the arguments stated here, it seems reasonable to assume that $\mu_L \approx 0.4$ for $|B| = 24.4°$.

Unfortunately, several recent articles (e.g., Cuzzi and Pollack, 1978), attempting to explain the rings' radar properties in terms of their adduced physical structure, have heavily stressed the single determination of μ_L by Goldstein <u>et al</u>. (1977). My personal conviction is that the dependence of albedo and polarization on tilt angle has yet to be elucidated. Nevertheless, certain constraints may be placed on the rings' structure on the basis of information in Table XIII.

The value of μ_C (0.40 ± 0.05) measured by Ostro and Pettengill (1979) at S-band rules out ring models predicting either a highly polarized echo ($\mu_C \approx 0$) or a highly depolarized echo ($\mu_C \approx 1$) at 12.6-cm wavelength. The net polarization state of the radar echo will depend on the polarization of single-particle-scattered radiation and the relative importance of single and multiple scattering.

Any multiply externally scattered component should be highly depolarized ($\mu_C \approx \mu_L \approx 1$). Liou and Schotland (1971) have shown that radiation twice-scattered by spheres is about 80% depolarized. One would expect a distribution of irregular particles to be even more efficient at depolarization. Hence the measurements of μ_C by Ostro and Pettengill (1979) indicate the importance of single-particle backscattering in the 12.6-cm radar echo from Saturn's rings.

Single-particle-scattering polarization properties are poorly known (Cuzzi and Pollack, 1978). Empirical studies (Sassen, 1974; Zerull, 1974, 1976; McNeill and Carswell, 1975) indicate that $0.3 \lesssim \mu_L \lesssim 0.5$ for irregular particles with circumferences $\sim 10\ \lambda$, corresponding to radii ~ 20 cm at S-band. Schotland et al. (1971) have shown that the depolarization observed from large, irregular particles tends to increase with the size of the particle. Multiple internal reflections could produce $\mu_L \approx 1$ for scattering from very large (radius $\gg$ 1 m at S-band) particles (Cuzzi and Pollack, 1978). However, the precise nature of the irregularities is not discussed on the literature, and the dependence of depolarization on the scale of the irregularities has yet to be investigated. On the other hand, the backscattered radiation from small (radius $\lesssim \lambda$) particles or smooth spheres of any size is known to be completely polarized ($\mu_C = \mu_L = 0$), as noted in Chapter II.

The radar echo from a monolayer would be almost entirely due to single-particle backscattering. Whereas a monolayer of large, irregular particles could easily yield $\mu_C \approx 0.4$, ring models postulating a monolayer of large, smooth spheres can be ruled out. At the other extreme, the echo from an extended layer of particles would presumably contain an appreciable multiply scattered component having $\mu_C \approx 1$. In this case, the portion of the echo resulting from single-particle backscattering would have to be highly polarized, and the large, smooth, transparent, ice spheres proposed by Pettengill and Hagfors (1974) would appear more attractive than very irregular particles.

As shown in Table XIII, the albedos and circular polarization ratios are apparently larger at $\lambda = 3.5$ cm and $|B| = 24.4°$ than at $\lambda = 12.6$ cm and $|B| \lesssim 18°$. If this result is significant, the complication of wavelength- and/or $|B|$-dependence must be added to the already difficult problem of interpretation of the rings' radar behavior.

As noted at the beginning of this section, measured values of σ_{OC} at S-band have remained nearly constant (within the estimated uncertainties) in the interval $11.7° \leqslant |B| \leqslant 26.4°$. One would expect the normalized cross section of a monolayer of particles to increase with decreasing $|B|$, i.e., as the fraction of projected ring area filled with particles increased. On the other hand, the reflectivity of an optically thick extended layer would be expected to remain nearly constant. Unfortunately, it is impossible to distinguish reliably between these two "canonical" types of ring models on the basis of existing data.

Cuzzi and Pollack (1978) have shown that extremely large (radius $\gg$ 1 m) particles composed of ice or metal or any other very low-loss or highly conducting material, in either a monolayer or an extended layer, would exhibit a much sharper rise in reflectivity with decreasing $|B|$ than has been observed from 1973 to 1978. This class of ring models is therefore ruled out by the radar results.

III. H. The structure of Saturn's rings: Conclusions

The optically defined A and B rings are apparently responsible for most of the radar echo. The outer half of the B ring (next to the Cassini Division) is significantly more reflective than the A ring or the inner half of the B ring. The average A-ring backscattering efficiency is nearly (~ 90%) as large as that of the B ring at the radar wavelengths used. The apparent difference in the A:B reflectivity ratio at radar and visible wavelengths may be evidence for major structural differences between these rings. The C ring has an extremely low radar reflectivity, and there is only marginal evidence for a radar D ring.

The rings' 12.6-cm normalized value for σ_{OC} has remained nearly constant at 0.7 ± 0.1 for $11.7° \leqslant |B| \leqslant 26.4°$. Although the 12.6-cm geometric albedo α has been directly <u>measured</u> for only two values of $|B|$ (11.7° and 18.2°), one may infer that the albedo also remains nearly invariant at 0.3 ± 0.1 over the wider interval $11.7° \leqslant |B| \leqslant 26.4°$.

Although one might conclude that μ_C and α depend on $|B|$, it seems more likely that these quantities are wavelength-dependent, being slightly larger at 3.5 cm than 12.6 cm.

The S-band measurements of μ_C constitute evidence for single scattering in the 12.6-cm radar echo. They can be interpreted in terms of <u>either</u> a monolayer of large (radius $\gtrsim \lambda$) irregular particles <u>or</u> an extended layer of particles with very low single-scattering polarization ratios.

As pointed out by Cuzzi and Pollack (1978), the monolayer and extended-layer models of ring structure are the canonical extremes of a continuum of possible ring states. The currently available radar measurements of albedo could conceivably be consistent with the type of $|B|$-dependence expected for either of these two canonical extremes. However, the 1973-1978 measurements of radar cross section do not show the sharp rise with decreasing $|B|$ which is predicted (Cuzzi and Pollack, 1978) for models postulating large ($\gg 1$ m) metallic particles.

I can offer no physically plausible explanation for the strong LDE observed at S-band with $|B| = 26.4°$ and at X-band with $|B| = 24.4°$. The apparent sudden decrease in the LDE for $|B| \leqslant 21.4°$ rules out source mechanisms involving echoes from particles in an A' ring, particles orbiting at high inclinations to Saturn's equatorial plane, or particles permanently entrained in Saturn's upper atmosphere and corotating with the planet. On the other hand, the demise of the LDE for $|B| \leqslant 21.4°$ might be due to changing ring geometry. In this case, the rear quadrant of the outer half of the A ring is likely to be the source of the LDE.

IV. FINAL REMARKS AND SUGGESTIONS FOR FUTURE WORK

Many properties of the Galilean satellite surfaces and Saturn's rings, and their possible interpretations, have been discussed in this dissertation. The most significant conclusions involve constraints based on measurements of the circular polarization ratio μ_C. Values of μ_C appreciably greater than unity, determined in 1976-1977 for Europa, Ganymede and Callisto, apparently demand the dominance of a double-reflection backscatter process on these bodies. The icy-crater model satisfies this requirement and can account for all other observed radar-scattering properties of the outer three satellites. In the case of Saturn's rings, values of μ_C observed for intermediate opening angles are much lower than unity, suggesting the importance of single-particle backscattering in the 12.6-cm radar echo.

The development of useful theoretical ring models is contingent on the acquisition of a larger body of reliable radar data than currently exists. The degree of wavelength dependence in the rings' radar properties must be elucidated by S- and X-band observations at particular ring opening angles. In a similar vein, a thorough empirical investigation of the radar polarization properties of irregular particles is sorely needed.

Future discrimination among competing ring models will require the accurate determination of geometric albedo and both polarization ratios at widely separated values of the ring opening angle. The Earth is shortly to pass through the ring plane; thus the 1979 apparition, with $|B| \approx 6°$, will be an opportune time to continue radar study of the rings. The determination of μ_L should certainly be attempted. Estimates of α, μ_C and μ_L could be improved substantially by simultaneous reception of the echo in orthogonal polarization senses. (Such a two-channel experiment, employing a pair of low-noise maser front-end amplifiers, may soon be possible at Arecibo.)

The linear polarization ratio has been measured for the Galilean satellites on only one occasion (Europa, on Dec. 7, 1976). The possibility that μ_L may share the correlation among μ_C, α, $\underline{p}$ and frost coverage should be investigated.

For Europa, Ganymede and Callisto, there are large ranges of orbital phase ($\Delta\Phi > 100°$) over which the radar geometric albedo is unknown. The orbital phase coverage of radar observations must be extended in order to elucidate the shape of the radar "lightcurves" as well as the dependence, if any, of other properties on Φ.

Calculations indicate that delay resolution of echoes from Ganymede and Callisto should be possible at Arecibo. Such observations may shed light on the locations and dimensions of regions possessing anomalous radar scattering. If sufficient sensitivity could be achieved, measurement of the delay distribution of the Ganymede echo in "OC" and "SC" polarization senses would provide a critical test of the icy-crater theory: μ_C is expected to decrease with delay for those delays corresponding to oblique angles of incidence.

As noted earlier, there is much room for further theoretical development of the icy-crater model presented here. Formulation of a rigorous physical-optics treatment of scattering from hemispherical craters would be a particularly useful and challenging endeavor.

V. APPENDICES

APPENDIX A. Radar equation and associated definitions*

The (monostatic) radar equation is

$$P_R = \left(\frac{P_T G}{4\pi R^2}\right)\left(\frac{\sigma}{4\pi}\right)\left(\frac{A_e}{R^2}\right) = \frac{P_T G^2 \lambda^2 \sigma}{(4\pi)^3 R^4} \tag{A1}$$

where

P_R = received power (w)

P_T = transmitted power (w)

G = one-way effective antenna gain = $\sqrt{G_r G_t}$, where (r,t) = (receive, transmit)

R = target distance (m)

A_e = antenna effective aperture area (m^2) = $G\lambda^2/4\pi$ (Kraus, 1966)

σ = radar cross section (m^2)

λ = wavelength (m)

The first term in brackets gives flux incident on the target (S_i, watts per m^2 wavefront), and the last term is the effective capture solid angle of the receiving antenna as seen from the target. The middle term is clearly backscattered power per steradian (i.e., angular power density) for unit incident flux at the target. That is, σ is the total power per unit incident flux which would be scattered if the reflected power density were isotropic and equalled that observed by the radar.

The specific radar cross section, or angular scattering

---

*Much of the material in this appendix can be found in Evans and Hagfors (1968); some is due to Pettengill (private communication, 1976).

law, is defined as

$$\sigma_o(\theta) = \frac{d\sigma}{dA} = \text{radar cross section per unit contributing target surface element} \tag{A2}$$

and is a dimensionless function of the angle of incidence, θ, on the target surface.

Since there are sec θ m^2 target per m^2 wavefront, the target "brightness" is

$$B(\theta)\frac{\text{w rad}^{-2}}{m^2\ \text{wavefront}} = S_i\ \frac{1}{4\pi}\ \sigma_o(\theta)\frac{\text{w rad}^{-2}\ \text{per unit } S_i}{m^2\ \text{target}}\sec\theta \tag{A3}$$

Hence, radar scattering laws contain an extra cos θ factor when compared to their optical equivalents.

If one knows $\sigma_o(\theta)$, it is trivial to find σ for a spherical target:

$$\sigma = \int_{\text{hemisphere}} \sigma_o dA = \int_0^a dx\ \sigma_o(\theta)\,2\pi x\ \sec\theta\ dx$$

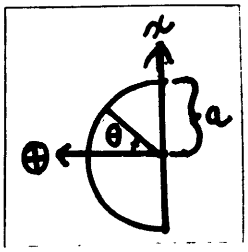

$$= 2\pi a^2 \int_0^{\pi/2} \sigma_o(\theta)\ \sin\theta\ d\theta \tag{A4}$$

If one knows the bistatic scattering law $\sigma_o(\theta,\theta',\phi)$, where the exit direction is described by the polar angle θ', and the azimuthal angle, ϕ, with respect to the incidence plane, one can calculate the total scattered power

$$P_{TOT} = S_i \int_{\text{surface}} dA \int_{2\pi} d\Omega \frac{\sigma_o(\theta,\theta',\phi)}{4\pi}$$

$$= S_i\ 2\pi a^2 \int_0^{\pi/2} d\theta \sin\theta \int_{2\pi} d\Omega \sigma_o(\theta,\theta',\phi) \qquad \text{(A5)}$$

Each "dA" scatters into a hemisphere of 2π steradians:

$$\int_{2\pi} d\Omega \rightarrow \int_0^{2\pi} d\phi \int_0^{\pi/2} d\theta' \sin\theta' \qquad \text{(A6)}$$

so

$$P_{TOT} = \frac{2\pi a^2}{4} S_i \int_0^{\pi/2} d\theta \int_0^{\pi/2} d\theta' \int_0^{2\pi} d\phi\ \sigma_o(\theta,\theta',\phi) \sin\theta \sin\theta' \qquad \text{(A7)}$$

Since σ_o is referenced to unit incidence flux by definition, and the total incident power is $\pi a^2 S_i$ watts for incident flux S_i, the Bond albedo is

$$A_B = \frac{P_{TOT}}{\pi a^2 S_i} \qquad \text{(A8)}$$

One can define the target gain G:

$$G = \frac{4\pi \cdot \text{reflected power density per unit incident flux} \cdot S_i}{\text{total reflected power}}$$

$$= \frac{\sigma S_i}{P_{TOT}} \qquad \text{(A9)}$$

Thus one also has

$$\frac{\sigma}{\pi a^2} = A_B G \tag{A10}$$

Geometric albedo

Geometric albedo is defined as the target brightness normalized to that of a perfectly diffusing ($A_B = 1$) Lambert disc normal to the line of sight ($\theta = \theta' = 0$), with an area equal to the projected area of the target, and located at the same distance as the target. "Lambert" means that the scattering law has the form

$$\sigma_0(\theta,\theta') = A_B g \cos\theta \cos\theta' \tag{A11}$$

i.e., scattering is azimuthally isotropic. The value of g is found by calculating the total power scattered by this hypothetical Lambert disc. From Eqn. (A5),

$$P_{TOT} = \int_{\text{surface}} dA \int_{2\pi} d\Omega \left. \frac{\sigma_0(\theta,\theta')}{4\pi} \right|_{\theta=0}$$

$$= (\pi a^2) 2\pi \int_0^{\pi/2} d\theta' \frac{A_B g \cos\theta' \sin\theta'}{4\pi}$$

$$= \frac{\pi a^2}{2} A_B g \left. \frac{\sin\theta'}{2} \right|_0^{\pi/2} = \frac{\pi a^2 A_B g}{4} \tag{A12}$$

Now, $A_B = 1$ and the total scattered power for unit incident flux is πa^2. Thus $P_{TOT} = \pi a^2 = \pi a^2 g/4$ and $g = 4$. Therefore

$\sigma_0(\theta,\theta') = 4 \cos\theta \cos\theta'$ for the standard disc. For backscatter, $\theta = \theta' = 0$ so $\sigma_0 = 4$. In other words, the standard disc with a geometric albedo of unity has a cross section per unit surface area equal to 4. The surface area of the standard disc used for comparison with any given target will be the target's projected area A_p, so the geometric albedo p is

$$p = \frac{\sigma}{4A_p} \tag{A13}$$

When the radar- and visible-wavelength geometric albedos need to be distinguished, the symbol α will represent the former and p will represent the latter.

It is convenient to reduce the bistatic scattering law to a monostatic scattering law:

$$\theta_0(\theta') = A_B g \cos\theta \cos^{n-1}\theta'\Big|_{\theta=\theta'} = A_B g \cos^{n}\theta' \tag{A14}$$

Then, for unit incident flux per unit surface area,

$$\int_{2\pi} d\Omega \left.\frac{\sigma_0(\theta,\theta')}{4\pi}\right|_{\theta=0} = 1$$

$$\int_{2\pi} d\Omega g \cos\theta \cos^{n-1}\theta'\Big|_{\theta=0} = 4\pi$$

$$2\pi g \int_0^{\pi/2} d\theta' \cos^{n-1}\theta' \sin\theta' = 4\pi$$

$$\left.\frac{-\cos^n \theta'}{n}\right|_0^{\pi/2} = 4\pi/(2\pi g) \qquad \text{(A15)}$$

so $g = 2n$ and $\sigma_0(\theta') = A_B(2n) \cos^n \theta'$.

For a sphere,

$$\sigma = 2\pi a^2 \int_0^{\pi/2} \sigma_0(\theta') \sin \theta' \, d\theta'$$

$$\sigma = 2\pi a^2 A_B \cdot 2n \int_0^{\pi/2} \cos^n \theta' \sin \theta' \, d\theta'$$

$$\sigma = \frac{4\pi a^2 A_B n}{n+1} \qquad \text{(A16)}$$

If $n = 2$ and $A_B = 1$, as for a perfectly diffusing Lambert sphere,

$$\sigma = \frac{8}{3} \pi a^2, \text{ Lambert sphere.} \qquad \text{(A17)}$$

Since $\sigma = 4p\pi a^2$ by definition of σ and p,

$$(n+1)p = nA_B \qquad \text{(A18)}$$

Thus, the monostatic specific radar cross section can be written

$$\theta_0(\theta') = 2p(n+1) \cos^n \theta' \qquad \text{(A19)}$$

From the definition of G, it follows that $G = 4n/(n+1)$; hence

$G = 8/3$ for $n = 2$.

I have $\sigma/(\pi a^2) = 4p = A_B G$. Optical astronomers [see Allen (1973), p. 142; or Kaula (1968), p. 259] use the relation $A_B = pq$ where their "phase integral" $q = 4/G$. Setting $A_B = 1$, I can construct the following table.

TABLE XIV. Constants applicable to common scattering laws.

Target	p	q	$G = \frac{\sigma}{\pi a^2}$	n(equivalent for sphere)
Lambert disc	1	1	4	--
Lambert sphere	2/3	3/2	8/3	2
uniformly bright sphere	1/2	2	2	1
isotropic scatterer (metallic-reflection sphere)	1/4	4	1	--

It is important to note that $G=4n/(n+1)$ is not applicable in the case of the isotropic scatterer. For such a specular reflector, the initial generalization of a $\cos^n \theta'$ law from a $\cos\theta \cos^{n-1}\theta'$ law is physically misleading because the bistatic law implies azimuthally isotropic scattering, while $\sigma_0(\theta,\theta')$ for specular reflectors is zero except for $\theta' = -\theta$, in the plane of incidence only. The use of a monostatic $\cos^n \theta$ law certainly lacks physical justification if $n \gg 1$ describes the surface in question. As long as this fact is kept in mind, it is acceptable to use the parameter n as an empirical descriptor of data. Similarly, $n < 1$ implies $\sigma_0(\theta,\theta') \to \infty$ at $\theta' = \pi/2$, again independent of azimuth, so, again, assumption of the bistatic law is physically unsound.

Nevertheless, as pointed out by Jurgens and Bender (1977), backscattering laws of the type $\cos^n \theta$ are extremely useful for detection modeling.

APPENDIX B. Arecibo S-band radar system and data-taking procedures

1. System characteristics

Figure 25 is a simplified radar receiver block diagram. Not shown are components involved in frequency synthesis from the site time base, system temperature calibration, or monitoring of system total-power response.

Figure 26 shows one-way antenna gain as a function of zenith angle for the "flat feed" used for the January 1976 Saturn's rings observations, and the newer "circular feed" used for all other observations. The curves were determined by D.B. Campbell of NAIC and are based on calibration observations of several well-studied radio sources.

Receiver system temperature T_s varies from less than 40 K (cold sky at zenith) to well over 100 K for the circular feed at zenith angles larger than 20^o. Jupiter adds about 30 K. Thus T_s must be measured frequently during any observation, generally by coupling a calibrated noise source into the receiver and monitoring the accompanying increase in IF rms voltage.

Calibration of the secondary temperature standards and transmitter power monitors is carried out regularly by Arecibo Observatory technical staff.

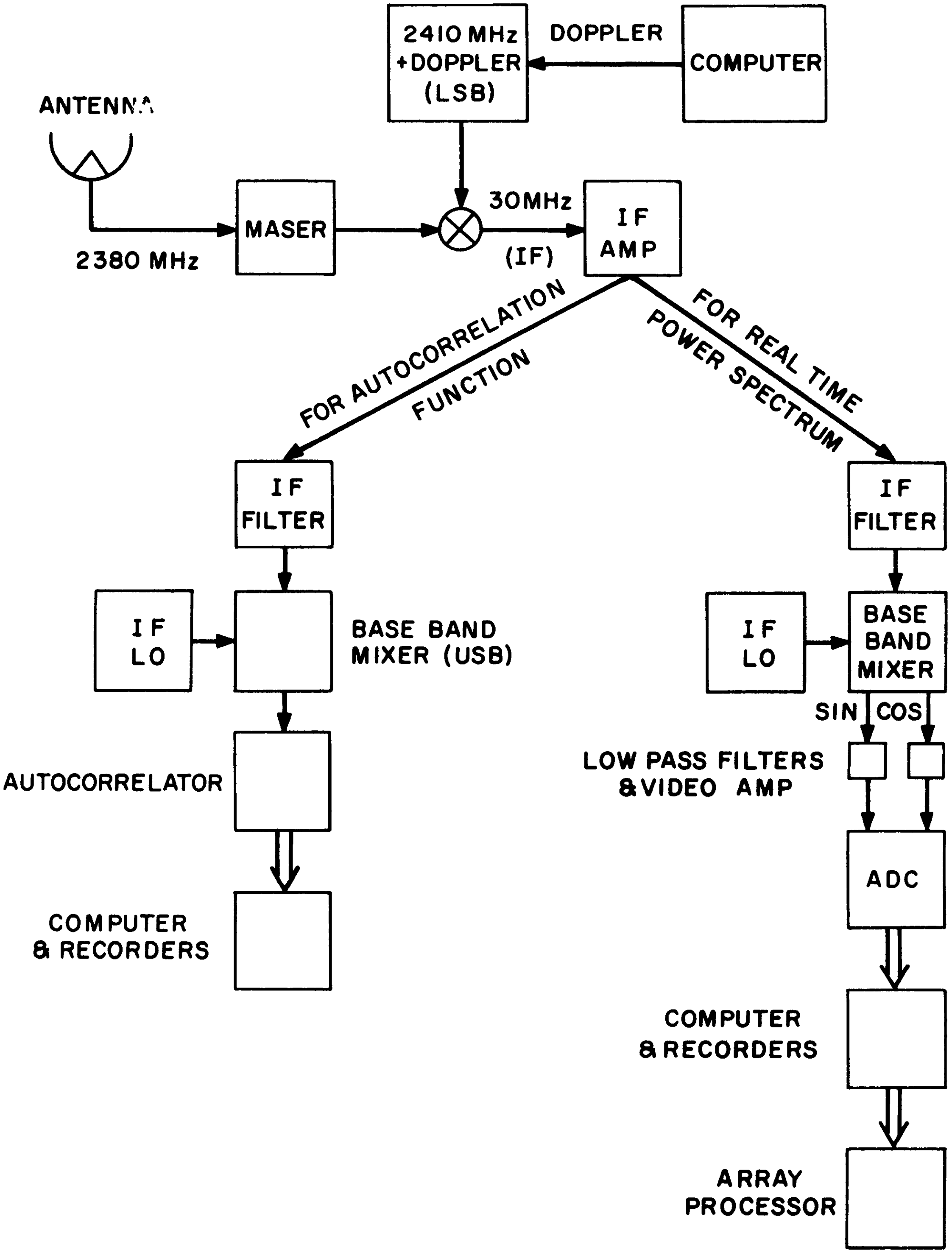

Fig. 25. Simplified block diagram of Arecibo S-band radar receiver. Here, LSB (or USB) denotes lower (or upper) side band selection.

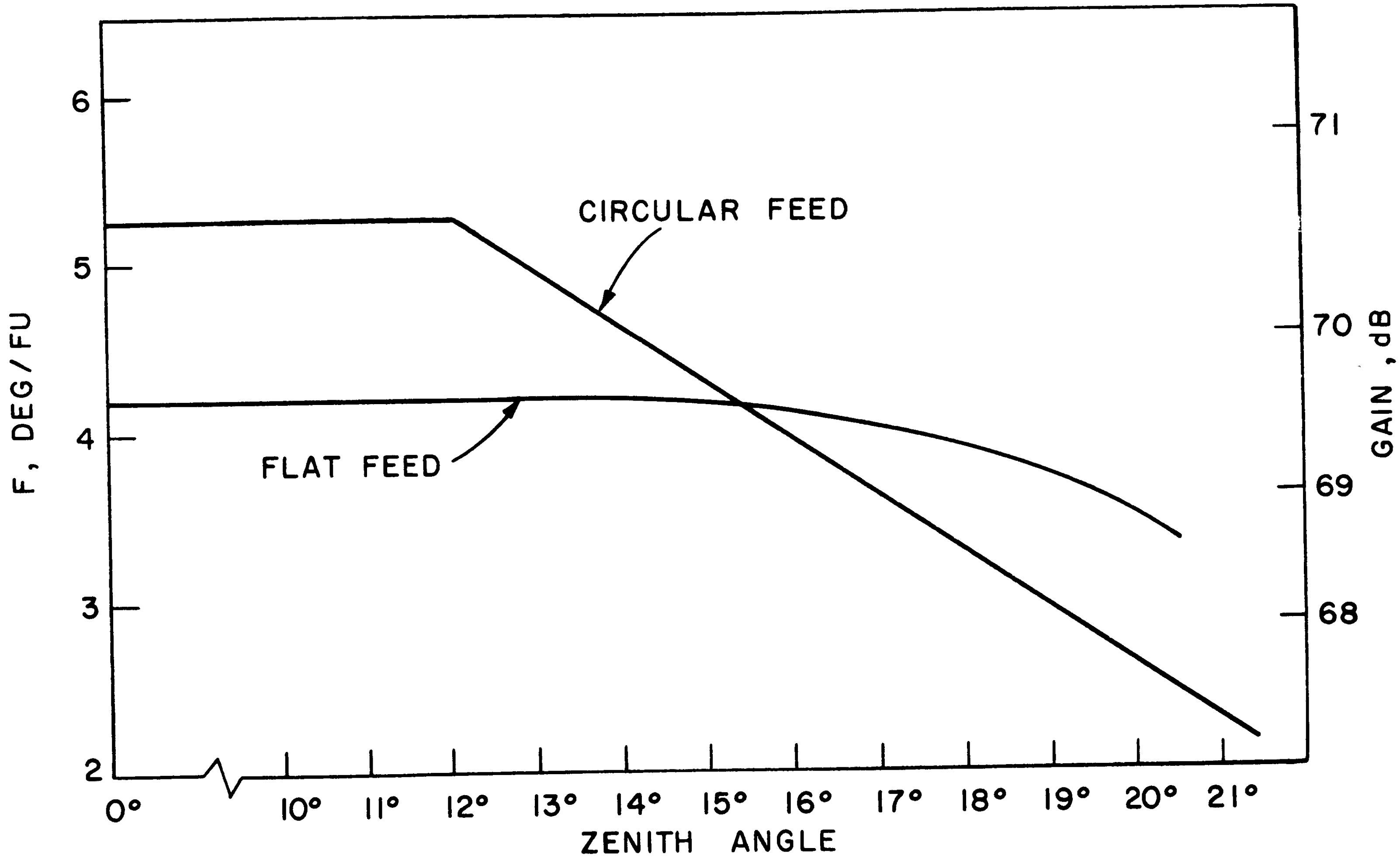

Fig. 26. Arecibo antenna gain calibration curves. The one-way gain is shown for both the old and the new 2380 MHz feeds used during 1976-1978, in units of degrees of antenna temperature increase per source flux unit, as well as in dB. The gain is given by $8\pi \underline{k}\lambda^{-2} \times 10^{26}\ \underline{F}$ (Kraus, 1968, p. 99), where $\underline{F}$ is the antenna response measured in degrees per flux unit, $\underline{k}$ is Boltzmann's constant, and λ is the wavelength (12.6 cm).

2. Procedures for obtaining power spectra

The raw data for all observations except the 1977 Galilean satellites (which employed a digital array processor for real-time calculation of power spectra) were obtained from a 1008-channel digital autocorrelation spectrum analyzer (DASA) working in the three-level by three-level mode. The true multibit autocorrelation function $\rho(t)$ is calculated from the three-level by three-level approximation $r_3(t)$ and then Fourier transformed. Whereas the one-bit, or hard-clipped, autocorrelation function $r_1(t)$ is related to $\rho(t)$ by the Van Vleck equation $r_1(t) = (2/\pi)\sin^{-1}\rho(t)$, Hagen and Farley (1973) have shown that

$$r_3(t) = \frac{1}{\pi}\int_0^{\rho(t)} \frac{1}{\sqrt{1-x^2}}\left[e^{-K^2/(1+x)} + e^{-K^2/(1-x)}\right]dx \qquad \text{(B1)}$$

where K is the ratio of clipping level v_o to rms signal voltage σ. The sampled signal voltage v is digitized as follows:

$$\underline{v} \rightarrow \begin{cases} 1, & v > v_o \\ 0, & -v_o \leqslant v \leqslant v_o \\ -1, & v < -v_o \end{cases} \qquad \text{(B2)}$$

Conklin (1976) has numerically integrated this expression, solved for ρ, and fitted the results with a third-degree polynomial in r_3, where each coefficient of r_3 is itself a third-degree polynomial in $\underline{K}$. This leads to the following straightforward algorithm for extraction of $\rho(t)$ from $r_3(t)$.

$$\rho(t) = a + b\underset{\sim}{r}(t) + c\underset{\sim}{r}^2(t) + d\underset{\sim}{r}^3(t)$$

where

$$\begin{aligned} \underset{\sim}{r}(t) &= [r_3(t) - 9765.6]/[r_3(0) - 9765.6] \\ a &= 0.0001 - 0.0009x + 0.0002x^2 + 0.0020x^3 \\ b &= 1.5477 - 1.0409x + 0.9464x^2 - 0.1398x^3 \\ c &= -0.0460 + 0.2701x - 0.8462x^2 + 0.8753x^3 \\ d &= -0.4365 + 0.1308x + 1.8450x^2 - 1.9708x^3 \end{aligned} \tag{B3}$$

where

$$x = 1.6209 - 2.2157\left[\frac{r_3(0)}{9765.6} - 1\right] + 0.6466\left[\frac{r_3(0)}{9765.6} - 1\right]^2$$

With $r_3(t)$ representing the "raw" correlation data set, the integration time required to obtain the same statistical accuracy as would result after unit integration time if $\rho(t)$ were the raw data set is larger by a factor of 1.51. If the sampling rate were twice the Nyquist rate, or four times the bandwidth (as in the case of the 1978 Saturn's rings observations), the factor drops to 1.26. The corresponding factors for hard clipping are 2.46 and 1.82, for Nyquist and twice-Nyquist sampling, respectively. As discussed by Hagen and Farley, oversampling recovers some of the information lost in the quantization, or clipping, process.

Operation in the three-level by three-level mode requires constant monitoring of the rms voltage level during data-taking, but this is acceptable in view of the resulting improvement (about 2 dB, as compared to hard clipping) in the signal-to-noise ratio which results.

3. Background removal for frequency-switched spectra

The following method is used to remove the background (video-filter response) from raw spectra and to normalize the resulting signal to the mean system noise power. First, the transmitter is switched among *N* different frequencies distributed over a bandwidth smaller than that analyzed for the data. The transmitter dwells a time τ_d at each frequency. The echo spectrum is then integrated over corresponding intervals τ_d, the start of each interval being delayed by the round-trip flight time in order to maintain synchronism with the transmitted sequence. Thus, one accumulates *N* raw spectra $\tilde{f}_1, \tilde{f}_2, \ldots, \tilde{f}_N$, where the tilde denotes a vector. If $w_1, w_2, \ldots, w_N$ are weights for corresponding spectra, the background for $\tilde{f}_j$ is represented by

$$\tilde{b}_j = \frac{\sum\limits_{i \neq j} w_i \tilde{f}_i}{\sum\limits_{i \neq j} w_i} \tag{B4}$$

The background-free "signal spectra" in units of the mean noise power P_N are $\underset{\sim}{\hat{s}}_1, \underset{\sim}{\hat{s}}_2, \ldots, \underset{\sim}{\hat{s}}_N$, where

$$\underset{\sim}{\hat{s}}_j = (\underset{\sim}{f}_j - \underset{\sim}{b}_j) \;/\; \underset{\sim}{b}_j \tag{B5}$$

It is sometimes desirable to normalize the spectra to the rms fluctuations in the noise power. In practice, the total integration time τ is split equally over *N* transmitter frequencies, so the rms noise in each $\underset{\sim}{f}_j$ is

$$\sigma_f = (B\tau/N)^{-1/2} \tag{B6}$$

where *B* is the spectral resolution. The rms noise in each $\underset{\sim}{b}_j$ is

$$\sigma_b = (B\tau/N)^{-1/2}\;(N-1)^{-1/2} \tag{B7}$$

Since $\underset{\sim}{\hat{s}}_j = \underset{\sim}{f}_j - \underset{\sim}{b}_j$,

$$(\sigma_{\hat{s}})^2 = \sigma_f^2 + \sigma_b^2 = \frac{N}{B\tau} + \frac{N}{B\tau(N-1)} = \frac{N^2}{B\tau(N-1)}$$

$$= N \;/\; \sqrt{B\,\tau(N-1)} \tag{B8}$$

for all j. The final step is to add the *N*, properly shifted $\underset{\sim}{s}_j$, resulting in a further $N^{-1/2}$ reduction in the rms noise. The final power spectrum, in units of the rms fluctuations in P_N, is

$$\underset{\sim}{s} = \sum_{j=1}^{N} \hat{\underset{\sim}{s}}_j \, / \, \sigma_s \tag{B9}$$

where

$$\sigma_s = \sigma_{\hat{s}} \, / \, \sqrt{N} = \left[\frac{N}{(N-1)B\tau} \right]^{1/2} \tag{B10}$$

For a given $B\tau$ product, the noise is proportional to $\sqrt{N/(N-1)}$, which equals 1.414, 1.155, and 1.069, for N equal to 2, 4, and 8, respectively. In other words, one gains almost 1 dB in signal-to-noise ratio by switching over four frequencies instead of two, while the improvement from increasing N still further is less dramatic. These facts were first noted by Pettengill (private communication, 1977).

APPENDIX C. Error estimates for cross sections and polarization ratios

The "observable": radar cross section "x" (to avoid notational confusion later) is assumed here to be defined by the radar equation (Appendix A):

$$x = (\text{cross section})\text{m}^2 = (A\rho kT_s B)/(P_T G^2) \tag{C1}$$

where $A = (4\pi)^3 R^4 \lambda^{-2}$

$\rho = P_R/P_N$ = signal-to-noise ratio

P_R = received signal power

$P_N = kT_s B$ = system noise power

B = analyzing bandwidth

For an integration time τ, the determination of P_R is degraded by the rms fluctuation $P_N/\sqrt{B\tau}$ in system noise power. Expressed in units of radar cross section this "thermal error" is

$$(\text{thermal error})\text{m}^2 = \frac{1}{\sqrt{B\tau}} \frac{AkT_s B}{P_T G^2} = \left(\frac{AkT_s}{P_T G^2}\right)\sqrt{\frac{B}{\tau}} \tag{C2}$$

so the fractional error due to thermal noise alone for any determination of radar cross section is

$$(\text{fractional error}) = (\text{thermal error})/(\text{cross section}) = (\rho\sqrt{B\tau})^{-1} \tag{C3}$$

Calibration of $T_s/(P_T G^2)$ is accurate to no better than about 1 dB, so if the fractional error due to thermal noise fluctuations is on the order of 25% or larger (e.g., the 1977 and 1978 Saturn's rings observations), it can be considered the major source of error. In this situation, a measurement x_i of cross section can be given a statistical weight

$$w_i = (\text{thermal error})^{-2} = \sigma_i^{-2} \tag{C4}$$

and the best estimate from statistical combination of N such measurements is

$$\hat{x} = \Sigma\, w_i x_i / \Sigma\, w_i \tag{C5}$$

with error

$$\hat{\sigma} = (\Sigma\, w_i)^{-1/2} \tag{C6}$$

where the summations are from 1 to N.

When systematic uncertainties dominate, that is, when $(\rho\sqrt{B\tau})^{-1} \ll 1$ and $\tau_i = \tau$ = constant, the best estimate of cross section is simply the mean

$$\hat{x} = \Sigma\, x_i / N \tag{C7}$$

and the statistical error is equal to the estimated rms fluctuations about that mean:

$$\hat{\sigma} = \sqrt{\frac{\Sigma (x_i - \hat{x})}{N-1}} \tag{C8}$$

If I have measured cross sections $\hat{x}_1 \pm \hat{\sigma}_1$, $\hat{x}_2 \pm \hat{\sigma}_2$ in two polarizations using rapid polarization switching, estimation of the ratio $\mu = x_1/x_2$ should be immune to the effects of systematic uncertainties so the maximum error in the estimate of μ is (Bevington, 1969, p. 56)

$$\sigma_\mu = \mu \sqrt{\left(\frac{\hat{\sigma}_1}{\hat{x}_1}\right)^2 + \left(\frac{\hat{\sigma}_2}{\hat{x}_2}\right)^2} \tag{C9}$$

However, the reported error in a single-polarization cross section is always assigned a minimum value equal to $\hat{x}/4$ to reflect estimated systematic uncertainties. Similarly, an estimate of total cross section $\hat{x}_T = \hat{x}_1 + \hat{x}_2$ is assigned an uncertainty equal to

$$\sigma_T = \max \begin{cases} \hat{x}_T/4 \\ \sqrt{\hat{\sigma}_1^2 + \hat{\sigma}_2^2} \end{cases} \tag{C10}$$

The lower expression, which applies for large $(\rho\sqrt{B\tau})^{-1}$, is simply the root-sum-square of the errors in the two single-polarization estimates (Bevington, p. 59); it assumes that the statistical fluctuations in $\hat{x}_1$ and $\hat{x}_2$ are uncorrelated.

APPENDIX D. Distribution of echo power in delay and Doppler for a sphere with a $\cos^n\theta$ scattering law *

Delay

The monostatic scattering law for a sphere can sometimes be represented by the form [see Appendix A, esp. Eqn. (G12)]

$$\sigma_0(\theta) = 2\alpha(n+1)\cos^n\theta \tag{D1}$$

where the geometric albedo α is defined in Appendix A, and θ is the angle of incidence of the radar line of sight to the normal of a given surface element. Figure 27a is a side view of the visible hemisphere of a spherical target with radius a with the delay coordinate τ shown increasing from zero at the subradar point, in the direction away from the radar. The figure illustrates that $\theta(\tau) = \cos^{-1}(1-\frac{c\tau}{2a})$ and that the area of a "range ring" resolved by a pulse of length $\Delta\tau$ is equal to $\pi ac\Delta\tau$, independent of τ. (In the figure c is the speed of light.)

As described in Appendix A, the radar cross section per unit delay interval is

$$\sigma(\tau) = \sigma_0(\tau)\cdot\text{area} = 2\alpha(n+1)\cos^n[\theta(t)]\cdot\pi ac$$

$$= 2\pi ac\alpha(n+1)(1-\frac{c\tau}{2a})^n \tag{D2}$$

or, normalized to the sphere's cross-sectional (projected)

---

*Much of this appendix is due to Pettengill (private communication, 1976).

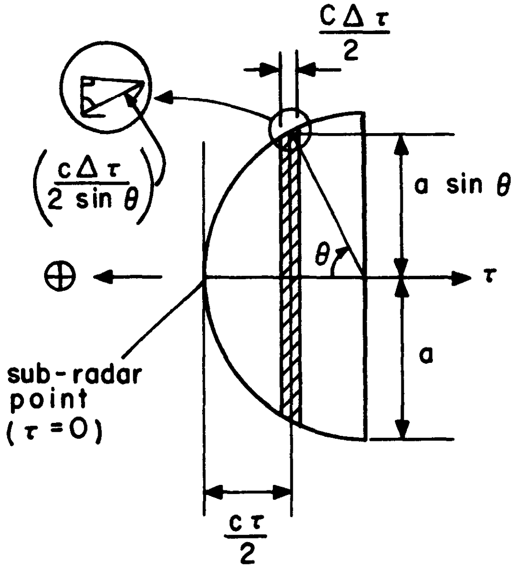

$$\cos\theta = \frac{(a - \frac{c\tau}{2})}{a} = 1 - \frac{c\tau}{2a}$$

area of cross hatched "range ring" is $[2\pi\ a \sin\theta][c\Delta\tau/(2\sin\theta)] = \pi a c \Delta\tau$

SIDE VIEW OF VISIBLE HEMISPHERE OF TARGET

Fig. 27a

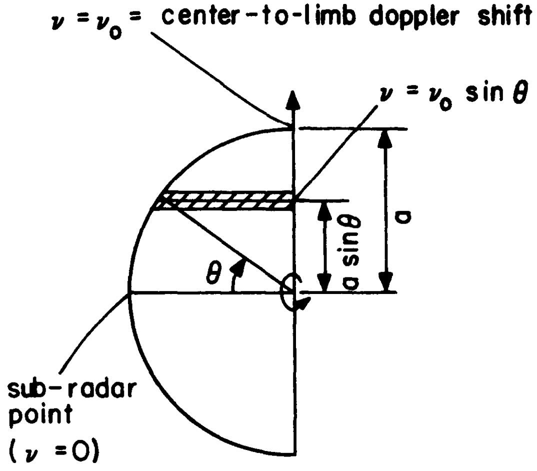

TOP VIEW OF VISIBLE HEMISPHERE OF TARGET

Fig. 27b

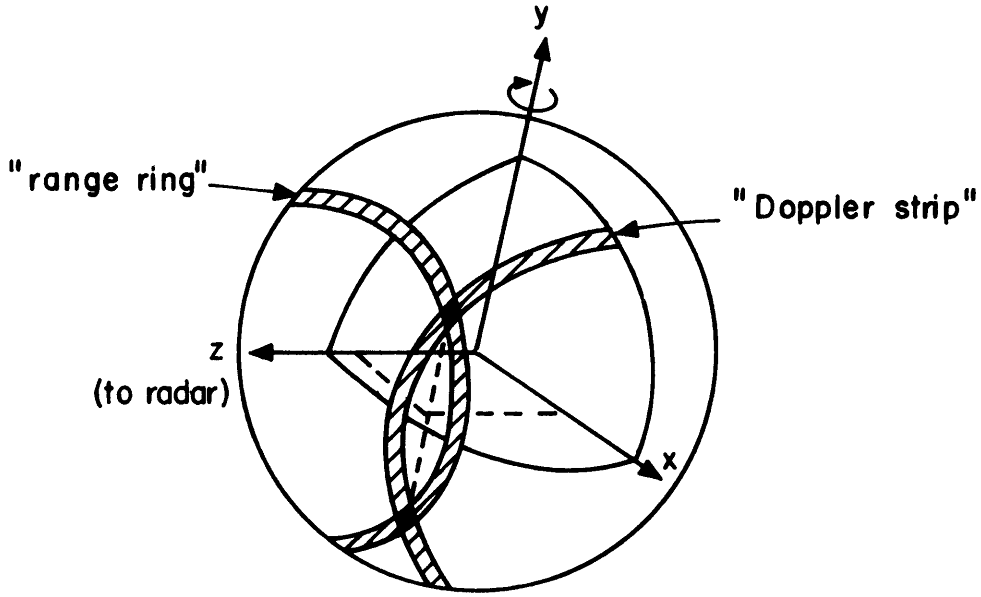

COORDINATE SYSTEM FOR
DERIVATION OF σ (ν)

Fig. 27c

area,

$$\sigma(\tau) = \frac{2c\alpha}{a}(n+1)(1-\frac{c\tau}{2a})^n \qquad (D3)$$

Doppler

The Doppler shift of the echo from a surface element with line-of-sight velocity $v_{\parallel} << c$ relative to the radar is simply $\nu = 2v_{\parallel} f/c$, where f is the transmitted carrier frequency. It is convenient to measure Doppler shift relative to that of the subradar point. If the target's apparent rotational velocity is Ω rad sec^{-1}, the "center-to-limb" Doppler shift, i.e., the absolute value of the Doppler shift from a point on the apparent Doppler equator and at $\theta = 90°$, is given by $\nu_0 = 2af\Omega/c$. The "limb-to-limb" Doppler shift is $\underline{f}_{LL} = 2\nu_0$. As illustrated by Fig. 27b, any point in a Doppler strip a distance $\underline{a}\cdot\sin\theta$ from the plane containing both the target's apparent rotation axis and the radar will have a Doppler shift $\nu = \nu_0 \sin\theta$.

Figure 27c shows the target as a unit sphere, with the z-coordinate unit vector pointing toward the radar, and the y-direction equal to the projection of the target's rotation onto a plane perpendicular to the line of sight.

From the above discussion, I have $x = \nu/\nu_0$ and $z = 1-\frac{c\tau}{2a} = \cos\theta$ so

$$y = \sqrt{1-x^2-z^2} = \sqrt{\sin^2\theta - (\nu/\nu_0)^2} \qquad (D4)$$

The target surface area of an element defined by the delay-

Doppler interval $\Delta\tau\Delta\nu$ is $2(a\Delta x)(a\Delta z)/y$, where contributions at positive and negative values of y have been included. The radar cross section of this element is thus

$$\sigma(\tau,\nu)\Delta\nu\Delta\tau = \sigma_0(\theta) \cdot 2(a\Delta x)(a\Delta z)y^{-1}$$

$$= \sigma_0(\theta) \cdot 2(a\frac{\Delta\nu}{\nu_0})(\frac{c\Delta\tau}{2})[\sin^2\theta - (\frac{\nu}{\nu_0})^2]^{-1/2}$$

$$= \sigma_0(\theta)\frac{c^2}{2f\Omega}[\sin^2\theta - (\frac{\nu}{\nu_0})^2]^{-1/2}\ \Delta\tau \qquad \text{(D5)}$$

Since $d\tau/d\theta = (2a \sin\theta)/c$,

$$\sigma(\theta,\nu)d\theta = \sigma_0(\theta)\ \frac{ac}{f\Omega}\ [\sin^2\theta - (\frac{\nu}{\nu_0})^2]^{-1/2}\ \sin\theta \qquad \text{(D6)}$$

The radar cross section per unit frequency interval for an <u>entire</u> Doppler strip is

$$\sigma(\nu) = \int_{\theta_{min}}^{\pi/2} \sigma_0(\theta,\nu)d\theta \qquad \text{(D7)}$$

where $\cos^2\theta_{min} = 1 - (\frac{\nu}{\nu_0})^2$. Substituting the scattering law,

$$\sigma(\nu) = \frac{ac}{f\Omega} \cdot 2\alpha(n+1) \int_{\pi/2}^{\theta_{min}} \cos^n\theta(\cos^2\theta_{min}-\cos^2\theta)^{-1/2}d(\cos\theta) \qquad \text{(D8)}$$

Letting $x = \cos\theta$ and $u = \cos\theta_{min}$, and using $\nu_0 = 2af\Omega/c$,

$$\sigma(\nu) = \frac{4a^2\alpha(n+1)}{\nu_0} \int_0^u \frac{x^n dx}{(u^2-x^2)^{1/2}} \tag{D9}$$

The CRC Handbook of Tables for Mathematics (Weast and Selby, 1975, p. 592) evaluates this definite integral. I find

$$\sigma(\nu) = \frac{4a^2\alpha(n+1)}{\nu_0} \frac{\sqrt{\pi}}{2} \frac{\Gamma(\frac{n+1}{2})}{\Gamma(\frac{n+2}{2})} u^n \tag{D10}$$

The relation $\Gamma(n+1) = n\Gamma(n)$ leads to $\Gamma(\frac{n+1}{2}) = \Gamma(\frac{n+3}{2})/(\frac{n+1}{2})$ so

$$\sigma(\nu) = \frac{4a^2\alpha\sqrt{\pi}}{\nu_0} \frac{\Gamma(\frac{n+3}{2})}{\Gamma(\frac{n+2}{2})} [1-(\frac{\nu}{\nu_0})^2]^{n/2} \tag{D11}$$

in agreement with Jurgens and Bender (1977) and Campbell *et al.* (1977). Figure 14 shows power spectra $\sigma(\nu)/\sigma(0)$ with $\nu_o \equiv 1$, corresponding to six values of *n*.

APPENDIX E. Least-squares parameter estimation

All my least-squares parameter estimations use the following well-known algorithm. Lower (or upper) case **boldface** denotes a vector (or matrix).

Assume that the data $\mathbf{z}$ are a function of instantaneous parameters $\mathbf{x}$ (related to $\mathbf{z}$ through a known model "H") plus Gaussian random errors $\boldsymbol{\nu}$. Let there be "d" data points and "p" parameters. I start with some *a priori* estimate of $\mathbf{x}$ called $\bar{\mathbf{x}}$ and wish to determine the best (in a least squares sense) estimate $\hat{\mathbf{x}}$. I define:

$\mathbf{A} = \left.\frac{\partial H}{\partial x}\right|_{\mathbf{x}=\bar{\mathbf{x}}}$, the d×p sensitivity matrix

$\mathbf{R} = \langle \boldsymbol{\nu}\boldsymbol{\nu}^{+} \rangle$, the d×d noise covariance matrix. This is the expectation of the product of $\boldsymbol{\nu}$ with itself, where ν_i is the Gaussian noise in the observation z_i. $\mathbf{R}^{-1}$ is the "weighting matrix". The data are sometimes normalized so that $\mathbf{R} = \mathbf{I}$, where $\mathbf{I}$ is the identity matrix.

$\mathbf{B} = \mathbf{A}^{+}\mathbf{R}^{-1}\mathbf{A}$, the p×p coefficient matrix

$\underset{\sim}{P} = \underset{\sim}{B}^{-1}$, the covariance matrix for estimation errors. The diagonal is the variance $\hat{\sigma}^2$ in $\hat{x}$.

$\underset{\sim}{r} = \underset{\sim}{z} - \underset{\sim}{\bar{z}}$, vector of pre-fit residuals

$\underset{\sim}{\hat{r}} = \underset{\sim}{z} - \underset{\sim}{\hat{z}}$, vector of post-fit residuals

$\underset{\sim}{v} = \underset{\sim}{A}^{+}\underset{\sim}{R}^{-1}\underset{\sim}{r}$, the "right-hand-side" p-vector

The best estimate of $\underset{\sim}{x}$ is $\underset{\sim}{\hat{x}} = \underset{\sim}{\bar{x}}+\underset{\sim}{P}\underset{\sim}{v}$, as can be seen from the simple case where $\underset{\sim}{R} = \underset{\sim}{I}$, as follows. Given an <u>a priori</u> model $\underset{\sim}{\bar{z}} = \underset{\sim}{A}\underset{\sim}{\bar{x}}$, so $\underset{\sim}{z} = \underset{\sim}{\bar{z}}+\underset{\sim}{r}$, I wish to find $\hat{x}$ such that the <u>scalar</u>

$$Q(\underset{\sim}{\hat{x}}) = \underset{\sim}{\hat{r}}^{+}\underset{\sim}{\hat{r}} = (\underset{\sim}{z}-\underset{\sim}{\hat{z}})^{+}(\underset{\sim}{z}-\underset{\sim}{\hat{z}}) = (\underset{\sim}{z}-\underset{\sim}{A}\underset{\sim}{\hat{x}})^{+}(\underset{\sim}{z}-\underset{\sim}{A}\underset{\sim}{\hat{x}})$$

$$= \underset{\sim}{z}^{+}\underset{\sim}{z} + \underset{\sim}{\hat{x}}^{+}\underset{\sim}{A}^{+}\underset{\sim}{A}\underset{\sim}{\hat{x}} - 2\underset{\sim}{\hat{x}}^{+}\underset{\sim}{A}^{+}\underset{\sim}{z} \qquad \text{(E1)}$$

is minimized. Setting dQ/dx = 0,

$$\underset{\sim}{A}^{+}\underset{\sim}{A}\underset{\sim}{x} = \underset{\sim}{A}^{+}\underset{\sim}{z} = \underset{\sim}{A}^{+}\underset{\sim}{\bar{z}}+\underset{\sim}{A}^{+}\underset{\sim}{r} = \underset{\sim}{A}^{+}\underset{\sim}{A}\underset{\sim}{r}+\underset{\sim}{A}^{-1}\underset{\sim}{r}$$

$$\text{(E2)}$$

$$\underset{\sim}{\hat{x}} = (\underset{\sim}{A}^{+}\underset{\sim}{A})^{-1}(\underset{\sim}{A}^{+}\underset{\sim}{A})\underset{\sim}{\bar{x}}+(\underset{\sim}{A}^{+}\underset{\sim}{A})^{-1}\underset{\sim}{A}^{+}\underset{\sim}{r} = \underset{\sim}{\bar{x}}+\underset{\sim}{P}\underset{\sim}{v}$$

If the data weighting were not uniform, $Q(\underset{\sim}{\hat{x}}) = \underset{\sim}{\hat{r}}\underset{\sim}{R}^{-1}\underset{\sim}{r}$ would have had to be minimized, giving the same result.

Partially to avoid numerical problems with matrix inversion subroutines, it is convenient to define the matrix $\underset{\sim}{\bar{B}}$ such that $\bar{B}_{ij} = B_{ij}/\sqrt{B_{ii}B_{jj}}$, then calculate $\underset{\sim}{\bar{P}} = \underset{\sim}{\bar{B}}^{-1}$ and finally $\underset{\sim}{P}$, where $P_{ij} = \bar{P}_{ij}/\ \overline{B_{ii}B_{jj}}$. The "masking factors"

M_i are given by $\sqrt{P_{ii}} = M_i \geqslant 1$ and are to be interpreted as a gauge of the "pressure" exerted by a particular parameter:

$$M_i = \frac{\text{covariance of } x_i}{\text{covariance of } x_i \text{ with } x_i \text{ the } \underline{\text{only}} \text{ parameter}} \tag{E3}$$

Convergence is assumed when $|\hat{x}_i - \bar{x}_i| < \sigma_i$ for each parameter. More than one iteration is generally necessary except when H(x) is linear.

It is customary to scale $\underset{\sim}{\sigma}$ to unity goodness-of-fit, χ, where

$$\chi^2 = \frac{\Sigma\, r_i^2/\sigma_i^2}{d-p-1} , \tag{E4}$$

in order to partially compensate for model-dependent errors.

A parameter can be constrained to its a priori value by introducing a new "pseudo-observable" equal to that parameter, and letting the noise covariance of this invented data point approach zero. In practice, one can simply add a huge number to the corresponding diagonal element of $\underset{\sim}{B}$.

APPENDIX F. Models and partial derivatives

Galilean satellites

The echo power spectral density from a rigid, rotating spherical target, derived in Appendix D, can be written

$$H(f) = AR \frac{\Gamma(\frac{n+3}{2})}{\Gamma(\frac{n+2}{2})} \left[1 - (\frac{\lambda P}{4\pi})^2 R^{-2} (f-\Delta)^2\right]^{n/2} \qquad \text{(F1)}$$

where

A is proportional to the geometric albedo of the target

R is the target radius. (For radius-constrained estimations, this is set equal to 1820, 1550, 2635, or 2500 km for Io, Europa, Ganymede, or Callisto, respectively; see text.)

λ is wavelength (0.126 m)

P is target sidereal rotation period (Allen, 1973)

f is Doppler frequency shift, Hz

Δ is the Doppler shift of the subradar point

n is the exponent in the $\cos^n \theta$ scattering law assumed in the model (Appendix H)

I wish to estimate A, R, Δ, n; partials of H(f) with respect to these parameters are

$$\frac{\partial H(f)}{\partial A} = H(f)/A \qquad \text{(F2)}$$

$$\frac{\partial H(f)}{\partial R} = H(f)\ \{R^{-1} + nR^{-3}(\frac{\lambda P}{4\pi})^2 (f-\Delta)^2 / \left[1 - (\frac{\lambda P}{4\pi})^2 R^{-2} (f-\ )^2\right]\} \qquad \text{(F3)}$$

$$\frac{\partial H(f)}{\partial \Delta} = H(f)n(\frac{\lambda P}{4\pi})^2 R^{-2} (f-\Delta) / \left[1 - (\frac{\lambda P}{4\pi})^2 R^{-2} (f-\Delta)^2\right] \qquad \text{(F4)}$$

The partial with respect to n requires more effort because of the gamma functions. The following formulas can be found in any complete handbook of mathematical functions (e.g., Abramowitz and Stegun, 1964). The function Ψ is defined as

$$\Psi(z) = \Gamma'(z)/\Gamma(z) \qquad \text{(F5)}$$

where z is real and positive. By using the asymptotic approximation

$$\psi(z) \approx \ln z - \frac{1}{2z} - \frac{1}{12z^2} + \frac{1}{120z^4} - \frac{1}{252z^6} + \ldots \qquad \text{(F6)}$$

to calculate $\psi(z+n)$, where n is large enough to give the desired precision, in conjunction with the recurrence formula

$$\psi(z) = \psi(z+n) - \sum_{i=1}^{n} \frac{1}{z-1+i} \qquad \text{(F7)}$$

it is easy to calculate $\psi(z)$ for z on the order of unity. Since gamma functions are Fortran-callable,

$$\Gamma'(z) = \Gamma(z)\psi(z) \qquad \text{(F8)}$$

Applying the chain rule

$$\frac{d}{dn}\left[\frac{\Gamma(\frac{n+3}{2})}{\Gamma(\frac{n+2}{2})}\right] = \frac{\Gamma(\frac{n+2}{2})\frac{d}{dn}\Gamma(\frac{n+3}{2}) - \Gamma(\frac{n+3}{2})\frac{d}{dn}\Gamma(\frac{n+2}{2})}{\Gamma^2(\frac{n+2}{2})}$$

$$= \frac{\Gamma(\frac{n+2}{2})\frac{1}{2}\Gamma(\frac{n+3}{2})\,\Psi(\frac{n+3}{2}) - \Gamma(\frac{n+3}{2})\frac{1}{2}\Gamma(\frac{n+2}{2})\,\Psi(\frac{n+2}{2})}{\Gamma^2(\frac{n+2}{2})}$$

$$= \frac{\Gamma(\frac{n+3}{2})}{\Gamma(\frac{n+2}{2})}\left[\psi(\frac{n+3}{2}) - \psi(\frac{n+2}{2})\right]\cdot\frac{1}{2} \qquad \text{(F9)}$$

Since $\frac{d}{dn}\, a^{n/2} = \frac{1}{2}\, a^{n/2} \ln \underline{a}$ and $H(f)$ has the form

$$H = AR\,\frac{\Gamma(\frac{n+3}{2})}{\Gamma(\frac{n+2}{2})}\,[\cdot]^{n/2} \qquad \text{(F10)}$$

it follows that

$$\frac{\partial H}{\partial n} = AR\,\frac{\Gamma(\frac{n+3}{2})}{\Gamma(\frac{n+2}{2})}\,[\cdot]^{n/2}\,(\frac{1}{2}\ln\,[\cdot])$$

$$+ AR\,\frac{\Gamma(\frac{n+3}{2})}{\Gamma(\frac{n+2}{2})}\,[\cdot]^{n/2}\,(\frac{1}{2})\,[\psi(\frac{n+3}{2}) - \psi(\frac{n+2}{2})] \qquad \text{(F11)}$$

so

$$\frac{\partial H(f)}{\partial n} = \frac{1}{2}H(f)\{\ln\,[1-(\frac{\lambda P}{4\pi})^2 R^{-2}(f-\Delta)^2] + \psi(\frac{n+3}{2}) - \psi(\frac{n+2}{2})\} \qquad \text{(F12)}$$

Saturn's rings

The Doppler frequency ν and time delay τ relative to the center of Saturn for a ring particle at radius ρ (units of Saturn radii) and orbital phase Φ are

$$\nu = \frac{2F \sin \Phi \cos B}{c}\sqrt{\frac{GM_{♄}}{\rho R_{♄}}} \qquad \text{(F13)}$$

$$\tau = \frac{2\rho R_{♄} \cos \Phi \cos B}{c} \qquad \text{(F14)}$$

where

F is carrier frequency, 2.380 E9 (mks units)

B is Saturnocentric declination of Earth

c is the velocity of light, 2.9979 E8

G is the gravitational constant, 6.6732 E-11

$M_{♄}$ is the mass of Saturn, 5.685 E26

$R_{♄}$ is Saturn's equatorial radius, 59.779 E6

Putting in the constants,

$$\nu = 400.0 \sin \Phi \cos B/\sqrt{\rho} \text{ kHz} \qquad \text{(F15)}$$

and

$$\tau = 0.40\ \rho \cos \Phi \cos B \text{ sec.} \qquad \text{(F16)}$$

The ring model used is numerical. Any given ringlet (e.g., B1) is broken into mini-rings with radial extent $\leq 0.01\ R_{♄}$, each such mini-ring consisting of about 2000 "particles" of constant geometric area, and uniformly distributed in orbital phase Φ from $\Phi = 0°$ to $\Phi = 180°$. The delay and Doppler shift of each unshadowed particle is calculated, and that particle's area is sorted into the appropriate bin in an array which is essentially an accumulator for the ringlet's delay-Doppler power distribution. (See Appendix L for the shadowing calculations.) In this manner, the quantized distribution of power in delay-Doppler space is determined for every ringlet. This distribution can, of course, be summed over delay to yield a Doppler distribution.

Let the entire distribution be the array $\underset{\sim}{P}$ with elements $P_{i,j,k}$. The indices i, j, k refer to ringlet, delay, and Doppler, and range from unity to l, m, n, respectively. If the relative scattering efficiencies, or reflectivities, used to weight the ringlet's contributions to the echo are x_i, the delay-Doppler model $\underset{\sim}{H}$ has elements

$$H_{j,k} = \sum_i x_i P_{i,j,k} \tag{F17}$$

If I am estimating x_i for a frequency spectrum, I must use

$$H_k = \sum_i x_i (\sum_j P_{i,j,k}) \tag{F18}$$

and if I want a delay distribution, I must calculate

$$H_j = \sum_i x_i (\sum_k P_{i,j,k}) \tag{F19}$$

The partial derivatives for estimation of the x_i are simply

$$\frac{\partial H_{j,k}}{\partial x_i} = P_{i,j,k} \tag{F20}$$

and the partials giving the distribution's sensitivity to translation of the delay coordinate (needed to estimate the position of the center of Saturn) is

$$\frac{\partial H_{j,k}}{\partial \tau} = \sum_i x_i (P_{i,j,k} - P_{i,j-1,k}) . \qquad \text{(F21)}$$

APPENDIX G. Stokes-vector formalism and scattering matrices

The electric field vector $\underset{\sim}{E}$ of a plane monochromatic electromagnetic wave traveling in direction $\hat{\underset{\sim}{k}}$, where $\hat{\underset{\sim}{k}} = \underset{\sim}{k}/|\underset{\sim}{k}|$ and $|\underset{\sim}{k}| = 2\pi/\lambda$, where λ is wavelength, has the form

$$\underset{\sim}{E}(\underset{\sim}{r},t) = \underline{\mathrm{Re}}\ \{\underset{\sim}{E}_0 e^{j(\underset{\approx}{k}\cdot\underset{\approx}{r}-\omega t)}\} \qquad \text{(G1)}$$

where the complex vector $\underset{\sim}{E}_0$ may be written

$$\underset{\sim}{E}_0 = \hat{\underset{\sim}{x}}\mathcal{E}_{0x} + \hat{\underset{\sim}{y}}\mathcal{E}_{0y} \qquad \text{(G2)}$$

where $\mathcal{E}_{0x}$, $\mathcal{E}_{0y}$ are complex variables:

$$\mathcal{E}_{0x} = E_{0x}e^{-j\delta_x} \; , \; \mathcal{E}_{0y} = E_{0y}e^{-j\delta_y} \qquad \text{(G3)}$$

Here E_0 and δ are the amplitude and phase, respectively.

Letting $z = \underset{\sim}{r}\cdot\hat{\underset{\sim}{k}}$ and $\phi = \omega t$, the Cartesian components of $\underset{\sim}{E}(\underset{\sim}{r},t)$ at $z = 0$ are given by

$$\underset{\sim}{E}(\underset{\sim}{r},t) \to \underset{\sim}{E}(\phi) = \hat{\underset{\sim}{x}}E_x + \hat{\underset{\sim}{y}}E_y + \hat{\underset{\sim}{z}}E_z \qquad \text{(G4)}$$

where

$$E_x = E_{0x}\cos(\phi+\delta_x) \; , \; E_y = E_{0y}\cos(\phi+\delta_y) \; , \; E_z = 0.$$

Eliminating ϕ gives (see Born and Wolf, 1975, p. 24, for algebra) the equation of an ellipse:

$$\left(\frac{E_x}{E_{0x}}\right)^2 + \left(\frac{E_y}{E_{0y}}\right)^2 - 2\frac{E_x}{E_{0x}}\frac{E_y}{E_{0y}}\cos\delta_{yx} = \sin^2\delta_{yx} \qquad \text{(G5)}$$

where $\delta_{yx} = \delta_y - \delta_x$. This ellipse, sketched in Fig. 28a, has an axial ratio a/b and a tilt angle τ. Kraus (1966, p. 113) gives useful relations between δ_{yx}, τ, ε, and γ, where cot ε = a/b and tan $\gamma = E_{0y}/E_{0x}$.

The Stokes parameters for narrowband ($\Delta\omega/\omega << 1$) signals are:

$$\begin{aligned} s_1 &= \langle E_{0x}^2 \rangle + \langle E_{0y}^2 \rangle \\ s_2 &= \langle E_{0x}^2 \rangle - \langle E_{0y}^2 \rangle = s_1 \cos 2\varepsilon \cos 2\tau \\ s_3 &= 2\langle E_{0x}E_{0y} \cos \delta_{yx} \rangle = s_1 \cos 2\varepsilon \sin 2\tau \\ s_4 &= 2\langle E_{0x}E_{0y} \sin \delta_{yx} \rangle = s_1 \sin 2\varepsilon \end{aligned} \tag{G6}$$

The angle brackets imply a time average and will be implicit henceforth. The quantities s_1, s_2 are the sum and difference of autocorrelation functions, while s_3, s_4 are cross-correlation functions, of the signals from two cross-polarized antennas.

By thinking of (E_x, jE_y) as Cartesian coordinates in the complex plane, one can construct $\underset{\sim}{E}(\phi)$ by superposing two counter-rotating phasors $E_R = E_{0R}e^{j\phi}$ and $E_L = E_{0L}e^{-j\phi+\delta'}$. Then (see Papas, 1975; or Jordan and Balmain, 1968)

$$\begin{aligned} E_x &= \text{Re}\,(E_R+E_L) = E_{0R} \cos \phi + E_{0L} \cos (\phi+\delta') \\ E_y &= \text{Im}\,(E_R+E_L) = E_{0R} \sin \phi - E_{0L} \sin (\phi+\delta') \end{aligned} \tag{G7}$$

Since the axial ratio a/b = cot $\varepsilon = (E_{0L}+E_{0R})/(E_{0L}-E_{0R})$, as

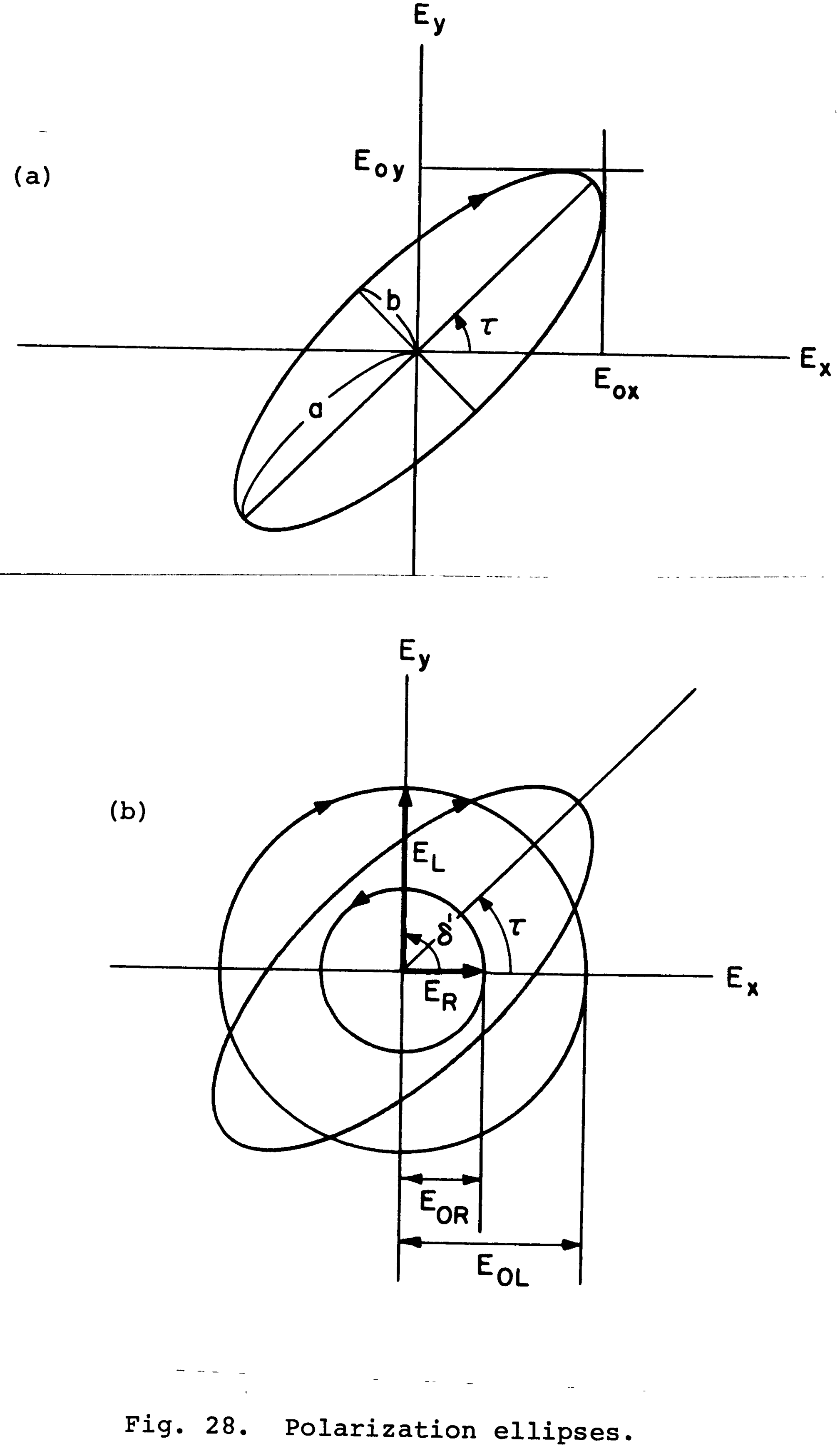

Fig. 28. Polarization ellipses.

shown in Fig. 28b, the double-angle trigonometric identities give

$$\cos 2\varepsilon = \frac{2E_{0L}E_{0R}}{E_{0L}^2+E_{0R}^2}$$

$$\sin 2\varepsilon = \frac{E_{0L}^2-E_{0R}^2}{E_{0L}^2+E_{0R}^2} \tag{G8}$$

Using these equations plus the fact that $\delta' = 2\tau$, the Stokes parameters become

$$s_1 = E_{0L}^2 + E_{0R}^2$$

$$s_2 = 2E_{0L}E_{0R} \cos \delta'$$

$$s_3 = 2E_{0L}E_{0R} \sin \delta' \tag{G9}$$

$$s_4 = E_{0L}^2 - E_{0R}^2$$

One may also write the Stokes parameters in terms of the complex amplitudes $\mathcal{E}_{0x}$ and $\mathcal{E}_{0y}$ defined above, as

$$s_1 = |\mathcal{E}_{0x}|^2 + |\mathcal{E}_{0y}|^2$$

$$s_2 = |\mathcal{E}_{0x}|^2 - |\mathcal{E}_{0y}|^2 \tag{G10}$$

$$s_3 = \mathcal{E}_{0x}\mathcal{E}_{0y}^* + \mathcal{E}_{0x}^*\mathcal{E}_{0y}$$

$s_4 = -j(E_{0x}E_{0y}^* - E_{0x}^* E_{0y})$

The Stokes parameters are discussed in considerable detail by Chandrasekhar, 1950; Green, 1968; Kraus, 1966; and Papas, 1965. They have the following physical interpretations, obvious from the above representations: s_1 equals the total power; s_2 measures the excess of horizontal linearly polarized power over the vertical component; s_3 has the same definition as s_2 but with both linearly polarized directions rotated 45° about $\underset{\sim}{k}$; and s_4 gives the excess of left-handed circularly polarized power (IAU definition) over the right circular polarized component. The degree of polarization of the wave is given by $(s_2^2+s_3^2+s_4^2)^{1/2}/s_1$. In practical applications, it is convenient to normalize s_i by dividing by s_1.

By treating (s_1,s_2,s_3,s_4) as a column vector $\underset{\sim}{s}$ and by incorporating the Fresnel amplitude reflection coefficients $r_\perp$ and $r_\parallel$ into a 4x4 matrix $\underset{\sim}{R}$ (Collett, 1968), reflection from a plane interface between two dielectric materials with refractive indices $n_2 > n_1$ can be represented by the equation: $\underset{\sim}{s}_r = \underset{\sim}{R}\underset{\sim}{s}_i$, where $\underset{\sim}{s}_i$ and $\underset{\sim}{s}_r$ are incident and reflected Stokes vectors, respectively. The incident (no second subscript) and reflected (second subscript "r") fields perpendicular and parallel to the plane of incidence are related as

$$E_{\perp r} = r_\perp E_\perp e^{-j\delta_\perp}$$

$$E_{\parallel r} = r_\parallel E_\parallel e^{-j\delta_\parallel} \qquad \text{(G11)}$$

where $E_\perp = E_{0x}$ and $E_\parallel = E_{0y}$ in the above notation.

The incident Stokes vector $\underset{\sim}{s}_i$ and the reflected Stokes vector $\underset{\sim}{s}_r$ have the following components:

Incident

$$\begin{aligned}
s_{i1} &= E_\perp E_\perp^* + E_\parallel E_\parallel^* = \mathrm{E}_\perp^2 + \mathrm{E}_\parallel^2 \\
s_{i2} &= E_\perp E_\perp^* - E_\parallel E_\parallel^* = \mathrm{E}_\perp^2 - \mathrm{E}_\parallel^2 \\
s_{i3} &= E_\perp E_\parallel^* + E_\perp^* E_\parallel = 2\mathrm{E}_\perp \mathrm{E}_\parallel \cos\delta \\
s_{i4} &= -j(E_\perp E_\parallel^* - E_\perp^* E_\parallel) = -2\mathrm{E}_\perp \mathrm{E}_\parallel \sin\delta
\end{aligned} \tag{G12}$$

reflected

$$\begin{aligned}
s_1 &= E_{\perp r} E_{\perp r}^* + E_{\parallel r} E_{\parallel r}^* = r_\perp^2 \mathrm{E}_\perp^2 + r_\parallel^2 \mathrm{E}_\parallel^2 \\
s_2 &= E_{\perp r} E_{\perp r}^* - E_{\parallel r} E_{\parallel r}^* = r_\perp^2 \mathrm{E}_\perp^2 - r_\parallel^2 \mathrm{E}_\parallel^2 \\
s_3 &= E_{\perp r} E_{\parallel r}^* + E_{\perp r}^* E_{\parallel r} = r_\perp r_\parallel \mathrm{E}_\perp \mathrm{E}_\parallel (e^{j(\delta_\parallel-\delta_\perp)} + e^{j(\delta_\parallel-\delta_\perp)}) \\
&= 2r_\perp r_\parallel \mathrm{E}_\perp \mathrm{E}_\parallel \cos\delta \\
s_4 &= -j(E_{\perp r} E_{\parallel r}^* - E_{\perp r}^* E_{\parallel r}) = -jr_\perp r_\parallel \mathrm{E}_\perp \mathrm{E}_\parallel (e^{-j\delta} - e^{j\delta}) \\
&= -2r_\perp r_\parallel \mathrm{E}_\perp \mathrm{E}_\parallel \sin\delta
\end{aligned} \tag{G13}$$

where $\delta = \delta_\perp - \delta_\parallel$. Thus one can write $\underset{\sim}{s}_r = \underset{\sim}{R}\,\underset{\sim}{s}_i$ with

$$\underset{\sim}{R}(\theta) = \frac{1}{2}\begin{bmatrix} (r_\perp^2+r_\parallel^2) & (r_\perp^2-r_\parallel^2) & 0 & 0 \\ (r_\perp^2-r_\parallel^2) & (r_\perp^2+r_\parallel^2) & 0 & 0 \\ 0 & 0 & 2r_\perp r_\parallel & 0 \\ 0 & 0 & 0 & 2r_\perp r_\parallel \end{bmatrix} \qquad \text{(G14)}$$

where

$$r_\perp = (\cos\,\theta - \underline{n}\cos\,\underline{t})/(\cos\,\theta + \underline{n}\cos\,\underline{t})$$
$$r_\parallel = (\underline{n}\cos\,\theta - \cos\,\underline{t})/(\underline{n}\cos\,\theta + \cos\,\underline{t}) \qquad \text{(G15)}$$

and the angles θ (of incidence and reflection) and $\underline{t}$ (of transmission) are related by Snell's Law: $\underline{n}\sin\,\underline{t} = \sin\,\theta$, where $\underline{n} = n_2/n_1$ and reflection occurs in the medium with index n_1.

When $\theta \neq 0$, calculations are faster if these equations are rewritten as

$$r_\perp = -\sin\,(\theta-t)/\sin\,(\theta+t)$$
$$r_\parallel = \tan\,(\theta-t)/\tan\,(\theta+t) \qquad \text{(G16)}$$

At the Brewster angle θ_B one has $\theta_B+t = \pi/2$ so $r_\parallel = 0$ and $r_\perp^2 = \sin^2(\theta_B-t)$. Since $\cos\,t = \cos\,(\pi/2 - \theta_B) = \sin\,\theta_B$ and $\sin\,t = \cos\,\theta_B$,

$$r_\perp = (\sin\,\theta_B\cos\,t - \cos\,\theta_B\sin\,t)^2 = (\sin^2\,\theta_B - \cos^2\,\theta_B)^2$$
$$= \cos^2\,2\theta_B \qquad \text{(G17)}$$

so

$$\underset{\sim}{R}(\theta_B) = \frac{1}{2}\cos^2\,2\theta_B\begin{bmatrix} 1 & 1 & 0 & 0 \\ 1 & 1 & 0 & 0 \\ 0 & 0 & 0 & 0 \\ 0 & 0 & 0 & 0 \end{bmatrix} \qquad \text{(G18)}$$

Two successive reflections which, together, yield a double-bounce backscattering event, share the same plane of incidence. Thus the net target matrix describing this scattering is simply the product of the reflection matrices for the individual reflections at angles θ_1 and θ_2 ($\theta_2 = 90° - \theta_1$; see Fig. 29):

$$\underset{\sim}{\hat{T}}(\phi=0°) = \underset{\sim}{R}(\theta_2)\ \underset{\sim}{R}(\theta_1) \tag{G19}$$

where ϕ is the azimuth (arbitrarily set equal to zero for the moment) of the plane of incidence relative to some fixed coordinate system. The net scattering effect of any mixture of planes, dipoles, or arbitrary scatterers can be described completely by a suitable target matrix $\underset{\sim}{\hat{T}}$.

Normally we are interested only in the strength and polarization properties of a wave backscattered from an ensemble of many statistically identical configurations, randomly distributed over all azimuths ϕ. It is easy to show (App. I) that averaging over all orientations is equivalent to replacing the matrix $\underset{\sim}{\hat{T}}$, for a scattering configuration at a particular azimuth, with the diagonal matrix $\underset{\sim}{T}$, where

$$\underset{\sim}{T} = \begin{bmatrix} \hat{T}_{11} & & & 0 \\ & \frac{1}{2}(\hat{T}_{22}-\hat{T}_{33}) & & \\ & & (\hat{T}_{33}-\hat{T}_{22}) & \\ 0 & & & \hat{T}_{44} \end{bmatrix} \tag{G20}$$

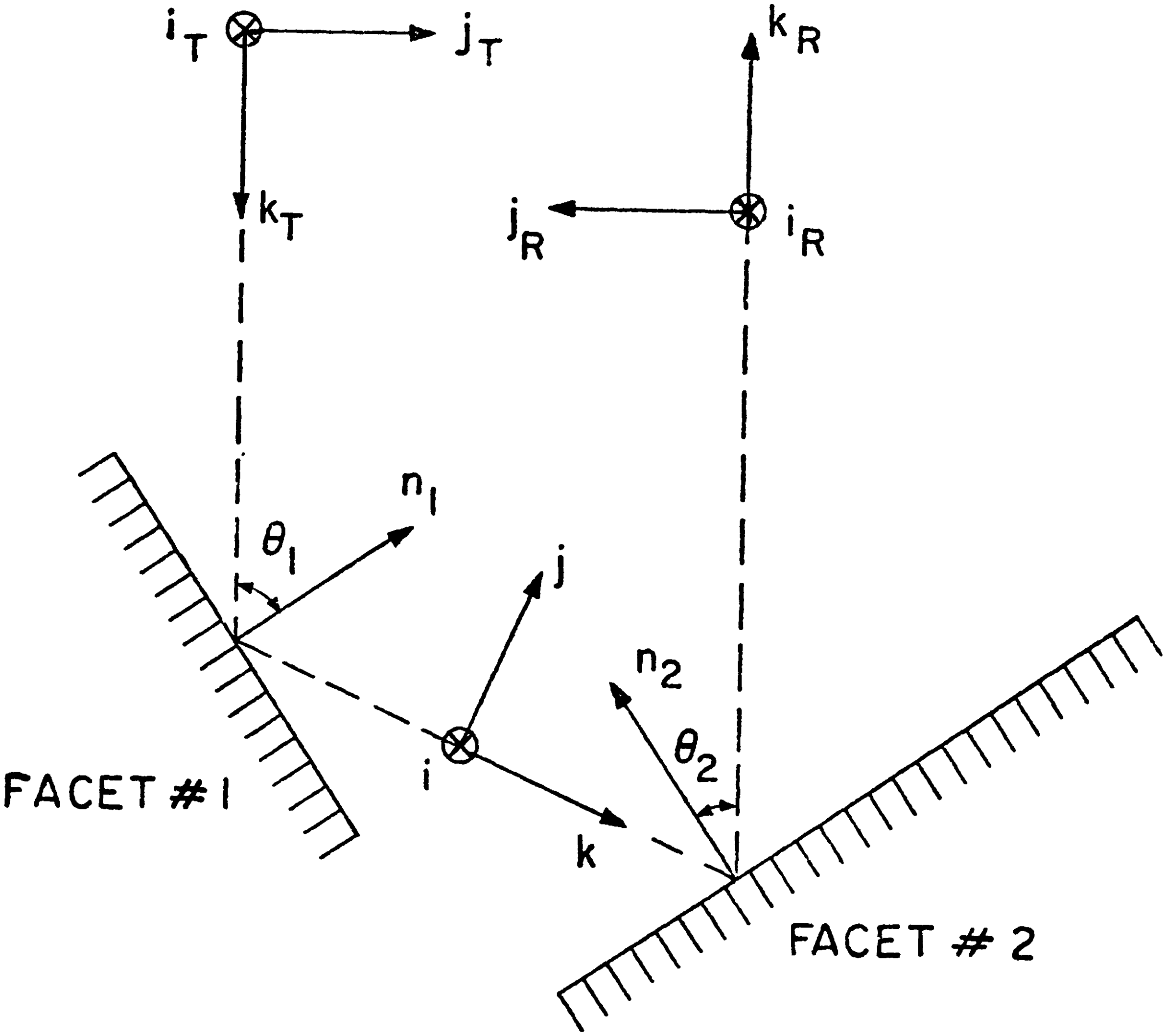

Fig. 29. Coordinate systems used to determine the polarization of the transmitted ($\underset{\sim}{i}_T$, $\underset{\sim}{j}_T$, $\underset{\sim}{k}_T$) and received ($\underset{\sim}{i}_T$, $\underset{\sim}{j}_T$, $\underset{\sim}{k}_T$) radio waves backscattered in two successive reflections from plane facets. The plane of incidence lies in the paper. The unlabeled coordinate system ($\underset{\sim}{i}$, $\underset{\sim}{j}$, $\underset{\sim}{k}$) is used to describe the wave between reflections.

The difference in the elements T_{22} and T_{33} between this result and that given by Hagfors (1967) arises from my definition of incident and reflected coordinate systems, as discussed in Appendix I.

The polarization ratios for backscattering from a target with (diagonal) reflection matrix $\underset{\sim}{T}$ follow immediately from the definitions of μ_C, μ_L, and the Stokes parameters:

$$\mu_C = \frac{s_1+s_4}{s_1-s_4} = \frac{T_{11}+T_{44}}{T_{11}-T_{44}}$$

and (G21)

$$\mu_L = \frac{s_1-s_2}{s_1+s_2} = \frac{T_{11}-T_{22}}{T_{11}+T_{22}}$$

For example, the matrix for a single reflection at normal incidence from a lossless dielectric with refractive index $\underline{n}$ is

$$\underset{\sim}{R}(0°) = \left(\frac{\underline{n}-1}{\underline{n}+1}\right)^2 \begin{bmatrix} 1 & & & 0 \\ & 1 & & \\ & & -1 & \\ 0 & & & -1 \end{bmatrix} \qquad \text{(G22)}$$

from Eq. (G14) with $r_\perp = -\frac{n-1}{n+1}$ and $r_\parallel = \frac{n-1}{n+1}$. Thus, $\mu_C = 0$ for this case and $\underset{\sim}{s}_r$ is completely circularly polarized with rotational sense (sign of s_4) opposite to that of s_i. The ratio μ_C is also zero for simple backscattering from Rayleigh particles (Chandrasekhar, 1950, p. 37) or from any perfectly symmetrical object (Beckmann, 1968, p. 190).

APPENDIX H. The whole-target scattering matrix

The calculation of the whole-target scattering matrix $\underset{\sim}{C}$ proceeds as follows: First I follow the paths of rays incident at any point (θ_1, ϕ_1) on the crater interior (Fig. 30). The symmetry allows me to analyze the scattering resulting from the illumination of points at $0 \leqslant \theta_1 \leqslant 90°$ but lying at a fixed azimuth $(\phi_1 = 0)$, and then simply to average the results over all azimuths. Finally, since the limit ε_c to the angular deviation of facets from the direction of the local spherical radius is assumed to be small, the ranges of angles θ_1 giving either single- or double-bounce echoes are easily derived and the two types of contributions to the scattering can be calculated separately. The scattering matrix which describes the effects of these processes for a diametral section of the crater corresponding to $\phi_1 = 0$ is defined as $\hat{\underset{\sim}{A}}$. Suppressing, for clarity, the explicit dependence of $\hat{\underset{\sim}{A}}$ on most independent variables, I may write that part which arises from double-bounce backscatter, assuming illumination only of a facet at $(\theta_1, 0)$, as

$$\hat{\underset{\sim}{A}}(\theta_1) = \iint_{\varepsilon} d\gamma_1 d\beta_1 P[\varepsilon(\gamma_1,\beta_1)] \left\{ \iint_{\substack{\text{illum}\\ \text{area}}} d\theta_2 d\phi_2 \iint_{\varepsilon} d\gamma_2 d\beta_2 P[\varepsilon(\gamma_2,\beta_2)] \underset{\sim}{R}_2 G_2 \right\} \underset{\sim}{R}_1 G_1 F^2 \cos\theta_1 \tag{H1}$$

where the angular deviation ε of a facet normal from the direction of the crater center is given by $\varepsilon(\gamma, \beta) =$

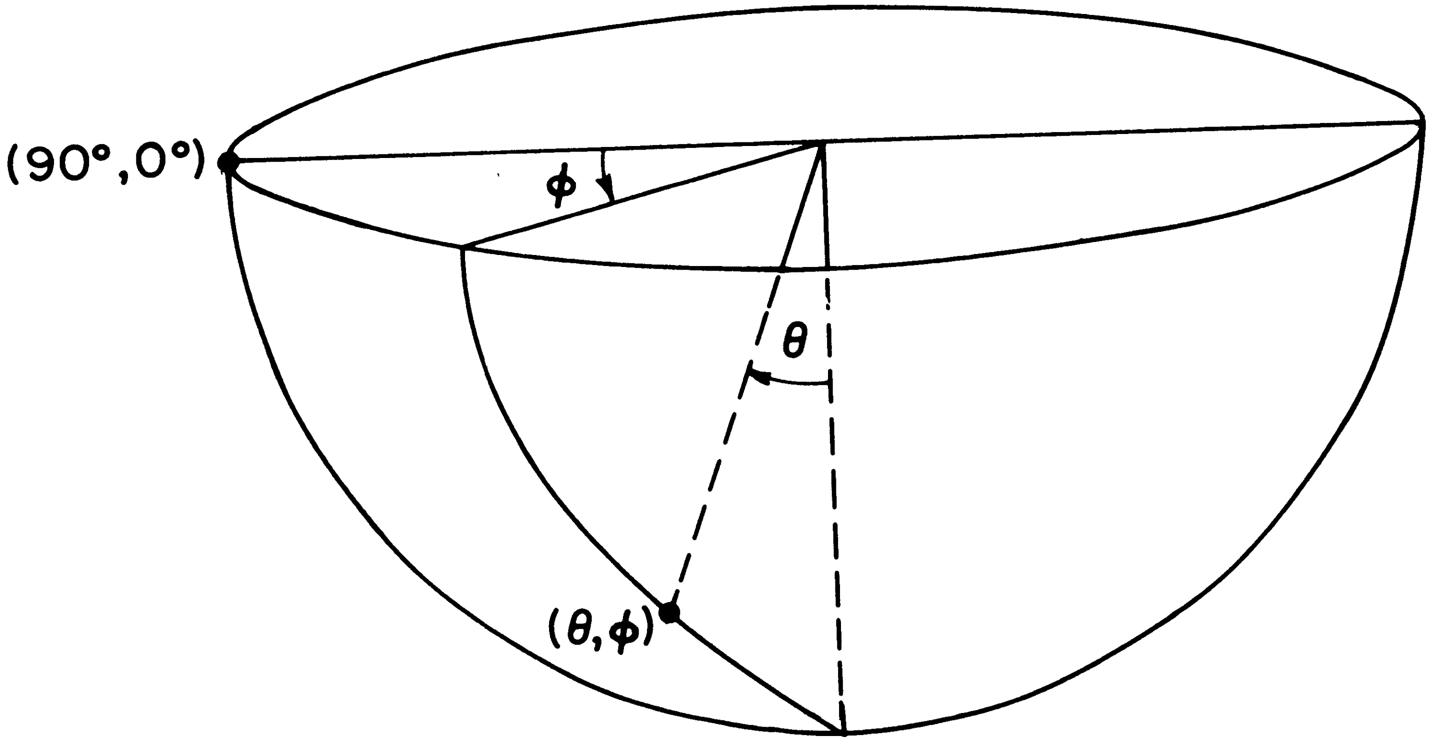

Fig. 30. Coordinate system used in calculation of the scattering matrix for a hemispherical crater. For the values of ε_c and F_λ considered, single-reflection echoes occur within a few degrees of $\theta = 0°$, while double-reflection echoes originate along an annulus near $\theta = 45°$.

$\cos^{-1}(\cos\gamma\cos\beta)$ and γ and β are (small) angles in orthogonal planes specifying the precise orientation of the deviation. $\underset{\sim}{R}_1$ and $\underset{\sim}{R}_2$ are scattering matrices (Appendix G) for the two reflections, and G is the directivity of a facet as defined below.

The outermost double integral in Eq. (H1) accounts for all orientations of a facet which is located in the crater at $(\theta_1, 0)$; the direction of the ray reflected from this facet is calculated by simple analytical geometry for each orientation. The area on the opposite side of the crater which is illuminated by the directivity pattern associated with this first reflection is then determined. The calculation uses an approximation to the true diffraction pattern from a finite plane sheet (Beckmann, 1968, p. 67) in which the directivity (or gain) G_1 is taken to be constant at a maximum value within a rectangular solid angle (and zero elsewhere) such that the surface integral of the approximation is equal to that over the main lobe of the actual function. The second double integral treats all points (θ_2, ϕ_2) so illuminated. For each of these points, all possible orientations of the second facet must also be considered, giving the innermost double integral in Eq. (H1). Again, a directivity G_2 is assumed for the second facet; and the contribution back toward the radar is determined. The reflection matrices $\underset{\sim}{R}_1$ and $\underset{\sim}{R}_2$ are calculated for the first and second facets and are appropriately normalized to yield the reflected power per steradian for unit flux incident on the crater. The corresponding values of echo power for specific radar cross section are, by definition, larger by a factor of 4π, (Green, 1968). The factor $(F^2 \cos\theta_1)$ weights $\hat{\underset{\sim}{A}}$ by the capture area of the first facet. The calculation of that part of $\hat{\underset{\sim}{A}}$ which corresponds to single-reflection backscatter may be obtained by removing the bracketed integrals from Eq. (H1). Since we are interested in the value of $\hat{\underset{\sim}{A}}$ averaged over all azimuths ϕ, I replace it by $\underset{\sim}{A}$ as described in Appendix G.

There remains the calculation of the scattering matrix $\underset{\sim}{B}$ appropriate to a hemispherical crater located at an angle $\underline{I}$ from the subradar point. The number of facets N located at θ_1 inside the crater is approximately equal to $2\pi R \sin\theta_1/F$. If $\delta(\underline{I}, \theta_1)$ represents the reduction in N due to shadowing by the crater lip (Appendix J), the reflected power per unit solid angle per unit incident flux from a crater inclined at angle $\underline{I}$ is the first element B_{11} of the scattering matrix

$$\underset{\sim}{B}(I) = \int_0^{\pi/2} (2\pi R \sin\theta_1/F)\, \delta(\underline{I}, \theta_1)\, \underset{\sim}{A}(\theta_1)\, d\theta_1 \qquad \text{(H2)}$$

which may be modified to give

$$\underset{\sim}{S}(\underline{I}) = 4\underset{\sim}{B}(\underline{I})\cos\underline{I}/R^2 \qquad \text{(H3)}$$

where the first element S_{11} becomes the specific radar cross section $\sigma_o(\underline{I})$. Finally, the total target scattering matrix

$\underset{\sim}{C}$, normalized so that its first element is equal to the geometric albedo α, is calculated from

$$\underset{\sim}{C} = \frac{1}{2} \int_0^{\pi/2} \underset{\sim}{S}(\underline{I}) \sin \underline{I} \, d\underline{I} \tag{H4}$$

The polarization ratios follow immediately from Eqs. (G21).

I have calculated $\underset{\sim}{C}(\underline{n}, F_\lambda, R_\lambda, \varepsilon_c)$ for selected values of each of the variables. The integrals in the above equations were evaluated numerically; although errors introduced by quantization are non-negligible, I feel that the accuracy of the curves shown in Fig. 11 is adequate when compared to the uncertainties in the observed data.

APPENDIX I. Rotational transformation of scattering matrices

Rotation of a coordinate system through an angle ψ causes components of a 2-D vector $\underset{\sim}{E}$ to transform according to

$$E_{x\psi} = E_x \cos \psi + E_y \sin \psi, \quad E_{y\psi} = -E_x \sin \psi + E_y \cos \psi$$

or, abbreviating the trigonometric functions,

$$\begin{pmatrix} E_{x\psi} \\ E_{y\psi} \end{pmatrix} = \begin{pmatrix} C & S \\ -S & C \end{pmatrix} \begin{pmatrix} E_x \\ E_y \end{pmatrix}$$

The Stokes parameters (defined in App. G) transform as:

$$s_{1\psi} = |E_{x\psi}|^2 + |E_{y\psi}|^2 = |CE_x + SE_y|^2 + |-SE_x + CE_y|^2$$

$$= |E_x|^2 (C^2+S^2) + |E_y|^2 (S^2+C^2) + SC(E_x E_y^* + E_x^* E_y - E_x E_y^* - E_x^* E_y)$$

$$= |E_x|^2 + |E_y|^2 = s_1 \qquad \text{(I1)}$$

$$s_{2\psi} = |E_{x\psi}|^2 - |E_{y\psi}|^2$$

$$= (CE_x + SE_y)(CE_x^* + SE_y^*) - (-SE_x + CE_y)(-SE_x^* + CE_y^*)$$

$$= C^2 |E_x|^2 + S^2 |E_y|^2 + 2SC(E_x E_y^* + E_x^* E_y) - S^2 |E_x|^2 - C^2 |E_y|^2$$

$$= s_2 \cos 2\psi + s_3 \sin 2\psi \qquad \text{(I2)}$$

$$s_{3\psi} = E_{x\psi}E_{y\psi}^{*}+E_{x\psi}^{*}E_{y\psi}$$

$$= (CE_x+SE_y)(-SE_x^{*}+CE_y^{*})+(CE_x^{*}+SE_y^{*})(-SE_x+CE_y)$$

$$= -SC(|E_x|^2-|E_y|^2)-S^2E_x^{*}E_y+C^2E_xE_y^{*}$$

$$-SC(|E_x|^2-|E_y|^2)-S^2E_xE_y^{*}+ C^2E_x^{*}E_y$$

$$= s_3 \cos 2\psi - s_2 \sin 2\psi \tag{I3}$$

$$s_{4\psi} = -j(E_{x\psi}E_{y\psi}^{*}-E_{x\psi}^{*}E_{y\psi})$$

$$= -j[(CE_x+SE_y)(-SE_x^{*}+CE_y^{*})-(CE_x^{*}+SE_y^{*})(-SE_x+CE_y)]$$

$$= -j[-SC|E_x|^2+CS|E_y|^2-S^2E_x^{*}E_y+C^2E_xE_y^{*}$$

$$+CS|E_x|^2-CS|E_y|^2+S^2E_xE_y^{*}-C^2E_x^{*}E_y]$$

$$= -j(E_xE_y^{*}-E_x^{*}E_y) = s_4 \tag{I4}$$

Thus $\underset{\sim}{s}_4 = \underset{\sim}{V}(\psi)\underset{\sim}{s}$, where

$$\underset{\sim}{V}(\psi) \qquad \underset{\sim}{V}_{\psi} = \begin{bmatrix} 1 & 0 & 0 & 0 \\ 0 & \cos 2\psi & \sin 2\psi & 0 \\ 0 & -\sin 2\psi & \cos 2\psi & 0 \\ 0 & 0 & 0 & 1 \end{bmatrix} \tag{I5}$$

The unit value for $V_{\parallel}(\psi)$ is consistent with conservation of energy: The total intensity $(s_{\parallel})$ of a wave cannot depend on ψ. Similarly, the relative contributions of right- and left-circularly polarized components are independent of rotational orientation of the coordinate system, so $V_{44}(\psi)$ must equal unity.

Given a scattering interaction described by $\underset{\sim}{s}_r = \underset{\sim}{T}_o\underset{\sim}{s}_i$, I would like to determine the effect of coordinate system rotation on the Mueller matrix $\underset{\sim}{T}_o$. That is, in a coordinate system rotated through angle ψ I wish to write $\underset{\sim}{s}_r = \underset{\sim}{T}_\psi\underset{\sim}{s}_i$ where $\underset{\sim}{T}_\psi$ is a function of $\underset{\sim}{T}_o$. This entails a straightforward similarity transformation (Arfken, 1970, p. 182)

$$\underset{\sim}{V}_\psi\underset{\sim}{s}_r = \underset{\sim}{V}_\psi\underset{\sim}{T}_o\underset{\sim}{s}_i \quad \underset{\sim}{V}_\psi\underset{\sim}{T}_o\underset{\sim}{V}_\psi^{-1}\underset{\sim}{V}_\psi\underset{\sim}{s}_i$$

or (I6)

$$\underset{\sim}{s}_{r\psi} = (\underset{\sim}{V}_\psi\underset{\sim}{T}_o\underset{\sim}{V}_\psi^{-1})\underset{\sim}{s}_{i\psi} = \underset{\sim}{T}_\psi\underset{\sim}{s}_{i\psi}$$

where

$$V_\psi^{-1} \equiv V_{-\psi}.$$

Now, derivation of the scattering matrix has assumed that the Stokes vector is measured using a coordinate system fixed in the measuring instrument, which "sees" the polarization ellipse by looking into the source, i.e., along the $-\underset{\sim}{\hat{z}}$ direction. Hence, I wish to keep $\underset{\sim}{s}_i$ constant, rotate my instrument coordinate system through ψ relative to the scatterer (i.e., rotate T_o through $-\psi$), then perform my experiment and be able to describe it as $\underset{\sim}{s}_r = \underset{\sim}{T}_\psi\underset{\sim}{s}_i$, where the form of $\underset{\sim}{T}_\psi$ has yet to be found. Suppose I am settled in my new orientation, having rotated through ψ relative to the target, which may be a polarizing lens, say. Then I can simulate my desired experiment mathematically by (a) rotating $\underset{\sim}{s}_i$ through $-\psi$ so it is described in the same coordinate system as $\underset{\sim}{T}_o$:

$$\underset{\sim}{s}_i \rightarrow \underset{\sim}{V}_{\psi}^{-1}\underset{\sim}{s}_i \tag{I7}$$

then (b) operating on this Stokes parameter with $\underset{\sim}{T}_o$, and finally (c) rotating the coordinate system through ψ, back to that of my instrument:

$$\underset{\sim}{s}_r \rightarrow \underset{\sim}{V}_{\psi}\underset{\sim}{T}_o\underset{\sim}{V}_{\psi}^{-1}\underset{\sim}{s}_i \tag{I8}$$

However, implicit in derivation of the Fresnel coefficients (see, for example, Jackson, 1962, p. 216) is a change in direction of wave propagation during reflection. I have maintained the conventions that the $\hat{x},\hat{y}$ directions are $\perp$, $\parallel$ to the plane of incidence, that $\underset{\sim}{s}$ is always measured looking in the $-\underset{\sim}{\hat{z}}$ direction, and that the unit vector $\underset{\sim}{\hat{y}}$ always points away from the reflecting surface such that $\underset{\sim}{\hat{y}}\cdot\underset{\sim}{\hat{n}} > 0$, where $\hat{n}$ is the surface outward unit normal. Thus, for <u>backscattering</u> involving one or more reflections, all of which take place in a single plane, as illustrated in Fig. 29 [which substitutes $(\hat{\imath},\hat{\jmath},\hat{k})$ for $(\hat{x},\hat{y},\hat{z})$], the directions of $\underset{\sim}{\hat{y}}$ and $\underset{\sim}{\hat{z}}$ in the separate coordinate systems describing $\underset{\sim}{s}_i$ and $\underset{\sim}{s}_r$ are opposed while $\underset{\sim}{\hat{x}}$ remains the same.

The effect of this "coordinate system flip" on Eqn. (I8) is that the final step must be a rotation through $-\psi$ instead of through ψ, so

$$\underset{\sim}{s}_r = \underset{\sim}{V}^{-1}\underset{\sim}{T}_o\underset{\sim}{V}^{-1}\underset{\sim}{s}_i \tag{I9}$$

Therefore, in a backscattering situation with $\underset{\sim}{s}_r$, $\underset{\sim}{s}_i$ and $\underset{\sim}{T}_o$ as given, the effect of rotating a target through ψ relative to the transmitting coordinate system is to replace $\underset{\sim}{T}_o$ with

$$\underset{\sim}{T}_\psi = \underset{\sim}{V}_\psi^{-1}\underset{\sim}{T}_o\underset{\sim}{V}_\psi^{-1} \tag{I10}$$

Consider the following example. Let $\underset{\sim}{T}_o$ describe a simple normal reflection from a perfect plane mirror:

$$\underset{\sim}{T}_o = \begin{pmatrix} 1 & & & 0 \\ & 1 & & \\ & & -1 & \\ 0 & & & -1 \end{pmatrix} \tag{I11}$$

Then, letting C = cos 2ψ and S = sin 2ψ,

$$\underset{\sim}{T}_\psi = \begin{pmatrix} 1 & 0 & 0 & 0 \\ 0 & C & -S & 0 \\ 0 & S & C & 0 \\ 0 & 0 & 0 & 1 \end{pmatrix} \begin{pmatrix} 1 & & & 0 \\ & 1 & & \\ & & -1 & \\ 0 & & & -1 \end{pmatrix} \begin{pmatrix} 1 & 0 & 0 & 0 \\ 0 & C & -S & 0 \\ 0 & S & C & 0 \\ 0 & 0 & 0 & 1 \end{pmatrix}$$

$$= \begin{pmatrix} 1 & 0 & 0 & 0 \\ 0 & C & S & 0 \\ 0 & S & -C & 0 \\ 0 & 0 & 0 & 1 \end{pmatrix} \begin{pmatrix} 1 & 0 & 0 & 0 \\ 0 & C & -S & 0 \\ 0 & S & C & 0 \\ 0 & 0 & 0 & 1 \end{pmatrix} = \begin{pmatrix} 1 & & & 0 \\ & 1 & & \\ & & -1 & \\ 0 & & & -1 \end{pmatrix}, \tag{I12}$$

or $\underset{\sim}{T}_\psi = \underset{\sim}{T}_o$, as it must be, since the mirror is azimuthally symmetric. If one applied expression (I8), one would find that

$$T_\psi = \begin{bmatrix} 1 & 0 & 0 & 0 \\ 0 & (C^2-S^2) & (-2SC) & 0 \\ 0 & (-2SC) & (S^2-C^2) & 0 \\ 0 & 0 & 0 & 1 \end{bmatrix} \qquad \text{(I13)}$$

contradicting the required invariance of rotation in influencing the effect of a perfect reflecting mirror on the polarization of a backscattered wave.

To average over all azimuthal orientations of a target, I must calculate

$$\langle \underset{\sim}{T} \rangle = \frac{1}{\pi} \int_{-\pi/2}^{\pi/2} d\psi \; \underset{\sim}{T}(\psi) \qquad \text{(I14)}$$

Assuming that $\underset{\sim}{T}_o$ has the form

$$\underset{\sim}{T}_o \equiv \underset{\sim}{T}(0) = \begin{bmatrix} T_{11} & T_{12} & 0 & 0 \\ T_{21} & T_{22} & 0 & 0 \\ 0 & 0 & T_{33} & 0 \\ 0 & 0 & 0 & T_{44} \end{bmatrix} \qquad \text{(I15)}$$

I calculate

$$\underset{\sim}{T}_\psi = \begin{bmatrix} T_{11} & CT_{12} & -ST_{12} & 0 \\ CT_{21} & (C^2T_{22}-S^2T_{33}) & CS(T_{22}-T_{33}) & 0 \\ ST_{21} & CS(T_{22}+T_{33}) & C^2T_{33}-S^2T_{22} & 0 \\ 0 & 0 & 0 & T_{44} \end{bmatrix} \qquad \text{(I16)}$$

Since the above definite integral of sin 2ψ, cos 2ψ, or sin 2ψ cos 2ψ is zero, while that of $\sin^2 2\psi$ or $\cos^2 2\psi$ is 1/2,

$$\langle \underset{\sim}{T} \rangle = \begin{bmatrix} T_{11} & & & 0 \\ & \frac{1}{2}(T_{22}-T_{33}) & & \\ & & \frac{1}{2}(T_{33}-T_{22}) & \\ 0 & & & T_{44} \end{bmatrix} \qquad \text{(I17)}$$

This is identical to Eqn. (G20), written in slightly different notation.

APPENDIX J. Calculation of the reduction factor δ for the icy crater model

The calculation of the whole-target scattering matrix for backscattering from smooth-faceted, nearly hemispherical craters is detailed in Appendix H. As described there, one sees single reflections from facets oriented such that the angle of incidence θ_1 (between the incident ray and the facet normal) is close to zero, and double reflections from a pair of facets oriented so the ray path defines two successive angles of incidence $\theta_1 \approx \theta_2 \approx 45°$. Here, θ_1 is the angle of incidence to the "first-reflection" facet.

For a given angle $\underline{I}$ (between the line of sight and the normal to the plane containing the crater rim), the crater will contain a number $\underline{N}$ (Appendix H) of first-reflection facets located in an annulus which is an angle θ_1 up the crater wall from the projection $\underline{C}$ of the crater center of curvature upon the crater surface. Figure 31 shows the pertinent geometry for $\theta_1 = 45°$, $\underline{I} = 30°$. The crater is not a complete hemishpere, having been "trimmed" by an angle τ, equal to 20° in the figure. Two orthogonal views are drawn, the upper projection being along the radar line of sight.

It is clear from the figure that there are many combinations of θ_1, $\underline{I}$, and τ for which $\underline{N}$ will be degraded by "blockage" of part of the reflection annulus by the near rim, or by "vignetting" of the annulus by the far rim.

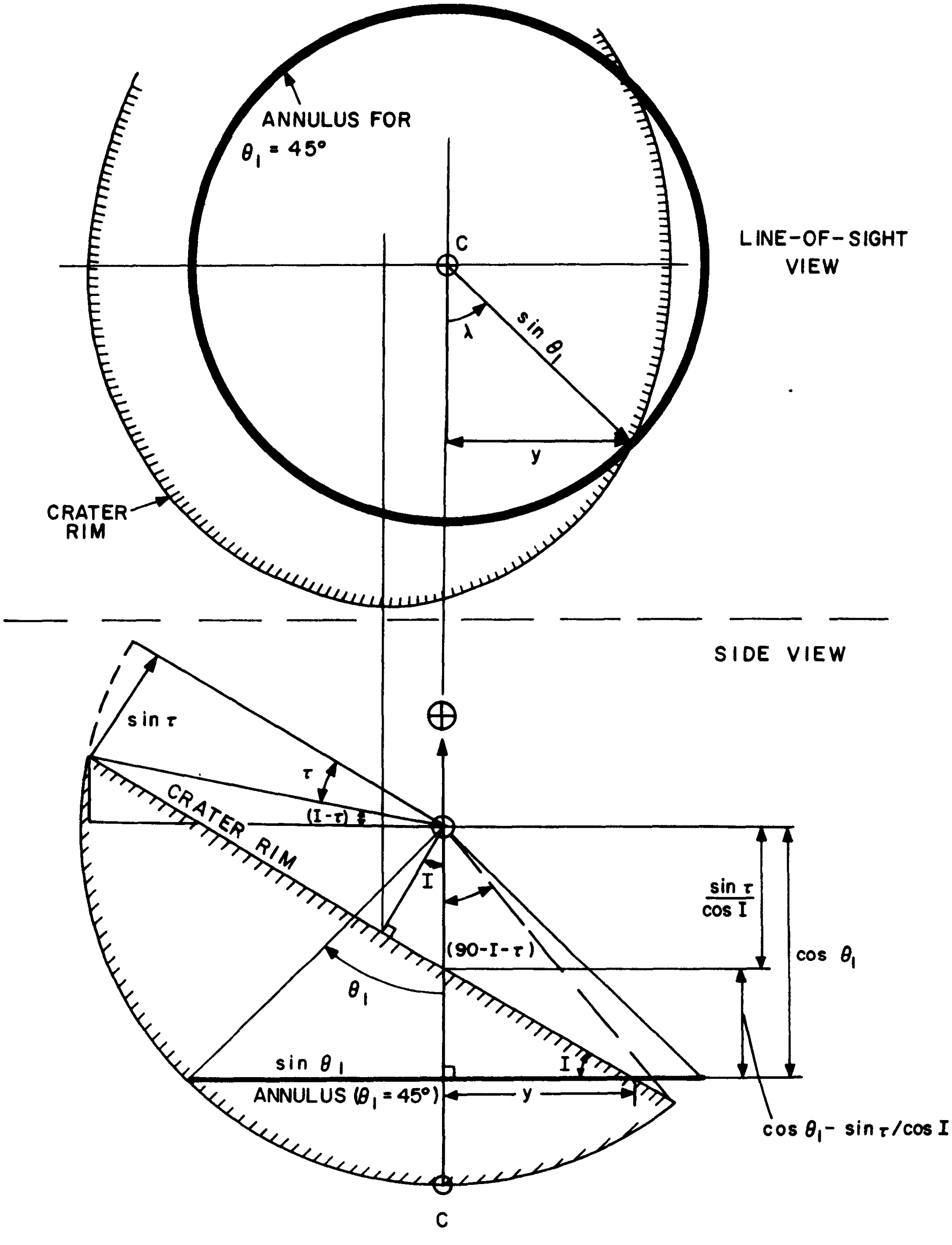

Fig. 31. Geometry for derivation of the reduction factor δ.

The figure shows one possible vignetting situation. Note that N for single-reflection backscatter is reduced by a factor $(90° + \lambda)/180° = \frac{1}{2} + \lambda/180°$, where the angle λ is designated in the figure. For double-reflection backscatter, this factor would be $\lambda/90°$. I shall call this reduction factor δ_1 or δ_2 to distinguish single- and double-reflection situations. The following procedure for determining δ_1, δ_2 is in the context of the practical ranges of acceptable values of I and τ for the pertinent calculations: $0° \leqslant I \leqslant 90°$ and $0° \leqslant \tau \leqslant 45°$.

It can be deduced from the figure that blockage occurs when $\cos(I - \tau) \leqslant \sin\theta_1$, while vignetting occurs when $\cos(I + \tau) \leqslant \sin\theta_1$. Hence θ_2 can be thought of as arising from vignetting alone.

If I $< (90° - \tau)$, C is inside the crater. If additionally, $\theta_1 \leqslant (90° - \tau) - I$, the annulus will not intercept the rim. In this case, the entire annulus is visible and inside the crater, so $\delta_1 = \delta_2 = 1$. Of course, if $\theta_1 > (90° - \tau)$, such as can occur for double reflections as $\tau \to 45°$, the annulus encircles the crater rim and $\delta_2 = 0$.

If I $\geqslant (90° - \tau)$, C is outside the crater. If additionally, $\theta_1 \leqslant I - (90° - \tau)$, the annulus will not intercept the rim. In this case, $\delta_1 = \delta_2 = 0$.

For those cases when the annulus does intercept the rim, the angle λ can be evaluated (Fig. 31):

$$\lambda = \sin^{-1}(y/\sin\theta_1) \tag{J1}$$

where

$$\underline{y} = (\cos\theta_1 - \sin\tau/\cos I)/\tan I. \tag{J2}$$

In such situations δ_1 and δ_2 must be calculated separately:

$$\delta_1 = 1/2 + \frac{\lambda}{180^\circ} \tag{J3}$$

$$\delta_2 = \begin{cases} \lambda/90^\circ, & \lambda > 0^\circ \\ 0 & , \lambda \leqslant 0^\circ \end{cases} \tag{J4}$$

APPENDIX K. Saturn ringlet dimensions and areas

Saturn's rings may be divided into ringlets, with the following boundaries, given in units of the equatorial radius $R_{♄}$ of Saturn, where $R_{♄}$ has been assumed equal to 5.978×10^{7} m [Table I of Pollack (1975)]. Also listed are ringlet visible geometric areas for the opening angle $|B| = 21.4°$.

TABLE XV. Saturn ringlet boundaries.

Ringlet		Boundaries ($R_{♄}$)	Geom. area (10^{15} m^2)
D		1.010 - 1.220	3.438
C		1.280 - 1.530	5.984
B	B3	1.530 - 1.625	2.752
	B2	1.625 - 1.755	4.146
	B1	1.755 - 1.950	7.045
A	A2	2.030 - 2.165	5.760
	A1	2.165 - 2.290	5.785

The outer boundaries of the B and A rings are from Table I of Cuzzi and Pollack (1978), which is based on figures given by Cook *et al.* (1973). My subdivision of these rings is similar to that given by Cook *et al.* (1973), the small differences being due, in part, to the quantization of my numerical model. My C ring extends from the B-ring inner edge to $1.28R_{♄}$ [Table XXII of Newburn and Gulkis (1973)]. My D-ring boundaries are $0.01R_{♄}$ larger than those given in the Newburn and Gulkis (1973) table.

Table XVI lists areas and maximum relative Doppler shift ν_{max} due to particles orbiting at the inner edge of the B ring for a 2380 MHz transmission. There are entries for the opening angles $|B|$ corresponding to the five S-band radar studies of the rings to date, as well as for $|B| = 5.6°$, which will occur during the observations planned for February 1979. The calculations use the numerical model described in Appendix F, with ellipticity $E = 0.098$ (Allen, 1973).

TABLE XVI. Saturn's rings visible areas for all S-band radar observations to date.

Date	Experimenters	$\|B\|$	ν_{max}	Ring	Geom. area (10^{15} m^2)	Proj. area (10^{15} m^2)
Jan 1973	Goldstein and Morris (1973)	26.4	290	B	14.50	6.448
				A	12.53	5.572
				B+A	27.03	12.020
Jan 1975	Goldstein *et al*. (1977)	24.4	294	B	14.24	5.885
				A	12.12	5.007
				B+A	26.36	10.892
Jan 1976	Pettengill *et al*. (1979)	21.4	301	B	13.95	5.090
				A	11.55	4.214
				B+A	25.50	9.304
April 1977	Ostro *et al*. (1979)	18.2	307	B	13.72	4.282
				A	11.24	3.509
				B+A	24.96	7.791
Feb 1978	Ostro *et al*. (1979)	11.7	317	B	13.40	2.718
				A	10.88	2.207
				B+A	24.28	4.925
Feb 1979		5.6	322	B	13.25	1.293
				A	10.72	1.046
				B+A	23.97	2.339

APPENDIX L. Saturn's rings shadowing calculation

Saturn may be considered an ellipsoid of revolution with ellipticity $E = 0.098$ (Allen, 1973, p. 140), i.e., a cross section containing its polar axis is an ellipse with semimajor axis $R_e = 59.779\times10^6$ m and semiminor axis αR_e where $\alpha = 1/(1+E) = 0.910747$ (see Fig. 32a):

$$r(\theta) = R_e \left(\cos^2\theta + \frac{\sin^2\theta}{\alpha^2}\right)^{-1/2} \qquad \text{(L1)}$$

The projection of Saturn in the direction of the radar will also be an ellipse with semimajor (equatorial) axis R_e but with apparent semiminor (polar) axis $R_p \geqslant \alpha R_e$. To find $R_p(B)$, one must find the point $[r(\theta'),\theta']$ at which the radar line of sight is tangent to this ellipse. Thomas (1969, p. 372) shows that $\tan\psi = r(\theta)/(dr/d\theta)$. Since

$$\frac{dr}{d\theta} = -\frac{1}{2}R_e\left(\cos^2\theta + \frac{\sin^2\theta}{\alpha^2}\right)^{-3/2}\left(-2\cos\theta\sin\theta + \frac{2\sin\theta\cos\theta}{\alpha^2}\right)$$

$$= R_e \sin\theta\cos\theta\,(1-\alpha^{-2})\left(\cos^2\theta + \frac{\sin^2\theta}{\alpha^2}\right)^{-3/2} \qquad \text{(L2)}$$

I find

$$\tan\psi = (\tan\theta + \alpha^2\cot\theta)/(\alpha^2-1) \qquad \text{(L3)}$$

where ψ is in the second quadrant. Since $\psi = 180° - B - \theta'$, I must solve

$$180° + \tan^{-1}\left(\frac{\tan\theta' + \alpha^2\cot\theta'}{\alpha^2-1}\right) = 180° - B - \theta' \qquad \text{(L4)}$$

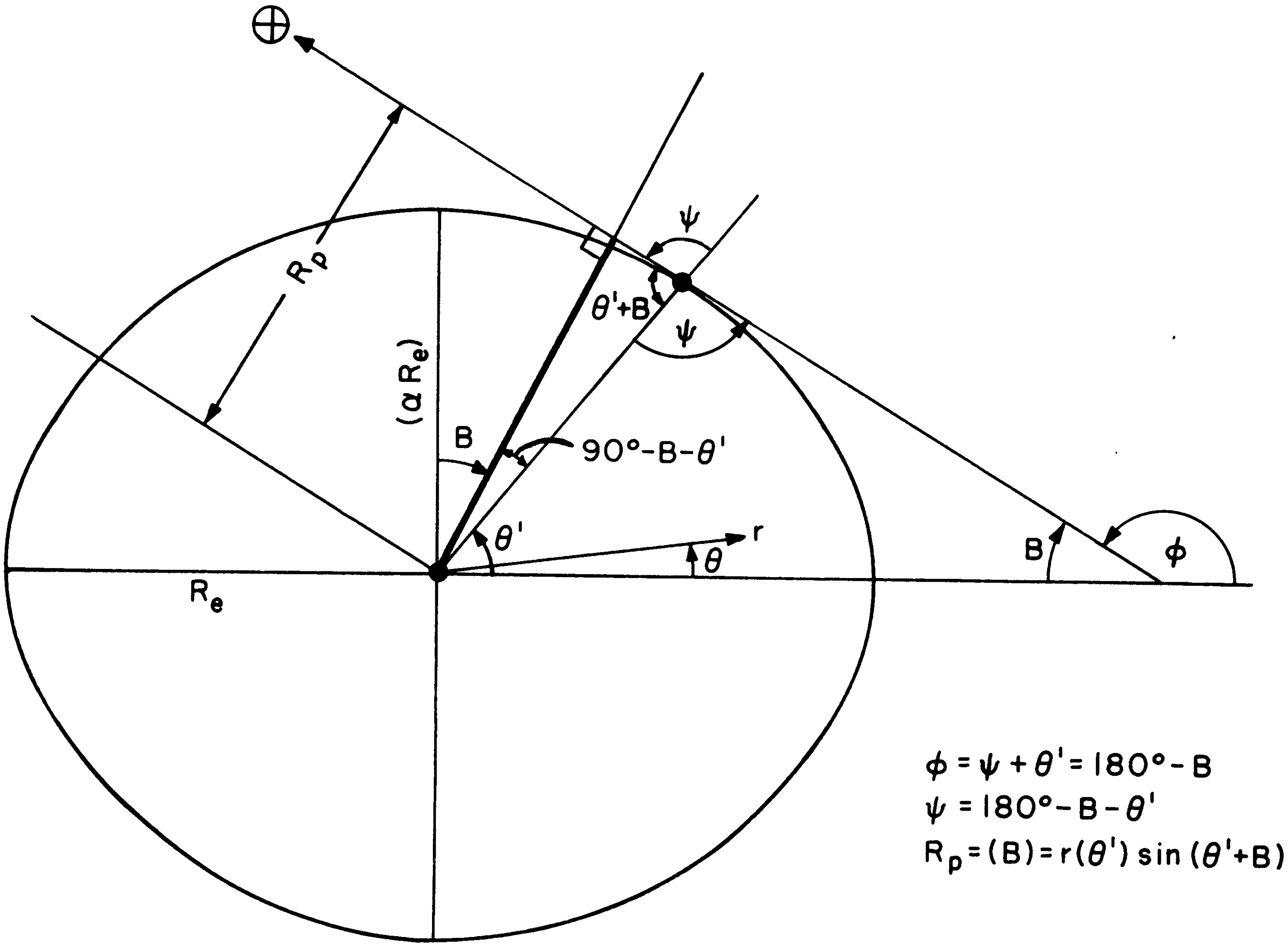

$$\phi = \psi + \theta' = 180° - B$$

$$\psi = 180° - B - \theta'$$

$$R_p = (B) = r(\theta') \sin(\theta' + B)$$

Fig. 32a. Geometry for Saturn's rings shadowing calculation.

where the inverse tangent is calculated as a negative value by my SR-56 calculator. The fastest way to find $\theta'(B)$ for a few values of B was to use my SR-56 to calculate the quantity

$$[\tan^{-1}(\frac{\tan\theta' + \alpha^2 \cot\theta'}{\alpha^2-1}) + B + \theta']$$

and adjust θ' to make this quantity equal to zero. Defining $\gamma = R_p/R_e$, I have the following table, in which I have included values of $\gamma^* = r(90°-B)/R_e$.

B	θ'	γ	γ^*
0.00	90.000	0.9107	0.9107
11.70	75.982	0.9146	0.9139
18.19	68.389	0.9198	0.9184
21.40	64.711	0.9231	0.9213
24.40	61.326	0.9266	0.9243
26.40	59.100	0.9291	0.9265

Given R_p, it is easy to project this "Saturn disc" ellipse onto the ring plane (Fig. 32b). The Saturn-disc ellipse is

$$r(\lambda) = (\frac{\cos^2\lambda}{R_e^2} + \frac{\sin^2\lambda}{R_p^2(B)})^{-1/2} \tag{L5}$$

The $\hat{y}$ coordinate of the point P is $y/\sin B = \frac{r(\lambda)\sin\lambda}{\sin B}$, so

$$R^2(\lambda) = r^2(\lambda)(\cos^2\lambda + \frac{\sin^2\lambda}{\sin^2 B}) \tag{L6}$$

and

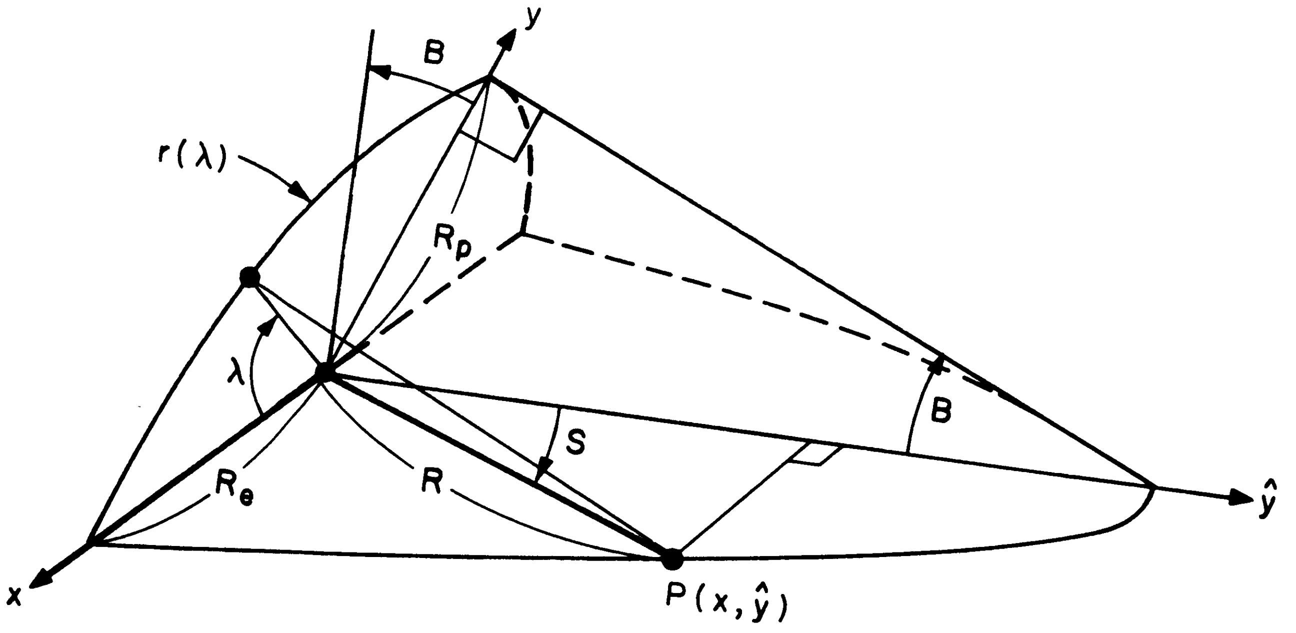

Fig. 32b. Geometry for Saturn's rings shadowing calculation.

$$S(\lambda) = \tan^{-1} (\frac{x}{\hat{y}}) = \tan^{-1} [r(\lambda) \cos (\lambda)/\hat{y}] = \tan^{-1}(\frac{\sin B}{\tan \lambda}) \qquad \text{(L7)}$$

The functional relationship between R(λ) and S(λ) follows:

$$R^2 = (\frac{\cos^2 \lambda}{R_e^2} + \frac{\sin^2 \lambda}{R_p^2})^{-1} (\cos^2 \lambda + \frac{\sin^2 \lambda}{\sin^2 B}) \qquad \text{(L8)}$$

$$R^2 = (1 + \frac{\tan^2 \lambda}{\sin^2 B})/(\frac{1}{R_e^2} + \frac{\tan^2 \lambda}{R_p^2}) \qquad \text{(L9)}$$

$$\tan^2 \lambda = [1 - (R/R_e)^2]/[(R/R_p)^2 - \frac{1}{\sin^2 B}] \qquad \text{(L10)}$$

so

$$\tan \lambda = [\frac{(R/R_e)^2-1}{1-(R/R_p)^2 \sin^2 B}]^{1/2} \sin B \qquad \text{(L11)}$$

and

$$S(R,B) = \tan^{-1} (\frac{\sin B}{\tan \lambda}) = \tan^{-1}\sqrt{\frac{1-(R/R_p)^2 \sin^2 B}{(R/R_e)^2-1}} \qquad \text{(L12)}$$

Thus if S is the minimum shadow-free orbital phase of particles in a ring with radius R,

$$S(R,B) = \begin{cases} 0 & , R \geqslant R_p/\sin B \\ \tan^{-1}\sqrt{\dfrac{1-(R/R_p)^2 \sin^2 B}{(R/R_e)^2-1}} & , \text{otherwise} \end{cases} \qquad \text{(L13)}$$

where $R_p = \gamma R_e$ from the table.

VI. REFERENCES

Aksnes, K., and F. A. Franklin (1976). Mutual phenomena of the Galilean satellites in 1973. III. Final results from 91 light curves. Astron. J. **81**, 464-481.

Allen, C. W. (1973). Astrophysical Quantities. Athlone Press, University of London, Great Britain.

Arfken, G. (1970). Mathematical Methods for Physicists. Academic Press, New York.

Beckmann, P. (1968). The Depolarization of Electromagnetic Waves. The Golem Press, Boulder, Colo.

Bevington, P. R. (1969). Data Reduction and Error Analysis for the Physical Sciences. McGraw - Hill, New York.

Blanco, C., and S. Catalano (1974a). Relation between light variations of solar system satellites and their interaction with interplanetary medium. In Exploration of the Planetary System, IAU Symposium No. 65 (A. Woszczyk and C. Iwaniszewski, Eds.), pp. 533-538. Dordrecht, Holland: D. Reidel.

Blanco, C., and S. Catalano (1974b). On the photometric variations of the Saturn and Jupiter satellites. Astron. Astrophys. **33**, 105-111.

Born, M., and E. Wolf (1975). Principles of Optics. Pergamon Press, New York.

Campbell, D. B. (1971). Radar interferometric observations of Venus. Ph.D. Thesis. Cornell University.

Campbell, D. B., J. F. Chandler, S. J. Ostro, G. H. Pettengill, and I. I. Shapiro (1978). Galilean satellites: 1976 radar results. *Icarus*, **34**, 254-267.

Campbell, D. B., J. F. Chandler, G. H. Pettengill, and I. I. Shapiro (1977). Galilean satellites of Jupiter: 12.6 cm radar observations, *Science* **196**, 650-653.

Campbell, M. J., and J. Ulrichs (1969). Electrical properties of rocks and their significance for lunar radar observations. *J. Geophys. Res.* **74**, 5867-5881.

Carpenter, R. L. (1966). Study of Venus by CW radar — 1964 results. *Astron. J.* **71**, 142-152.

Chandrasekhar, S. (1950). *Radiative Transfer*. Dover Publications, New York.

Clarke, D., and J. F. Grainger (1971). *Polarized Light and Optical Measurement*. Pergamon Press, New York.

Collett, E. (1968). The description of polarization in classical physics. *Am. J. Phys.* **36**, 713-725.

Conklin, N. (1976). Private communication.

Consolmagno, G. J., and J. S. Lewis (1978). The evolution of icy satellite interiors and surfaces. *Icarus* **34**, 280-293.

Cook, A. F., and F. A. Franklin (1958). Optical properties of Saturn's rings. I. Transmission. *Smithsonian Contrib. Astrophys.* **2**, 377-383.

Cook, A. F., and F. A. Franklin (1977). Saturn's rings: A new survey. In Burns, J. A., Ed., Planetary Satellites, University of Arizona Press, Tucson, Arizona.

Cook, A. F., F. A. Franklin, and F. D. Palluconi (1973). Saturn's rings: A survey. Icarus **18**, 317-337.

Cuzzi, J. N., and J. B. Pollock (1978). Saturn's rings: Particle composition and size distribution as constrained by microwave observations. I. Radar observations. Icarus **33**, 233-262.

Diedrich, J. H., I. J. Loeffler, and F. S. Stepka (1964). Brittle behavior of beryllium, graphite, and lucite under hypervelocity impact. In Proceedings of the Seventh Hypervelocity Impact Symposium, Vol. 6, pp. 27-47. Avail. as AD463230 from the Defense Documentation Center, Alexandria, Va.

Evans, J. V., and T. Hagfors (1966). Study of radio echoes from the moon at 23 centimeter wavelength. J. Geophys. Res. **71**, 4871-4899.

Evans, J. V., and T. Hagfors, Eds. (1968). Radar Astronomy. McGraw-Hill, New York.

Ferrin, I. R. (1974). Saturn's rings. I. Optical thickness of rings A, B, D and structure of ring B. Icarus **22**, 159-174.

Ferrin, I. R. (1975). Saturn's rings. II. Condensations of light and optical thickness of Cassini's Division. Icarus **26**, 45-53.

Fink, V., N. Dekkers, and H. P. Larson (1973). Infrared spectra of the Galilean satellites of Jupiter. *Astrophys. J.* **179**, L155-L159.

Franklin, F. A., and G. Colombo (1978). On the azimuthal brightness variations of Saturn's rings. *Icarus* **33**, 279-287.

Fung, A.K. (1967). Character of wave depolarization by a perfectly conducting rough surface and its application to earth and moon experiments. *Planet. Space Sci.* **15**, 1337-1347.

Goldstein, R. M. (1970). Radio and radar studies of Venus and Mercury. *Radio Sci.* **5**, 391-395.

Goldstein, R. M. (1971). Radar observations of Mercury. *Astron. J.* **76**, 1152-1154.

Goldstein, R. M. (1977). Private communication.

Goldstein, R. M. (1978). Private communication.

Goldstein, R. M., R. R. Green, G. H. Pettengill, and D. B. Campbell (1977). The rings of Saturn: Two-frequency radar observations. *Icarus* **30**, 104-110.

Goldstein, R. M., and G. A. Morris (1973). Radar observations of the rings of Saturn. *Icarus* **20**, 260-262.

Goldstein, R. M., and G. A. Morris (1975). Ganymede: Observations by radar. *Science* **188**, 1211-1212.

Goldstein, R. M., and G. H. Pettengill (20 April 1973). Proposal to observe the Rings of Saturn by radar at Arecibo Observatory.

Green, P. E., Jr. (1968). Radar measurements of target scattering properties. In *Radar Astronomy* (J. V. Evans and T. Hagfors, Eds.), p. 1-77. McGraw-Hill, New York.

Gromova, L. V., V. I. Moroz, and D. P. Cruikshank (1970). The spectrum of Ganymede in the region 1-1.7 microns. *Astron. Circular* (USSR), No. 569, p. 6.

Guerin, P. (1969). Sur la mise en evidence d'un quatrieme anneau et d'une nouvelle division obscure dans le systeme des anneaux de Saturne. *Compt. Rend.* **270**, 125-128.

Guerin, P. (1970). The new ring of Saturn. *Sky and Telescope* **40**, 88.

Hagen, J. B., and D. T. Farley (1973). Digital-correlation techniques in radio science. *Radio Sci.* **8**, 775-784.

Hagfors, T., and D. B. Campbell (1974). Radar backscattering from Venus at oblique incidence at a wavelength of 70 cm. *Astron. J.* **79**, 493-502.

Hagfors, T., and J. H. Evans (1968). Radar studies of the Moon. *In Radar Astronomy* (J. V. Evans and T. Hagfors, Eds). pp. 219-273. McGraw-Hill, New York.

Hapke, B. (1963). A theoretical photometric function for the lunar surface. *J. Geophys. Res.* **68**, 4545-4570.

Harris, D. L. (1961). Photometry and calorimetry of the planets and satellites. In *Planets and Satellites* (G. P. Kuiper and B. M. Middlehurst, Eds.), p. 272. University of Chicago Press, Chicago.

Hill, N. E., W. E. Vaughan, A. H. Price, and M. Davies (1969). *Dielectric Properties and Molecular Behavior*, p. 401. Van Nostrand Reinhold, New York.

Hobbs, P. V. (1974). *Ice Physics*. Clarendon Press, Oxford.

Jackson, J. D. (1962). *Classical Electrodynamics*. John Wiley and Sons, New York.

Johnson, T. V. (1969). *Albedo and Spectral Reflectivity of the Galilean Satellites of Jupiter*. Ph.D. dissertation. California Institute of Technology, Pasadena, California.

Johnson, T. V. (1971). Galilean satellites: Narrowband photometry 0.30 to 1.10 microns. *Icarus* **14**, 94-111.

Johnson, T. V., and T. B. McCord (1971). Spectral geometric albedo of the Galilean satellites, 0.3 to 2.5 microns. *Astrophys*. *J*. **169**, 589-594.

Johnson, T. V. and T. R. McGetchin (1973). Topography on satellite surfaces and the shape of asteroids. *Icarus* **18**, 612-620.

Jordan, E. C., and K. G. Balmain (1968). *Electromagnetic Waves and Radiating Systems*. Prentice-Hall, Englewood Cliffs, New Jersey.

Jurgens, R. F., and D. F. Bender (1977). Radar detectability of asteroids. *Icarus* **31**, 483-497.

Kaula, W. M. (1968). *An Introduction to Planetary Physics*: *The Terrestrial Planets*. John Wiley, New York.

Kuiper, G. P. (1957). Infrared observations of planets and satellites. *Astron*. *J*. **62**, 245.

Kraus, J. D. (1966). *Radio Astronomy*. McGraw-Hill, New York.

Lee, T. (1972). Spectral albedos of the Galilean satellites. *Comm. Lunar Planet. Lab.* **9**, 179-180.

Lewis, J. S. (1971). Satellites of the outer planets: Thermal models. *Science* **172**, 1127-1128.

Lewis, J. S. (1973). Chemistry of the outer solar system. *Space Sci-Rev*. **14**, 401.

Liou, K., and R. M. Schotland (1971). Multiple backscattering from water clouds for a pulsed lidar system. *J. Atmos. Sci.* **22**, 772. As quoted by Cuzzi and Pollack (1978).

Long, M. W. (1965). On the polarization and the wavelength dependence of sea echo. *Trans. IEEE* **AP-14**, 749-754.

Lumme, K., and W. M. Irvine (1976). Azimuthal brightness variations of Saturn's rings. *Astrophys. J.* **204**, L55-L57.

McNeill, W. R., and A. I. Carswell (1975). Lidar polarization studies of the troposphere. *Appl. Opt.* **14**, 2158.

Moroz, V. I. (1965). Infrared spectrophotometry of satellites: The Moon and the Galilean satellites of Jupiter. Trans in *Soviet Astron.*-**AJ9** , 999-1006.

Morrison, D., and D. P. Cruikshank (1974). Physical properties of the natural satellites. *Space Sci. Rev.* **15**, 641-739.

Morrison, D., N. D. Morrison, and A. R. Lazarewicz (1974). Four-color photometry of the Galilean satellites. *Icarus* **23**,399-416.

Muhleman, D. O. (1964). Radar scattering from Venus and the Moon. Astron. J. 69, 34-41.

Newburn, R. L., and S. Gulkis (1973). A survey of the outer planets: Jupiter, Saturn, Uranus, Neptune, Pluto and their satellites. Space Sci. Rev. 14, 179-271.

Ostro, S. J. (1976). The low-Doppler excess in the radar echo from Saturn's rings. M.I.T. General Examination Paper. Unpublished.

Ostro, S. J., and G. H. Pettengill (1979). Saturn's rings: 1977 and 1978 radar results. In preparation.

Ostro, S. J., and G. H. Pettengill (1978). Icy craters on the Galilean satellites? Icarus, 34, 268-279.

Ostro, S.J., G. H. Pettengill, I. I. Shapiro, and D. B. Campbell (1979). Galilean Satellites: 1977 radar results. In preparation.

Papas, C. H. (1965). Theory of Electromagnetic Wave Propagation. McGraw-Hill, New York.

Peale, S. J. (1977). Rotational histories of the natural satellites. Chapter 6 in Planetary Satellites (J. A. Burns, Ed.). University of Arizona Press, Tucson.

Perutz, M. F. (1948). A description of the iceberg aircraft carrier and the bearing of the mechanical properties of frozen wood pulp upon some problems of glacier flow. J. Glaciol. 1, 95-102.

Pettengill, G. H. (1968). Radar studies of the planets. In Radar Astronomy (J. V. Evans and T. Hagfors, Eds.), pp. 275-321. Mc Graw-Hill, New York.

Pettengill, G. H. (1970). Radar Astronomy. Chapter 33 in *Radar Handbook* (M. I. Skolnik, Ed.). McGraw-Hill, New York.

Pettengill, G. H. (1976, 1977, 1978). Private communication.

Pettengill, G. H., D. B. Campbell, R. R. Green, S. J. Ostro, and I. I. Shapiro (1978). Radar observations of 1 Ceres. *Icarus*, in preparation.

Pettengill, G. H., and T. Hagfors (1974). Comment on radar scattering from Saturn's rings. *Icarus* **21**, 188-190.

Pettengill, G. H., and J. C. Henry (1962). Radio measurements of the lunar surface. In *The Moon, IAU Symposium 14* (Z. Kopal and A. A. Mikhailov, Eds.), p. 519. Academic Press, London.

Pettengill, G. H., S. J. Ostro, D. B. Campbell, and R. M. Goldstein (1977). Saturn's rings: radial distribution of radar scatterers. Paper presented at 8th Annual Meeting of Amer. Astron. Soc. Division of Planetary Sciences, 21 Jan 77.

Pettengill, G. H., S. J. Ostro, D. B. Campbell, and R. M. Goldstein (1979). Saturn's rings: Delay-Doppler radar study. In preparation.

Pilcher, C. B., S. T. Ridgway, and T. B. McCord (1972). Galilean satellites: Identification of water frost. *Science* **178**, 1087-1089.

Pollack, J. B. (1975). The rings of Saturn. *Space Sci. Rev.* **18**, 3.

Pollack, J. B., and L. Whitehill (1972). A multiple-scattering model of the diffuse component of lunar radar echoes. *J. Geophys. Res.* **77**, 4289-4303.

Reitsema, H. J., R. F. Beebe, and B. A. Smith (1976). Azimuthal brightness variations in Saturn's rings. *Astron. J.* **81**, 209-215.

Sassen, K. (1974). Depolarization of laser light backscattered by artificial clouds. *J. Atmos. Sci.* **13**, 923.

Schotland, R. M., K. Sassen, and R. Stone (1971). Observations by lidar of linear depolarization ratios by hydrometers. *J. Appl. Meterol.* **10**, 1011. As quoted by Cuzzi and Pollack (1978).

Simpson, R. A. (1973). Lunar radar echoes: An interpretation emphasizing characteristics of the leading edge. Stanford Electronics Laboratories, Radioscience Laboratory Report No. 42, Stanford Univ., Stanford, CA.

Smith, B. A., A. F. Cook, W. A. Feibelman, and R. F. Beebe, (1975). On a suspected ring external to the visible rings of Saturn. *Icarus* **25**, 466-469.

Smith, E. I, and A. G. Sanchez (1973). Fresh lunar craters: Morphology as a function of diameter, a possible criterion for crater origin. *Modern Geology* **4**, 51-59.

Thomas, G. B. (1969). *Calculus and Analytic Geometry*. Addison-Wesley, Reading, Massachusetts.

Thompson, T. W. (1965). A study of radar scattering behavior of lunar craters at 70 cm. Research Report RS 64, Center for Radiophysics and Space Research, Cornell University, Ithaca, New York.

Vermilion, J. R., R. N. Clark, T. F. Greene, J. F. Seamans, and W. F. Yantis (1974). A low resolution map of Europa from four occultations by Io. *Icarus* **23**, 89-96.

Veverka, J. (1971). Polarization measurements of the Galilean satellites of Jupiter. *Icarus* **14**, 355-359.

Veverka, J. (1977). Photometry of satellite surfaces. In *Planetary Satellites* (J. A. Burns, Ed.), p. 171. University of Arizona Press, Tucson, Arizona.

Weast, R. C., and S. M. Selby (1975), Eds. *CRC Handbook of Tables for Mathematics*. CRC Press, Cleveland.

Zerull, R. (1976). Scattering functions of dielectric and absorbing irregular particles. In *Interplanetary Dust and Zodiacal Light* (H. Elsässer and H. Fechtig, Eds.) Proc. IAU Coll. 31, Heidelberg. As quoted by Cuzzi and Pollack (1978).

Zerull, R. (1974). Light scattering by dielectric and absorbing irregular particles. *Beit*. *Phys*. *Atmos*., to appear. As quoted by Cuzzi and Pollack (1978).

BIOGRAPHICAL NOTE

Steven J. Ostro was born on March 9, 1946, in Somerville, New Jersey. He attended public schools in Somerville until 1964, when he began the five-year engineering program at Rutgers, The State University, in New Brunswick, New Jersey.

While at Rutgers, Mr. Ostro received the Abraham Messler Quick Award for Outstanding Sophomore, and was elected to Phi Beta Kappa and Tau Beta Pi. The technical emphasis of his final two undergraduate years was in ceramics, his research focusing on the surface properties of high-temperature porcelain glazes. His extracurricular activities included intercollegiate rowing, sport parachuting, and amateur astronomy. He was awarded a B.S. Degree in Ceramic Science and a A.B. Degree in Liberal Arts in June 1969.

From 1970 to 1971, the author was employed as a research ceramist by Corning Glass Works in Corning, New York. Here he investigated reboil phenomena in photochromic and high-lead commercial glasses.

Mr. Ostro married Jeanne Musca, of Berkeley Heights, New Jersey, in May 1971.

In 1972, he left Corning to enter Cornell University's Department of Applied and Engineering Physics as a graduate student. While at Cornell, he did research on the optical scattering properties of particulate surfaces. He was awarded a Master of Engineering Degree in Engineering Physics in June 1974.

Since that time, Mr. Ostro has been a graduate student in MIT's Department of Earth and Planetary Sciences. He and his wife live in Boston with their cats, who frequently accompany them to the Arecibo Observatory in Puerto Rico. Mr. Ostro's major outside interest is karate. His wife is the Protocol Program Coordinator for the MIT Medical Department, bakes fabulous bread, and studies classical ballet.